DEVELOPING SURFACE ENHANCED RAMAN SPECTROSCOPY AND POLYMER HOLLOW PARTICLES FOR SENSING AND MEDICAL IMAGING APPLICATIONS

A Dissertation
Presented to
The Academic Faculty
By

Christine H. Moran

In Partial Fulfillment
Of the Requirements for the Degree
Doctor of Philosophy in Biomedical Engineering

Georgia Institute of Technology

December, 2013

DEVELOPING SURFACE ENHANCED RAMAN SPECTROSCOPY AND POLYMER HOLLOW PARTICLES FOR SENSING AND MEDICAL IMAGING APPLICATIONS

Approved by:

Dr. Younan Xia, Advisor
Department of Biomedical Engineering,
School of Chemistry and Biochemistry
Georgia Institute of Technology and Emory University

Dr. Zhiqun Lin
School of Materials Science and Engineering
Georgia Institute of Technology

Dr. Shuming Nie
Department of Biomedical Engineering
Emory University and Georgia Institute of Technology

Dr. Mark Prausnitz
School of Chemical and Biomolecular Engineering
Georgia Institute of Technology

Dr. Johnna Temenoff
Department of Biomedical Engineering
Georgia Institute of Technology and Emory University

Date Approved: October 1, 2013

Dedicated to my loving and supportive family.

ACKNOWLEDGEMENTS

Thank you Prof. Xia for your support and guidance during my tenure in your lab. I have learned so much over the past four and a half years. I would also like to thank the members of the Xia group, especially those current and former members who have played a significant role in my experience and training: Dr. Matthew Rycenga, Dr. Meng-Yi Bai, Dr. Xiaohu Xia, Dr. Yu Shrike Zhang, Wenying Liu, Dr. Claire Cobley, and Dr. Dong Hyun. I am grateful to the staff at Georgia Tech who helped smooth our transition and guide me through the path to graduation, Shannon Sullivan and Denna Cummings, and to the department chair at the time, Dr. Larry McIntire. Thank you to Dr. Frank Yin and Karen Teasdale at Washington University in St. Louis for helping me to get launched into my graduate career, and to Lori Williams and Glen Reitz for all your administrative help.

I am especially grateful for the love and support of my family, especially my parents Caroline and Steve Moran, who didn’t question my decision to go to graduate school (too much) and encouraged me through difficult times. Thank you to my grandfather, Raymond Bratschi, for saving articles about nanotechnology for me, and to my fiancé Christopher Kielhorn for being a source of encouragement and peace.

TABLE OF CONTENTS

LIST OF TABLES

LIST OF FIGURES

LIST OF ABBREVIATIONS

1,4-BDT	1,4-Benzenedithiol
^{19}F	Fluorine-19 Isotope
2-NT	2-Naphthalenethiol
3D	Three-Dimensional
4-MBT	4-Methylbenzenethiol
AFM	Atomic Force Microscopy
$AgNO_3$	Silver Nitrate
AM	Alternating Minimization
B_v	Blur Value
CCD	Charge-Coupled Device
CD4	Cluster of Differentiation 4 Glycoprotein
CT	Computed Tomography
D-band	Disorder Band
DCLS	Direct Classical Least-Squares
DI	Deionized
DNA	Deoxyribonucleic Acid
d_s	Distance to substrate
E-beam	Electron Beam
EBID	Electron Beam Induced Deposition
EF	Enhancement Factor
E-field	Electric Field
FRET	Fluorescence Resonance Energy Transfer
FWHM	Full-Width Half-Maximum
G-Band	Graphite Band
GI	Gastrointestinal
Her2	Human Epidermal Growth Factor Receptor 2
ICC	Iodinated Contrast Compound
IgG	Immunoglobulin G
λ	Weighting Factor
LDPE	Low-Density Polyethylene
LOD	Limit of Detection
LSP	Localized Surface Plasmon
LSPR	Localized Surface Plasmon Resonance
mPEG-SH	Methoxy-terminated Poly(ethylene glycol) Thiol
MR	Magnetic Resonance
N	Multiplexing Number
NIR	Near-Infrared

P_a	Peak-to-Peak Area
PCA	Principle Component Analysis
PCL	Polycaprolactone
PDMAm	Poly(*N*,*N*-dimethyl acrylamide)
PDMS	Poly(dimethyl siloxane)
PEG	Poly(ethylene glycol)
PET	Positron Emission Tomography
PFCE	Perfluoro-15-crown-5-ether
PFO	Perfluorooctane
PLGA	Poly(lactic-co-glycolic) Acid
PMMA	Poly(methyl methacrylate)
PR	Polynomial Regression
PSF	Point Spread Function
PVA	Poly(vinyl alcohol)
PVP	Polyvinylpyrrolidone
RES	Reticuloendothelial System
RF	Radiofrequency
SAM	Self-Assembled Monolayer
SEM	Scanning Electron Microscopy
SERRS	Surface-Enhanced Resonance Raman Spectroscopy
SERS	Surface-Enhanced Raman Spectroscopy
SiRNA	Small Interfering Ribonucleic Acid
SM	Single-Molecule
SNSP	Silver Nanoparticle SERS Probe
SWNT	Single-Walled Carbon Nanotube
TAT	Thermoacoustic Tomography
TEM	Transmission Electron Microscopy
T_g	Glass-Transition Temperature
TMFP	Transport Mean Free Path
UV	Ultraviolet
UV-Vis	Ultraviolet-Visible

SUMMARY

Early diagnosis of disease and developing targeted therapeutics are two major goals of medical research to which nanotechnology can contribute a variety of novel approaches and solutions. This work utilized an optical phenomenon specific to metallic nanoparticles, surface-enhanced Raman spectroscopy (SERS), as a nanomedicine research tool to aid in the progression toward these goals. Single-particle SERS studies were streamlined to identify particles or aggregates with potentially high enhancement factors (EFs) for applications requiring ultrasensitive and possibly single-molecule detection. SERS was used to probe the changes in surface chemistry of nanoparticles for optimizing nanomedicine applications. Fundamental SERS imaging parameters were identified, and a new algorithm for multiplexed SERS imaging was developed and tested.

Novel particle-based contrast agents were also developed. Polystyrene hollow beads with a single hole on the surface were fabricated and used to encapsulate contrast agents for a variety of medical imaging modalities. Saline was encapsulated as a novel contrast agent for thermoacoustic tomography (TAT). Encapsulation of X-ray computed tomography (CT) and magnetic resonance (MR) imaging was also performed and tested.

CHAPTER 1: INTRODUCTION

1.1 Nanotechnology and Medicine

Two major goals of medical research are early diagnosis and more effective, targeted treatments. It is precisely these two aspects of medicine that nanotechnology research has pursued in the biomedical realm. Disease should be detected and therapy should be administered directly at the molecular level rather than waiting for macroscopic symptoms to surface. Imaging and detection techniques conceived around nanomaterials should improve the capability of doctors and scientists to target and identify a specific cell, protein, DNA sequence, or even small molecule, in order to improve patient outcomes.[1-3]

Because of their small size and customizable surface chemistry, nanoparticles provide advantages in sensitive detection and targeted applications. Advanced synthesis techniques have been developed to achieve unprecedented control over the materials, shapes, and sizes of nanoparticles.[4] These advances have led to the development of a variety of microscopic biological sensors by utilizing the interesting physical phenomena that arise on the nanoscale. In some cases, these phenomena give nanoparticles easily distinguishable signatures for use in imaging or detection. For example, the quantum confinement effect occurring in nanoscale semiconductors, or quantum dots, results in tunable fluorescence peaks with broad excitation and good stability (major improvements over traditional molecular fluorophores). The good stability, high quantum yield, and optical tunability of quantum dots are some of the attractive properties for labeling and detection of cells, proteins, and nucleic acids.[2] Other nanoscale phenomena are very sensitive to small changes in the local environment. One-dimensional nanoparticles such as semiconductor nanowires or carbon nanotubes that have been applied as electrical detection systems by

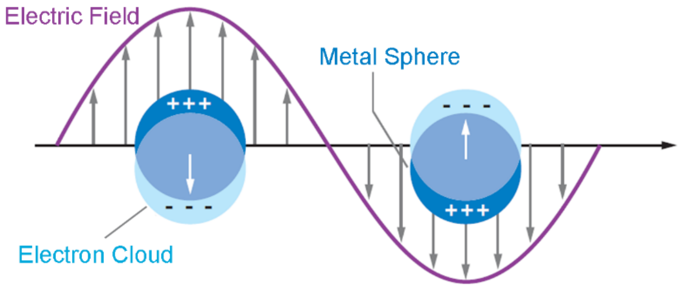

Figure 1.1. Schematic illustration of the LSPR phenomenon.[6] Republished with permission of Annual Reviews, from Localized Surface Plasmon Resonance Spectroscopy and Sensing by K. A. Willets and R. P. van Duyne, vol. 58, 2007; permission conveyed through Copyright Clearance Center, Inc.

measuring conductivity changes upon binding of a target molecule like a protein.[1,2]

Metallic nanoparticles also have a diverse spectrum of applications in the biomedical realm. One of the unique optical properties of metallic nanoparticles, especially those composed of Au or Ag, is the surface plasmon resonance (SPR). The SPR is the excitation of coherent oscillation of the surface conduction electrons at a particular frequency, and in bulk metals the SPR can propagate in the *x* and *y* directions along the metal's surface.[5-7] When the size of the metal particle is much smaller than the wavelength of the incident light, as with nanoparticles, the oscillation is confined to the nanoparticle and cannot propagate, so it is called the localized surface plasmon resonance (LSPR) (Figure 1.1).[6,7] The LSPR is reflected by distinct peaks in the extinction spectrum of a suspension of nanoparticles. Extinction spectra reveal how a suspension of nanoparticles is absorbing and scattering photons of different wavelengths, so peaks in the spectra indicate wavelengths of light that interact strongly with the nanoparticles, and can be seen clearly in Figure 1.2.[7] The LSPR also provides metallic nanoparticles with fascinating multimodal properties. The LSPR is another example of a nanoscale phenomenon that is very sensitive to changes in the environment, and the binding of proteins to the surface of metal

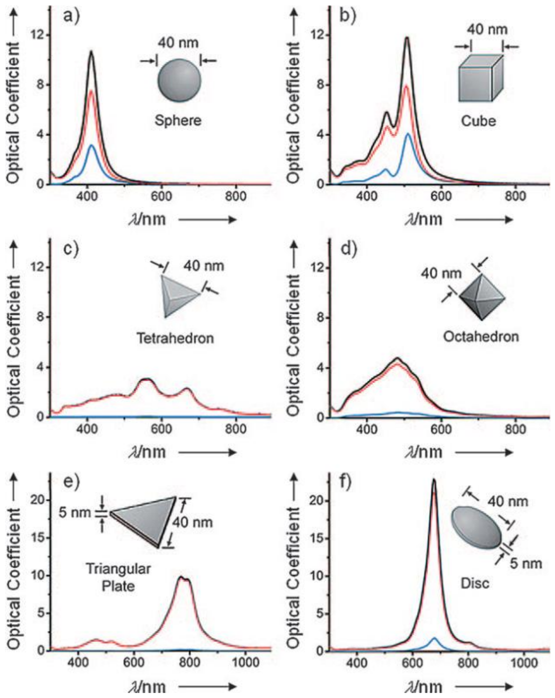

Figure 1.2. Silver nanoparticles with different shapes have different LSPR properties, as indicated by their calculated UV-vis extinction (black), absorption (red), and scattering (blue) spectra.[7] Adapted with permission from J. Phys. Chem. B Copyright 2006 American Chemical Society.

nanoparticles, for example, would result in a measurable shift in the LSPR peak.[6,7] Metal nanoparticles have also been used as transducers for photothermal therapy, as contrast agents for various imaging modalities, as sensitive detectors, and even as triggers for controlled release of drugs.[5,8-11]

The surfaces of nanoparticles can be easily modified to target them to specific tissues in the body, like a tumor. Nanoparticles carrying drugs and imaging contrast agents, or which are acting as therapeutic agents directly, can be delivered to the tissue of interest in greater amounts than nanoparticles with unmodified surface chemistry.[9,12,13] This has implications in not only more efficient cancer therapy, but also in early detection of disease. However, leftover surfactants and capping agents from synthesis may potentially interfere with the surface chemistry modification, and since some capping agents are toxic, it is important to confirm these compounds have been completely removed.[14,15] A better understanding of the kinetics of surface-modification by monitoring the removal of capping agents and their simultaneous replacement by functional molecules would give researchers greater confidence when developing targeted nanoparticles for *in vivo* applications.

1.2 Ultrasensitive Detection with Surface-Enhanced Raman Spectroscopy

Nanoparticles composed of Au and Ag can have LSPR peaks in the visible and near-infrared (NIR) regions, giving suspensions of these nanoparticles distinctive colors.[7,16] The position of the LSPR peak depends on the composition, size, shape, structure, and external environment of the nanoparticle, and can thereby be tuned by controlling these parameters.[4,5,7] Figure 1.2 illustrates the effect of nanoparticle shape on the LSPR. As mentioned earlier, the LSPR peak itself can be used for detection since its position is highly sensitive to the environment of the nanoparticle.[6,7] However, another application of the plasmonic effect, surface-enhanced Raman spectroscopy (SERS), tends to be richer in information.

Raman spectroscopy, a type of vibrational spectroscopy, uses inelastic scattering to detect different vibrational modes present in a sample (Figure 1.3).[17] The vibrational modes present in a molecule are dependent on its unique chemical structure, so the resulting Raman spectrum serves as a molecular fingerprint.[7,17,18] This capability is the major advantage of Raman spectroscopy. However, Raman scattering is intrinsically weak, several orders of magnitude weaker than fluorescence signals, and so this technique was not seriously considered for medical applications.[17]

With the demonstration of SERS forty years ago, first by Fleischmann *et al.*,[19] and

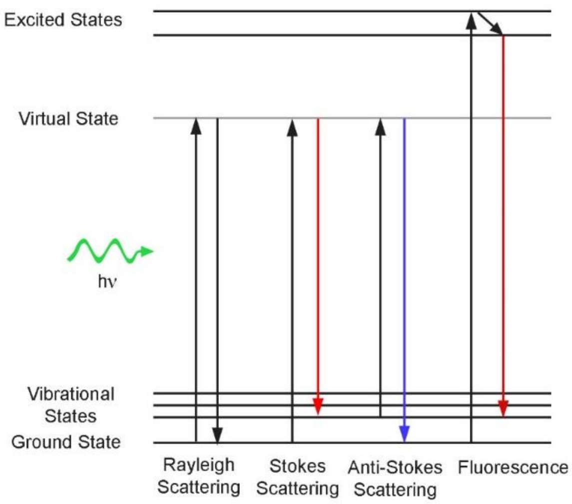

Figure 1.3. Diagram of electronic states for a typical molecule and different radiative transitions. Stokes and anti-Stokes are two types of Raman scattering, the difference being in whether the scattered light has energy greater or less than the incident photon. Rayleigh scattering and fluorescence are also displayed for comparison.

explained later by Jeanmaire and Van Duyne[20] and Albrecht and Creighton,[21] the door was opened for Raman spectroscopy to be used with medical applications.[7,17] These landmark studies found that when molecules of interest were placed on a roughened noble-metal substrate, the Raman signal intensities were greatly amplified.[19-21] The cause of the enhancement is still a subject of debate, but is generally regarded to be a combination of electromagnetic enhancement and chemical enhancement.[22,23] The electromagnetic enhancement is a result of the LSPR which gives rise to an enhanced local electric field (E-field) at the metal surface that decays evanescently away from the surface.[6,17,22] The chemical enhancement theory attributes enhancement to the effects of molecule chemisorption on the metal surface.[23]

The level of enhancement, or enhancement factor (EF), varies with many factors, including the shape and size of the nanoparticle, the type of Raman reporter molecule, and the properties of the incident light.[23,24] The EF is calculated by comparing the enhanced signal to the ordinary Raman signal of a molecule according to the following equation:

$$EF = (I_{SERS} \times N_{ordinary}) / (I_{ordinary} \times N_{SERS}) \qquad (1)$$

where I_{SERS} and $I_{ordinary}$ are a particular band's intensity for the SERS and ordinary Raman spectra, respectively, and N_{SERS} and $N_{ordinary}$ are the number of molecules probed in the collection of each spectrum.[24,25] Maximum EFs are estimated to be about 10^{12}, but EFs on the order of 10^{8} are more typical.[24] These incredible enhancements from relatively few molecules on the surface of a nanoparticle makes SERS an appealing choice for targeted and sensitive detection.

The maximum EFs are typically localized to areas on the SERS substrate with extremely high local E-fields, known as hot spots. Hot spots can result from asymmetry in the nanoparticle, such as the sharp corners of a nanocube, that cause the E-field resulting from the LSPR to concentrate in those areas.[26] The intensity of SERS signals is directly related to the magnitude of the E-field, causing greater SERS enhancement for molecules located there.[24] Additionally, the gaps between particles that are very close together also act as hot spots.[27,28] When engineering sensing platforms using SERS, hot spots are often included to maximize the potential EF of the system, and therefore its sensitivity.[29-31] Designing an effective SERS substrate means understanding the connection between the physical parameters of the substrate and its SERS EF. The study of the relationship between physical structure and SERS EFs is an active area of research in the SERS field. However, experiments are often tedious, leaving much room for improvement.

There are several ways in which SERS has found use in medical applications. The specific molecular information given by SERS spectra makes it an excellent label-free

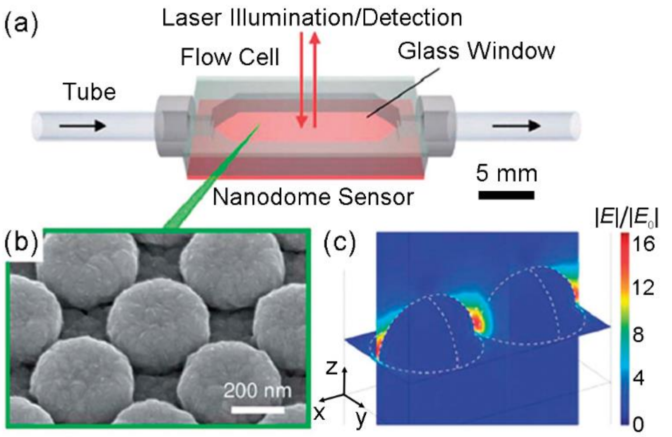

Figure 1.4. Unlabeled SERS detection chip incorporated in medical tubing for monitoring the composition of blood or other fluids in real time. (a) Schematic of the flow cell, in which a (b) nanodome sensor structure is incorporated into the bottom surface. (c) 3D model of E-field distribution in nanodome sensor structure. Red areas are hot-spots between domes, indicating the effectiveness of this substrate for SERS.[29] Reproduced by permission of the Royal Society of Chemistry.

detection technique (Figure 1.4). Assays which once depended on dyes or other means of secondary spectroscopic detection can be simplified to identification of the molecular species itself, especially if the analyte can be localized to a hot spot. This approach has been used for applications such as quantitative detection of certain disease-causing microorganisms, monitoring drug analytes in the bloodstream, and even measuring drug release in a single cell.[5,18,29]

Additionally, SERS is used in label-based detection and diagnostic tools. In situations where the target molecule does not have a strong or easily distinguishable spectrum, Raman-active probes are attached to nanoparticles and targeted to a specific ligand, which usually results in the formation of a hot spot via nanoparticle aggregation (Figure 1.5). This principle has been used to develop SERS-based immunoassays, detection assays for specific DNA sequences and mutations, and identification of individual cells.[1,18,30-32]

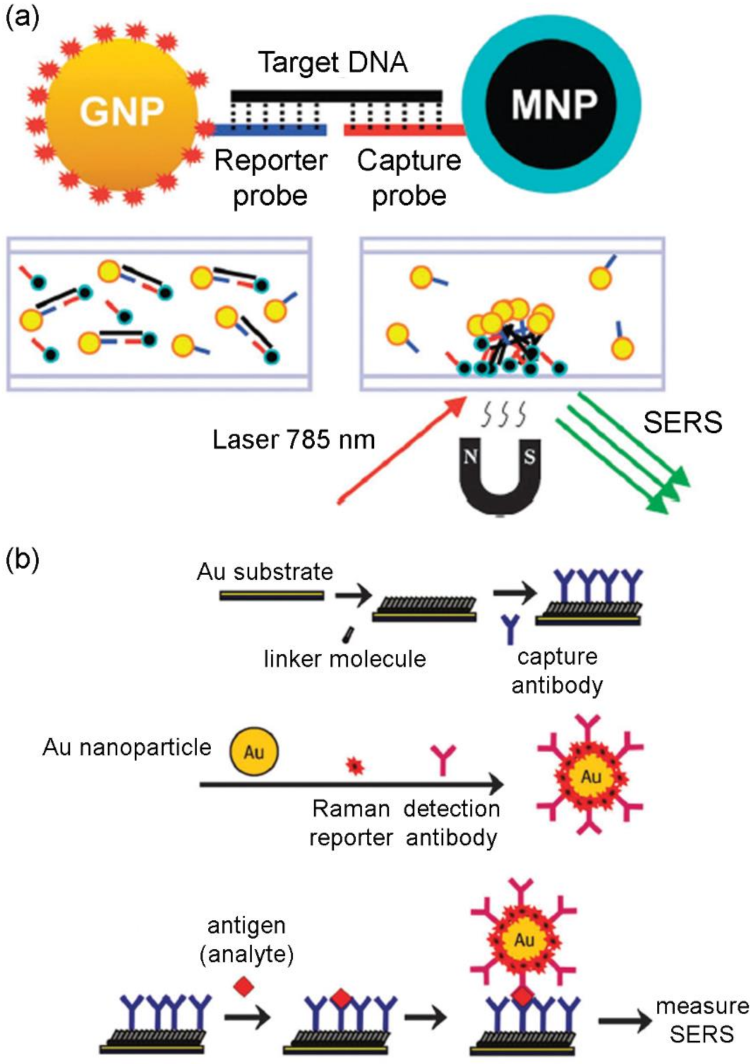

Figure 1.5. Schematics of two examples of labeled SERS assays. (a) DNA target detection using magnetic nanoparticles to encourage aggregation in the presence of the target DNA, providing additional enhancement by creating hotspots between Au nanoparticles.[30] Adapted with permission from Anal. Chem. Copyright 2011 American Chemical Society. (b) SERS sandwich immunoassay utilizing Au substrate and Au nanoparticles to achieve high EFs in the presence of the antigen.[31] Adapted with permission from Anal. Chem. Copyright 2011 American Chemical Society.

Finally, SERS can be used for imaging. Like fluorescence imaging, the detection of signals from a molecule as a result of illumination with an incident light source is mapped in space to create an image of the location of the molecules. SERS imaging is possible with both labeled and unlabeled approaches to SERS, rendering it flexible and useful.[18]

SERS clearly has great potential to improve approaches for ultrasensitive detection and medical imaging. The research presented in this dissertation investigated SERS not only in this capacity, but also as a valuable new research tool in the development and production of particle-based therapeutics and imaging contrast agents.

1.3 Medical Imaging

Medical imaging has become an indispensable tool in the fields of medicine and medical research thanks to many technological advances over the past 25 years.[33] Not only have new modalities been invented, such as magnetic resonance (MR) imaging or SERS imaging, but also existing technologies have evolved, making them even more powerful, as in X-ray computed tomography (CT). These developments have enabled rapid diagnosis of disease through visualization and quantitative assessment.

Many of these advanced imaging applications require the use of a good contrast agent, which also provides additional functionality to many established imaging modalities. X-ray, for example, was already used extensively to evaluate the skeletal system, which provides intrinsic contrast. However, with the development and use of contrast agents such as iodinated compounds, X-ray has also expanded into imaging of soft tissue with high resolution.[34] The improvement of digital technology has led to more sophisticated imaging modalities, as well as greatly improved the existing imaging hardware. With higher resolution and the capability to collect large and complex data-sets, medical imaging can demand more targeted imaging applications. Many imaging techniques can potentially detect diseases at very early stages or pick up small changes in signal intensity when an appropriate contrast agent is employed.[3,35]

1.3.1 Imaging with SERS

SERS recently emerged as a new optical imaging modality. The enhancement of Raman signals from probe molecules on a noble-metal particle has allowed this modality to potentially compete with other optical imaging techniques based on fluorescence. By correlating the location of these signals with the peak intensity and wavenumber, SERS signals can be used to construct an image over small areas like a cell, or even larger areas like a tumor.[36-43] Moreover, since SERS bands are much narrower compared with fluorescence peaks, multiplexing of multiple probes, data analysis, and image reconstruction is easier and more accurate.[36,41-45] The narrow bands and unique nature of signals generated from different molecules allow for two or more different probes to be imaged simultaneously. Additionally, only a single excitation source is needed (unlike fluorescent molecules) to generate SERS from an array of different probe molecules. However, SERS imaging has not been thoroughly characterized, and many fundamental parameters such as resolution and penetration depth are still unknown. Additionally, multiplexed imaging requires an appropriate computational algorithm for separating the component spectra from a mixture. While there are several commonly used approaches, there has not been an algorithm developed specifically with SERS analysis in mind.

1.3.2 Magnetic Resonance Imaging

MRI is characterized by high spatial resolution, excellent depth penetration, and non-ionizing radiation, but is expensive, takes a long time to collect an image, and has limited molecular sensitivity.[35] It has therefore been greatly influenced by the use of contrast agents. Though there are ways of optimizing the intrinsic contrast differences between tissues using different imaging protocols, the use of additional contrast enhancement is often necessary for diagnostic or multimodal purposes. Commonly used contrast agents for MRI are iron oxide nanoparticles, gadolinium (Gd^{3+}), manganese oxide, and ^{19}F compounds.[35,46,47] These contrast agents have their pros and cons. While Gd^{3+} is very effective, it is also highly toxic. Iron oxide nanoparticles provide contrast by influencing the surrounding proton responses to the magnetic field, but this can sometimes be difficult to distinguish from background or artifacts in the image. ^{19}F compounds, or perfluorocarbons, have been increasingly studied as positive MRI contrast agents because they provide a clear signal with no native background.[46,48] Much can be improved in the formulation of particles containing perfluorocarbons.

Multimodal applications involving MRI are also increasingly studied. Particles combining an MRI contrast agent such as perfluorocarbons are also commonly found in combination with particles containing other imaging agents such as fluorescent molecules or X-ray contrast agents, or in combination with therapeutic molecules for drug delivery.[48,49-51]

1.3.3 X-ray Computed Tomography

X-ray CT is mainly known for its excellent depth penetration, spatial resolution, and short acquisition time. Major drawbacks include exposure to ionizing radiation and poor soft-tissue contrast.[35] Utilization of contrast agents has completely transformed the functionality of the X-ray CT. Thanks to nanoparticles incorporating materials like iodine, barium, gold, bismuth, and ytterbium, CT imaging can produce high-resolution, three-dimensional images of soft tissues like the gastrointestinal (GI) tract, blood vessels, and tumors.[34,35] However, many of these contrast agents have shortcomings. Heavy metals can be toxic, and thus their applications are limited. Iodinated compounds are commonly used for a wide variety of imaging applications due to their ability to attenuate X-rays, small size, and rapid perfusion rates. However, some iodinating contrast compounds result in severe allergic reactions in some patients and have demonstrated toxicity.[52] A better approach to formulating iodinated contrast compounds could allow their continued use when imaging high-risk patients.

Co-localization of CT with positron emission tomography (PET), now fairly ubiquitous, combined the high spatial resolution and anatomical detail of CT imaging with the functional data of PET for more accurate cancer detection and treatment monitoring. Other multimodal approaches to CT contrast have also been studied, including nanoparticles designed for combining CT and MRI, fluorescence, and drug delivery.[53-55]

1.3.4 Thermoacoustic Tomography

TAT is an imaging modality that combines the good contrast of microwave imaging and high resolution of ultrasound imaging. In TAT, a microwave pulse is used to excite the tissue. The heating of good microwave absorbers results in thermoelastic expansion, producing acoustic waves detected by an ultrasound transducer.[56,57] Although the modality was designed around intrinsic contrast in microwave absorption, there are still some situations in which additional contrast is desirable, such as the early detection of breast cancer. However, the novelty of the imaging modality means very few contrast agents have been studied. Single-walled carbon nanotubes (SWNTs) and microbubbles are

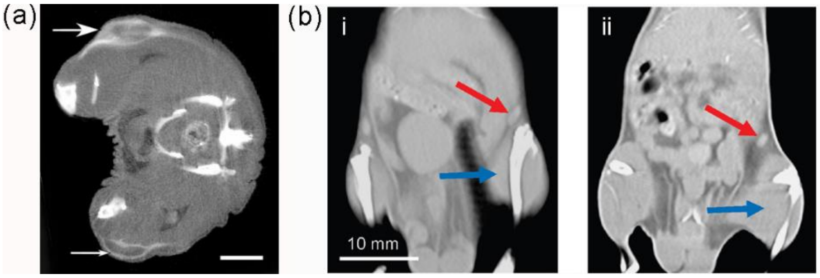

Figure 1.6. Two examples of actively targeted nanoparticle contrast agents. (a) Gold nanoparticles conjugated with antibodies for the human epidermal growth factor receptor (Her2) demonstrate increased contrast in Her2-positive tumors (top arrow) when compared to Her2-negative tumors (bottom arrow). Reproduced with permission from [53]. (b) Nonspecific targeting of Au nanoparticles using IgG (i) shows no contrast enhancement compared with specifically-targeted Anti-CD4 Au nanoparticles (ii) which demonstrate increased contrast in the lymph node (indicated by the red arrows). Adapted with permission from [59]. Copyright 2010 American Chemical Society.

two examples of potential contrast agents for TAT, although SWNTs have long possessed toxicity concerns.[56,58] The microbubbles provide negative contrast, which may not be suitable for all TAT imaging applications. There is much room for improvement in developing a contrast agent for TAT that can potentially provide targeted contrast for early detection.

1.3.5 Particle-based Contrast Agents

An ideal contrast agent not only provides excellent contrast for a given imaging modality, but also selectively localizes in the area of interest and thus reduce the toxicity. Advanced imaging techniques and multimodal applications require targeting the contrast agent to specific tissues (Figure 1.6).[3,53,59] The development of particle-based contrast agents is popular because particles provide improved control over circulation times, a greater density of contrast enhancing molecules, and a substrate for attaching targeting ligands.[3,34,54]

Perhaps the greatest benefit of particle-based contrast agents is their potential for use in multimodal applications. A nanoparticle composed of a contrast enhancing material can then be coated with polymers containing drugs or functionalized with therapeutic antibodies for combinatorial imaging and therapy.[49,60-62] Multi-component nanoparticles can be designed for use as contrast agents in several different imaging modalities, such as MRI and CT, simultaneously.

While most particle-based platforms involve complex chemistry and the layering of materials to achieve targeting and multimodality, the practice of encapsulating an active agent within a particle or other inert shell is also a desirable approach. Encapsulation provides the benefits of particle-based technology with additional improvements in flexibility, control, and preventing toxicity. The use of liposomes for encapsulating drugs, for example, has already improved the delivery of some chemotherapeutics.[63] Advanced hollow particles made of polymers and other materials are also being investigated, and there is much room in this area for innovation. The research presented in this dissertation investigated the use of hollow polymer beads for the simple and flexible encapsulation of imaging contrast agents.

1.4 Scope of this Work

The research objectives of this dissertation were to develop a deeper understanding and broader application of nanoparticles and small microparticles in the areas of medical sensing and imaging. Due to the status of SERS as an effective mode for ultrasensitive detection and its emergence as a potential medical imaging modality, much of the research in this dissertation investigated SERS based on nanoparticle substrates as a platform for ultrasensitive molecular detection, an analytical tool, and an imaging technique.

Additionally, polymer hollow beads were used to encapsulate contrast agents for a variety of medical imaging modalities. This work serves to lay a foundation for SERS as a valuable research tool for monitoring molecules on the surface of nanoparticles, implementing SERS as a viable imaging technique, and proposing a new class of hollow polymeric carriers for multimodal applications.

In Chapters 2 and 3, I elaborate on fundamental studies of SERS, demonstrating its power as a research tool for nanomedicine. The laser polarization, nanoparticle shape, and nanoparticle orientation are known to have tremendous effects on SERS EFs.[25,64-66] I describe a technique designed to streamline correlated studies between SERS and the physical properties of nanoparticles. Correlated studies are critical to identifying particles or aggregates with potentially high EFs for applications requiring ultrasensitive and potentially single-molecule detection. I used SEM to determine the physical parameters of nanoparticles, and then investigated the deposition of amorphous carbon during SEM imaging and its impact on the SERS measurements.[67] Chapter 3 explores the use of SERS as a tool for monitoring the exchange of ligands on the surface of nanoparticles.[68] Since capping agents used to control nanoparticle shape remain attached to the surface post synthesis, the SERS signal from these molecules diminishes at the rate of functional polymer attachment. This work demonstrates that SERS is ideal for not only confirming the presence of functional molecules on the surface, but also the complete removal of contaminants, a vital step for developing nanoparticle-based medical applications for use *in vivo*.

Chapter 4 contains two projects designed to advance SERS imaging as a potential clinical platform. Fundamental parameters for imaging such as resolution and penetration depth were determined.[69] Penetration depth was found to be a major weakness of SERS imaging, although the sensitivity and resolution of SERS imaging are very high. Multiplexing is another great advantage of SERS imaging, but it can be complicated and difficult to execute. A novel algorithm for unmixing SERS signals based on the alternating minimization (AM) method was developed and its efficacy was demonstrated.[45]

Chapter 5 describes novel polymer hollow beads with a single hole on the surface for encapsulating imaging contrast agents. The encapsulation of imaging agents was demonstrated, and the successful enhancement of images for a variety of medical imaging techniques including MRI, X-ray CT, and TAT was shown.[70]

1.5 References

[1] N. L. Rosi and C. A. Mirkin. *Chem. Rev.* 2005, **105**, 1547.

[2] P. Alivisatos. *Nat. Biotech.* 2004, **22**, 47.

[3] M. Mahmoudi, V. Serpooshan, and S. Laurent. *Nanoscale* 2011, **3**, 3007.

[4] Y. Xia, Y. Xiong, B. Lim, and S. E. Skrabalak. *Angew. Chem. Int. Ed.* 2009, **48**, 60.

[5] J. N. Anker, W. P. Hall, O. Lyandres, N. C. Shah, J. Zhao, and R. P. Van Duyne. *Nat. Mater.* 2008, **7**, 442.

[6] K. A. Willets and R. P. Van Duyne. *Annu. Rev. Phys. Chem.* 2007, **58**, 267.

[7] B. J. Wiley, S. H. Im, Z.-Y. Li, J. McLellan, A. Siekkinen, and Y. Xia. *J. Phys. Chem. B* 2006, **110**, 15666.

[8] R. Bardhan, S. Lal, A. Joshi, and N. J. Halas. *Acc. Chem. Research* 2011, **44**, 936.

[9] S. E. Skrabalak, J. Chen, L. Au, X. Lu, X. Li, and Y. Xia. *Adv. Mater.* 2007, **19**, 3177.

[10] K.-S. Lee and M. A. El-Sayed. *J. Phys. Chem. B* 2006, **110**, 19220.

[11] M. S. Yavuz, Y. Cheng, J. Chen, C. M. Cobley, Q. Zhang, M. Rycenga, J. Xie, C. Kim, K. H. Song, A. G. Schwartz, L. V. Wang, and Y. Xia. *Nat. Mater.* 2009, **8**, 935.

[12] S. D. Perrault, C. Walkey, T. Jennings, H. C. Fischer, and W. C. W. Chan. *Nano Lett.* 2009, **9**, 1909.

[13] L. Au, Q. Zhang, C. M. Cobley, M. Gidding, A. G. Schwartz, J. Chen, and Y. Xia. *ACS Nano* 2010, **4**, 35.

[14] C. Grabinski, N. Schaeublin, A. Wijaya, H. D'Couto, S. H. Baxamusa, K. Hamad-Schifferli, and S. M. Hussain. *ACS Nano* 2011, **5**, 2870.

[15] Q. Zhang, W. Li, C. Moran, J. Zeng, J. Chen, L.-P. Wen, and Y. Xia. *J. Am. Chem. Soc.* 2010, **132**, 11372.

[16] A. J. Haes and R. P. Van Duyne. *Anal. Bioanal. Chem.* 2004, **379**, 920.

[17] C. L. Haynes, A. D. McFarland, R. P. Van Duyne. *Anal. Chem.* 2005, **77**, 338A.

[18] W. Xie and S. Schlücker. *Phys. Chem. Chem. Phys.* 2013, **15**, 5329.

[19] M. Fleischmann, P. J. Hendra, and A. J. McQuillan. *Chem. Phys. Lett.* 1974, **26**, 163.

[20] D. L. Jeanmaire and R. P. Van Duyne. *J. Electroanal. Chem.* 1977, **84**, 1.

[21] M. G. Albrecht and J. A. Creighton. *J. Am. Chem. Soc.* 1977, **99**, 5215.

[22] A. Campion and P. Kambhampati. *Chem. Soc. Rev.* 1998, **27**, 241.

[23] M. Moskovits. *Phys. Chem. Chem. Phys.* 2013, **15**, 5301.

[24] E. C. Le Ru, E. Blackie, M. Meyer, and P. G. Etchegoin. *J. Phys. Chem. C* 2007, **111**, 13794.

[25] M. Rycenga, P. H. C. Camargo, W. Li, C. H. Moran, and Y. Xia. *J. Phys. Chem. Lett.* 2010, **1**, 696.

[26] M. Rycenga, M. H. Kim, P. H. C. Camargo, C. Cobley, Z.-Y. Li, and Y. Xia, *J. Phys. Chem. A*, 2009, **113**, 3932-3939.

[27] P. H. C. Camargo, M. Rycenga, L. Au, and Y. Xia. *Angew. Chem. Int. Ed.* 2009, **48**, 2180.

[28] M. Rycenga, X. Xia, C. H. Moran, F. Zhou, D. Qin, Z.-Y. Li, and Y. Xia. *Angew. Chem. Int. Ed.* 2011, **50**, 5473.

[29] C. J. Choi, H. Y. Wu, S. George, J. Weyhenmeyer, and B. J. Cunningham. *Lab Chip* 2012, **12**, 574.

[30] H. Zhang, M. H. Harpster, H. J. Park, and P. A. Johnson. *Anal. Chem.* 2011, **83**, 254.

[31] G. F. Wang, R. J. Lipert, M. Jain, S. Kaur, S. Chakraboty, M. P. Torres, S. K. Batra, R. E. Brand, and M. D. Porter. *Anal. Chem.* 2011, **83**, 2554.

[32] X. Wang, X. Qian, J. J. Beitler, Z. G. Chen, F. R. Khuri, M. M. Lewis, H. J. C. Shin,

S. Nie, and D. M. Shin. *Cancer Res.* 2011, **71**, 1526.

[23] C. M. C. Tempany and B. J. McNeil. *J. Am. Med. Assoc.* 2001, **285**, 562.

[34] Y. Liu, K. Ai, and L. Lu. *Acc. Chem. Res.* 2012, **45**, 1817.

[35] M. A. Pysz, S. S. Gambhir, and J. K. Willman. *Clin. Radiol.* 2010, **65**, 500.

[36] C. L. Zavaleta, B. R. Smith, I. Walton, W. Doering, G. Davis, B. Shojaei, M. J. Natan, and S. S. Gambhir. *Proc. Natl. Acad. Sci.* 2009, **106**, 13511.

[37] J.-H. Kim, J.-S. Kim, H. Choi, S.-M. Lee, B.-H. Jun, K.-N. Yu, E. Kuk, Y.-K. Kim, D. H. Jeong, M.-H. Cho, and Y.-S. Lee. *Anal. Chem*. 2006, **78**, 6967.

[38] M. Y. Sha, H. Xu, M. J. Natan, and R. Cromer. *J. Am. Chem. Soc.* 2008, **130**, 17214.

[39] X. Qian, X.-H. Peng, D. O. Ansari, Q. Yin-Goen, G. Z. Chen, D. M. Shin, L. Yang, A. N. Young, M. D. Wang, and S. Nie. *Nat. Biotech*. 2008, **26**, 83.

[40] S. Lee, S. Kim, J. Choo, S. Y. Shin, Y. H. Lee, H. Y. Choi, S. Ha, K. Kang, and C. H. Oh. *Anal. Chem.* 2007, **79**, 916.

[41] B.-H. Jun, J.-H. Kim, H. Park, J.-S. Kim, K.-N. Yu, S.-M. Lee, H. Choi, S.-Y. Kwak, Y.-K. Kim, D. Jeong, M.-H. Cho, and Y.-S. Lee. *J. Comb. Chem.* 2007, **9**, 237.

[42] L. Sun et al. *Nano Lett.* 2007, **7**, 351.

[43] S. Keren, C. Zavaleta, Z. Cheng, A. de la Zerda, O. Gheysens, and S. S. Gambhir. *Proc. Natl. Acad. Sci.* 2008, **105**, 5844.

[44] B. R. Lutz, C. E. Dentinger, L. N. Nguyen, L. Sun, J. Zhang, A. N. Allen, S. Chan, and B. Knudsen. *ACS Nano* 2008, **2**, 2306.

[45] Y. Chen, C. H. Moran, Z. Tan, A. L. Wooten, and J. A. O'Sullivan. *J. Raman Spectrosc.* 2013, **44**, 703.

[46] U. Flögel, Z. Ding, H. Hardung, S. Jander, G. Reichmann, C. Jacoby, R. Schubert, and J. Schrader. *Circulation* 2008, **118**, 140.

[47] S. T. Selvan, T. T. Y. Tan, D. K. Yi, and N. R. Jana. *Langmuir* 2010, **26**, 11631.

[48] G. M. Lanza, P. M. Winter, A. N. Neubauer, S. D. Caruthers, F. D. Hockett, and S. A. Wickline. *Curr. Topics Dev. Biol.* 2005, **70**, 57.

[49] J. Yang, C.-H. Lee, H.-J. Ko, J.-S. Suh, H.-G. Yoon, K. Lee, Y.-M. Huh, and S. Haam. *Angew. Chem. Int. Ed.* 2007, **46**, 8836.

[50] Y. T. Lim, Y.-W. Noh, J.-H. Cho, J. H. Han, B. S. Choi, J. Kwon, K. S. Hong, A. Gokarna, Y.-H. Cho, and B. H. Chung. *J. Am. Chem. Soc.* 2009, **131**, 17145.

[51] L. Wang, K. G. Neoh, E.-T. Kang, and B. Shuter. *Biomaterials* 2011, **32**, 2166.

[52] J. J. Pasternak and E. E. Williamson. *Mayo Clin. Proc.* 2012, **87**, 390.

[53] J. F. Hainfeld, M. J. O'Connor, F. A. Dilmanian, D. N. Slatkin, D. J. Adams, and H. M. Smilowitz. *Br. J. Radiol.* 2011, **84**, 526.

[54] D. P. Cormode, P. A. Jarzyna, W. J. M. Mulder, and Z. A. Fayed. *Adv. Drug Delivery Rev.* 2010, **62**, 329-338.

[55] D. Kim, M. K. Yu, T. S. Lee, J. J. Park, Y. Y. Jeong, and S. Jon. *Nanotechnology* 2011, **22**, 155101.

[56] A. Mashal, J. H. Booske, and S. C. Hagness. *Phys. Med. Biol.* 2009, **54**, 641.

[57] M. Xu and L. V. Wang. *Med. Phys.* 2002, **29**, 1661.

[58] M. Pramanik, M. Swierczewska, D. Green, B. Sitharaman, and L. V. Wang. *J. Biomed. Opt.* 2009, **14**, 034018.

[59] W. Eck, A. I. Nicholson, H. Zentgraf, W. Semmler, and S. Bartling. *Nano Lett.* 2010, **10**, 2318-2322.

[60] Z. Fan, M. Shelton, A. K. Singh, D. Senapati, S. A. Khan, and P. C. Ray. *ACS Nano* 2012, **6**, 1065.

[61] K. Park, S. Lee, E. Kang, K. Kim, K. Choi, and I. C. Kwon. *Adv. Funct. Mater.* 2009, **19**, 1553.

[62] H. Kobayashi, M. R. Longmire, M. Ogawa, and P. L. Choyke. *Chem. Soc. Rev.* 2011, **40**, 4626.

[63] S. T. Duggan and G. M. Keating. *Drugs* 2011, **71**, 2531.

[64] Q. Zhang, C. H. Moran, X. Xia, M. Rycenga, N. Li, and Y. Xia. *Langmuir* 2012, **28**, 9047.

[65] J. M. McLellan, Z.-Y. Li, A. R. Siekkinen, and Y. Xia. *Nano Lett.* 2007, **7**, 1013.

[66] W. Li, P. H. C. Camargo, X. Lu, and Y. Xia. *Nano Lett.* 2009, **9**, 485.

[67] C. H. Moran, X. Xia, and Y. Xia. *Phys. Chem. Chem. Phys.* 2013, **15**, 5400.

[68] C. H. Moran, M. Rycenga, Q. Zhang, and Y. Xia. *J. Phys. Chem. C* 2011, **115**, 21852.

[69] C. H. Moran, M. Rycenga, X. Xia, C. M. Cobley, and Y. Xia. *Nanotechnology* 2014, in press.

[70] M.-Y. Bai, C. H. Moran, L. Zhang, C. Liu, Y. Zhang, L. V. Wang, and Y. Xia. *Adv.*

Funct. Mater. 2012, **22**, 764.

CHAPTER 2: CORRELATING SERS MEASUREMENTS WITH STRUCTURAL PARAMETERS

2.1 Introduction

As discussed in Chapter 1, SERS can be used for labeled or label-free detection of small molecules, proteins, and cell types. In labeled detection, the sensitivity is optimized by choosing an appropriate Raman-active reporter molecule and designing the nanoparticle system accordingly. For *in vivo* detection or imaging, an NIR laser will likely be used to reduce the absorption and scattering of the light by blood and tissue.[1] Therefore, selecting a Raman reporter that exhibits high absorption in that range, such as an NIR fluorescent dye, will produce large EFs.[2] This phenomenon has its own name: surface-enhanced resonance Raman spectroscopy (SERRS).[2,3] Additionally, inclusion of hot-spots by choosing nanoparticles with sharp corners, such as Ag nanocubes, or involvement of nanoparticle aggregation, can also increase EFs.[4,5]

With label-free detection, the molecule of interest will likely not experience resonant absorption at the excitation frequency. As a result, the attempts to control enhancement fall solely on optimizing the SERS substrates.[6-8] Creating nanoparticle arrays or aggregates with built-in hot-spots can optimize EFs in a label-free detection system.[8,9] Therefore, the goal of many fundamental studies of SERS is to isolate hot-spots and design substrates for single-molecule (SM) detection. A substrate sensitive enough for SM detection would have tremendous potential for biosensing.[10-12]

A systematic study of the relationship between the SERS spectrum of an individual nanoparticle, or assembly of nanoparticles, and its physical parameters and orientation is vital for the effort to achieve the largest possible enhancement. To this end, several approaches have been demonstrated to correlate the SERS spectrum of a nanoparticle with its structural parameters. Electron microscopy (EM) or atomic force microscopy (AFM) can provide detailed and high-resolution images of the nanoparticles and their physical parameters. Of all the nanoscale imaging techniques, SEM imaging has proven to be a simple yet effective means to obtain details about the morphology of a nanoparticle.[13] For assemblies of spherical nanoparticles, optical techniques based on the polarization effect have been used to determine the orientation of the aggregates.[14,15] However, for nanoparticles with anisotropic shapes, such as the Ag nanocubes used here, a more definite imaging technique like SEM is necessary.

2.2 Silver Nanocubes: Synthesis and Plasmonic Properties

2.2.1 Synthesis of Silver Nanocubes

In a typical synthesis, single-crystal Ag seeds in a spherical or cubic shape were first prepared using a polyol process developed in the Xia group that used silver trifluoroacetate (CF_3COOAg) as a precursor to elemental Ag.[16] The seeds were collected and then mixed with Ag nitrate ($AgNO_3$) in ethylene glycol at an elevated temperature to generate Ag nanocubes. Mechanistic studies indicated that oxidative etching played an important role in the seed-mediated growth of Ag nanocubes. When $AgNO_3$ was used for the polyol process, HNO_3 was formed during the synthesis,[17] which could serve as an oxidative etchant to block the homogeneous nucleation of Ag atoms and the evolution of single-crystal seeds into twinned nanoparticles.

The size of the resultant Ag nanocubes could be reliably controlled by any one of the following means: i) quenching the reaction once the LSPR peak had reached a specific position; ii) varying the amount of $AgNO_3$ precursor mixed with a specific quantity of Ag

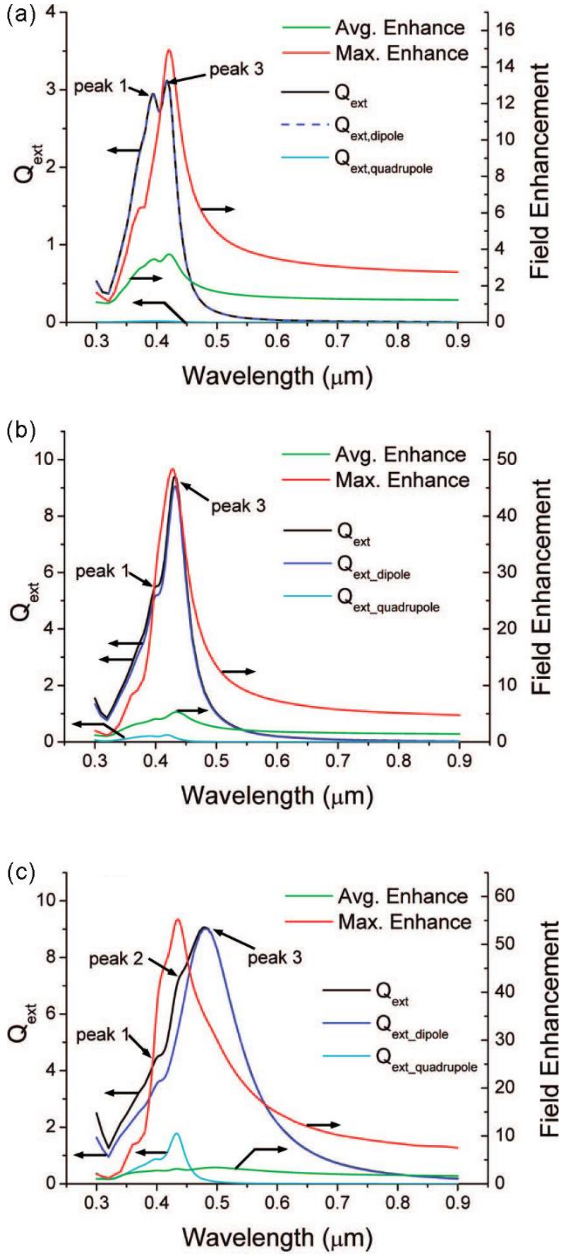

Figure 2.1. UV-vis spectra calculated for Ag nanocubes with edge lengths of (a) 20 nm, (b) 50 nm, and (c) 90 nm. The contributions from the dipole and quadrupole resonances are compared. That calculated field enhancement is also plotted.[20] Adapted with permission from J. Phys. Chem. C. Copyright 2008 American Chemical Society.

seeds; and iii) varying the quantity of Ag seeds added into a specific amount of $AgNO_3$ precursor.[18] Typically, the LSPR was used as a reliable means for determining Ag nanocube size during the reaction.

2.3 The Effect of Nanocube Orientation and Laser Polarization on SERS

As explained in Chapter 1, the SERS phenomenon depends on the LSPR of the substrate, of which I will only be concerned with nanoparticles. If the nanoparticle is anisotropic, such as a cube or bar, it will have multiple LSPR peaks. For example, UV-vis absorbance spectroscopy reveals that Ag nanocubes have several LSPR peaks (Figure 2.1) reflecting the different resonance modes of Ag nanocubes.[19,20] The two peaks visible in smaller Ag nanocubes arise from the dipole resonance modes along the sides of the nanocube, which is split due to the sharp corners. The third peak that appears when the Ag nanocubes grow above 90 nm in edge length results from the quadrupole mode associated with the corners of the nanocube.[20,21] When the Ag nanocube is placed on a substrate, as in single particle SERS studies, there arises a separation between the modes distal and proximal to the substrate.[21] As a result, in single particle studies, the polarization and wavelength of the incident light matter to a great deal. Individual LSPR modes can be activated by aligning the resonance mode and the laser polarization, or matching the laser wavelength and the LSPR peak. If the wavelength of the laser is very close to the LSPR mode, the intensity of the electric field will be maximized, and the SERS spectra will experience its optimal EF, as the Xia group has demonstrated with Ag nanobars in Figure 2.2.[22] For Ag nanocubes, the SERS EFs were maximized when the face diagonal of the Ag nanocube was aligned parallel to the excitation laser polarization.[23]

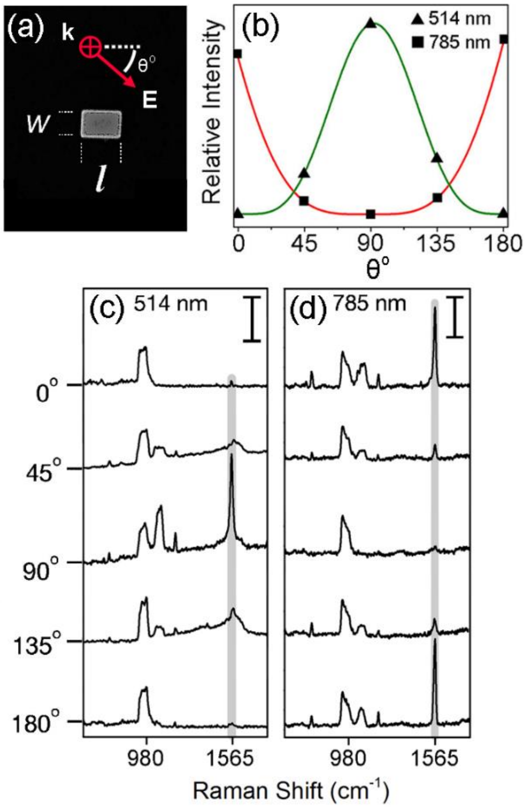

Figure 2.2. The alignment of the polarization and wavelength of the incident laser with particular LSPR modes of Ag nanobars has a major impact on SERS enhancement. (a) An SEM image of a typical Ag nanobar with an aspect ratio of 2. The laser polarization angle, θ, was defined relative to the longitudinal axis of the nanobar. The LSPR modes of nanobars are separated into longitudinal and transverse modes corresponding to its physical dimensions. The transverse LSPR peak is about 450 nm and the longitudinal LSPR peak is about 650 nm for this nanobar. (b) The SERS intensity plotted a function of θ, with the fit to $\cos^4(\theta)$. When both the wavelength and polarization angle of the laser were aligned with the corresponding LSPR mode in the nanobar, SERS signals were maximized. (c,d) SERS spectra were plotted for the 514 nm and 785 nm lasers at different polarization angles.[22] Reprinted with permission from Langmuir. Copyright 2012, American Chemical Society.

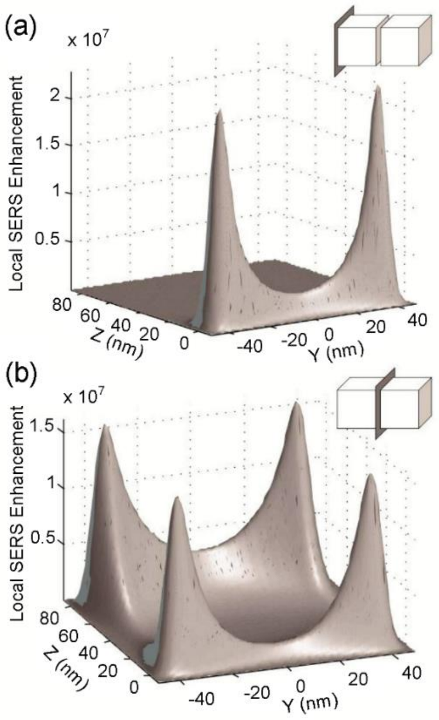

Figure 2.3. The SERS enhancement map for a dimer of Ag nanocubes on the (a) outer face of the dimer and (b) gap between the faces of the Ag nanocubes. The sharp peaks are areas of great SERS enhancement, known as hot spots.[24] Adapted with permission from ACS Nano. Copyright 2010 American Chemical Society.

The orientation and shape of anisotropic nanoparticles will also influence the location and strength of the hot spots. Hot spots are small regions of exceptionally high E-fields typically resulting from an antenna-like effect at the sharp corners of Ag nanocubes or of the interaction of the LSPRs of two or more nanoparticles, as shown in Figure 2.3.[24] Molecules located in the hot spot will experience much greater enhancement than molecules located elsewhere. In theory, probing the hot spots could allow for the collection of SERS signal from a single molecule.[10,12]

2.4 Correlating SERS with Structural Parameters

Using SEM to image the Ag nanocubes is convenient because a variety of substrates can be used, unlike other nanoscale imaging techniques like TEM. Preparation of SEM samples is also simple and they can be directly transferred into a Raman microscope. Here a Si wafer was used as the substrate but both Au and Ag substrates can also be used to further enhance the SERS signals.[12] A typical correlated SERS/SEM measurement is conducted by first recording the SERS spectra from nanoparticles that have been functionalized with probe molecules and then deposited on a substrate with registration marks. Afterwards, structural information about the nanoparticles is collected by SEM imaging.[12,25] This procedure is ineffective since it requires one to collect spectra from a large number of particles, only to find after SEM imaging that the majority of the data are useless. Obviously, it will be more efficient to know the morphology and orientation of the nanoparticle first so that collection of SERS spectra can be targeted.

The potential drawback of using SEM is that amorphous carbon will be deposited on the sample during exposure to the electron beam (e-beam) in a process known as electron beam-induced deposition (EBID).[26-31] The deposited amorphous carbon contaminates the surface, and could obstruct further functionalization of the nanoparticles with probe molecules, not to mention the introduction of unwanted background Raman signals. However, I found that choosing the SEM parameters wisely could reduce EBID, and that the deposited amorphous carbon could be removed using several simple ways.

2.4.1 The Effect of Carbon Deposition in SEM on SERS Spectra

In a simple demonstration of EBID, Ag nanocubes deposited on a TEM grid were imaged by the SEM at a tilt angle of 45° relative to the incoming e-beam. The faces of the nanocube exposed to the e-beam were coated with a noticeable carbon layer when viewed afterward head-on under TEM, as shown in Figure 2.4(a).[13] While EBID is useful for a

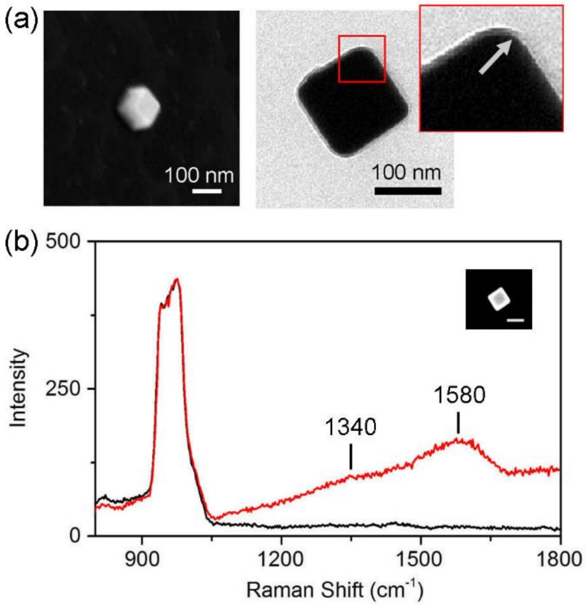

Figure 2.4. Deposition of carbon on Ag nanocubes during SEM imaging was confirmed by both TEM imaging and SERS measurements. (a) After SEM imaging at a 45° tilt angle (left), the Ag nanocube was imaged head-on in the TEM (right). Carbon was only deposited on the exposed faces, as indicated by the arrow in the inset. (b) SERS spectra taken from a single 100-nm Ag nanocube before (bottom trace) and after SEM imaging (top trace). The broad SERS peaks correspond to the bands of amorphous carbon. Each SERS spectrum represents the average from 15-20 similar Ag nanocubes, and one of them is shown in the inset (scale bar: 100 nm). The polarization of the excitation laser was parallel to the face diagonal of the Ag nanocube.[13] Reproduced by permission of the PCCP Owner Societies.

variety of applications,[26,28,32] it is a potential problem for SERS applications, which are extremely sensitive to surface contamination.

Prior to SERS measurements, SEM easily identified individual Ag nanocubes on a marked Si substrate with particular orientations allowing for targeted and more efficient experiments. Nanocubes with the side diagonal parallel to the laser polarization, as shown in the inset of Figure 2.4(b), were chosen due to the polarization dependence of LSPR excitation.[23] After SEM imaging, the average SERS spectrum collected from a set of Ag nanocubes shown in Figure 2.4(b) indicated that the material that had been deposited was

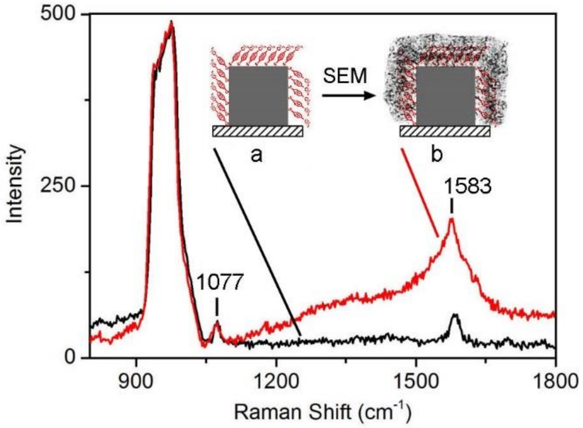

Figure 2.5. The SERS spectrum of 4-MBT adsorbed on the 100-nm Ag nanocubes before SEM imaging (a) was retained after SEM imaging (b). However, the background from deposition of carbon was detected under the 4-MBT peaks after SEM imaging (b). The SERS peaks from 4-MBT were at 1077 cm^{-1}, a combination of the benzene ring breathing and CH in-plane bending modes, and at 1583 cm^{-1}, the benzene ring C-C stretching. The broad peak from 930-1000 cm^{-1} was from the Si substrate, and was used to normalize all the spectra. Each SERS spectrum represents the average from 15-20 similar Ag nanocubes with similar orientation relative to laser polarization. The SEM was operated at 15 kV, with a current of 0.24 nA. [13] Reproduced by permission of the PCCP Owner Societies.

essentially amorphous carbon. The two major features in this spectrum were the broad peaks centered at 1580 and 1340 cm^{-1}, which can be assigned to the E_{2g} zone center mode of graphite (or G-band) and the disorder-induced band (or D-band), respectively.[31-36]

As shown in Figure 2.5, if the Ag nanocubes were first functionalized with 4-MBT, the SERS signals from 4-MBT on those nanocubes were still detectable even after EBID. The deposited carbon did not cause any major changes to the SERS peaks of 4-MBT; the intensity of the peak at 1077 cm^{-1}, a combination of the benzene ring breathing and CH in-plane bending modes (7a vibrational mode),[37-39] remained the same before and after the deposition of amorphous carbon. The other major peak at 1583 cm^{-1}, the benzene ring C-C stretching (8a vibrational mode),[38,39] did not show any increase in intensity, but rather was superimposed on the background spectrum from carbon.

These observations imply that the deposition of amorphous carbon came from vapor phase hydrocarbon contaminants in the vacuum chamber, and it was not caused by degradation of the probe molecules adsorbed on the surface of a Ag nanocube. These results are additionally supported by a body of research indicating that self-assembled monolayers (SAMs) of aromatic compounds were more stable than aliphatic SAMs under the irradiation of low-energy electrons.[40,41] Instead of breaking down the probes, the e-beam might just cross-link adjacent carbon rings.[40,41] Note that the beam energy used in my study was even lower than what were used in many of the prior cross-linking studies (15 kV compared to 50 kV), suggesting that the level of cross-linking was low enough to not affect the SERS spectra.

Since the 4-MBT monolayer was not disturbed by the deposition of amorphous carbon during SEM imaging, SERS probe molecules with strong peaks outside the range of the carbon background, and preferably aromatic compounds, can be intentionally chosen for correlated SEM/SERS analysis. It should be pointed out that there are many cases where functionalization of nanoparticles should be performed after SEM imaging. In order to determine the impact of the amorphous carbon on the ability to functionalize the Ag nanocubes post SEM imaging, I investigated the dependence of carbon deposition on e-beam current and exposure time, and then evaluated its impact on the SERS signals coming from the probe molecules.[26-28]

I initially considered the effect of e-beam exposure time on the deposition of carbon. I found that more carbon was deposited onto the surface of the Ag nanocubes when the e-beam exposure time was increased, as shown by the TEM images in Figure 2.6(a). As expected, the SERS signals from carbon also increased dramatically with the exposure time

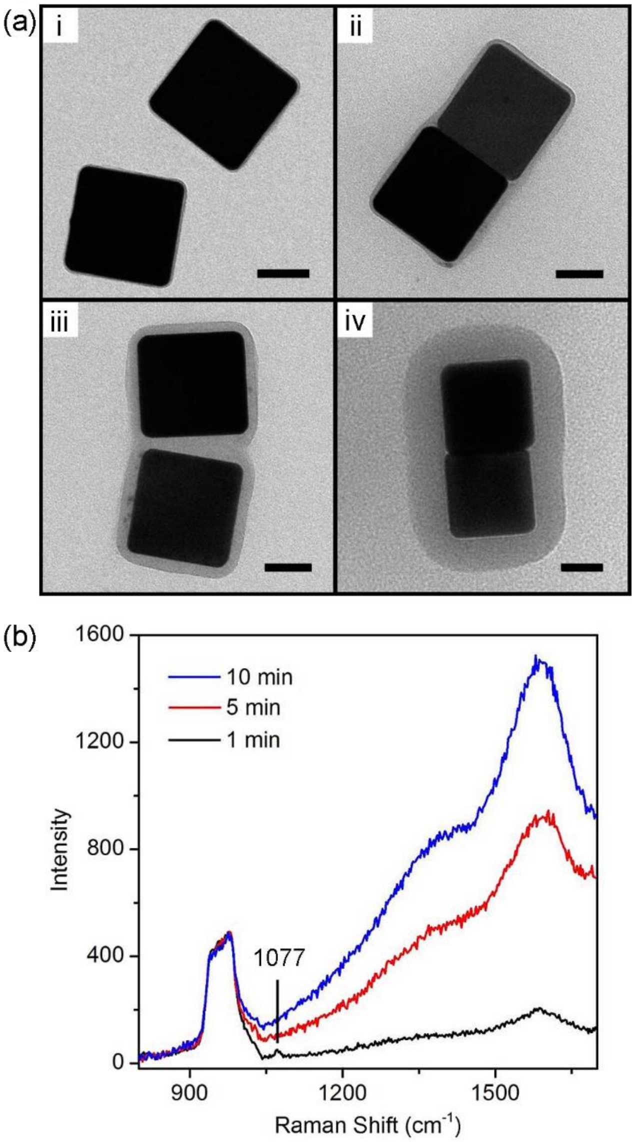

Figure 2.6. (a) TEM images of Ag nanocubes (i) that had not been exposed to the e-beam, and after exposure to the e-beam at 15 kV and 0.24 nA for (ii) 1 min, (iii) 5 min, and (iv) 15 min. All scale bars are 50 nm. (b) The duration of exposure of Ag nanocubes to the e-beam affects not only the amount of carbon deposited, but also the capability of the Ag nanocubes for functionalization. The individual 100-nm Ag nanocubes on a Si substrate were exposed to the e-beam for 1, 5, and 10 min, at a voltage of 15 kV and a current of 0.24 nA. The samples were then immersed in 1 mM 4-MBT for functionalization for 1 h prior to recording of the SERS spectra.[13] Reproduced by permission of the PCCP Owner Societies.

as shown in Figure 2.6(b). This thicker layer of carbon made it more difficult for 4-MBT molecules to access the Ag surface during modification, and Figure 2.6(b) shows that the SERS signals from 4-MBT became very weak even just after 5 min of EBID.

Besides exposure time, the e-beam current was found to have an impact on the deposition of carbon. Three substrates with Ag nanocubes deposited were first imaged in the SEM for 1 min at currents of 0.24, 0.49, and 1 nA prior to functionalization with 4-MBT (Figure 2.7). While the SERS intensities of the amorphous carbon peaks did not change significantly between the three samples, the intensities from 4-MBT decreased as the current was increased, suggesting that fewer 4-MBT molecules were able to access the Ag surface. Increasing beam current generally resulted in a higher rate of carbon deposition

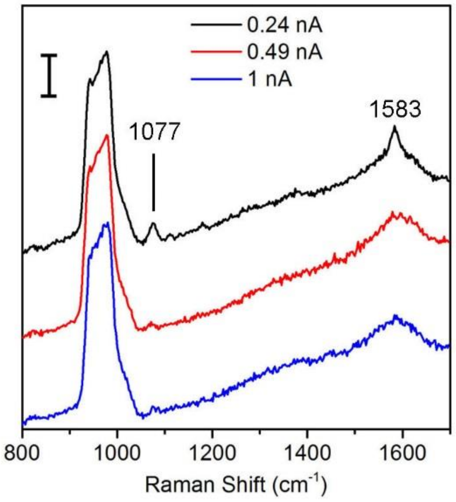

Figure 2.7. Three different samples of Ag nanocubes were imaged in the SEM at three different currents of 0.24, 0.49, and 1 nA. After imaging, the samples were functionalized with 4-MBT (1 mM in ethanol) for 1 h. The SERS intensity of 4-MBT on Ag nanocubes imaged at higher currents was much lower than those imaged at a lower current, but all showed broad peaks from amorphous carbon with the same intensities between 1340 and 1580 cm^{-1}. The peak at 1077 cm^{-1} represents a combination of the benzene ring breathing and CH bending modes from 4-MBT. The scale bar is 100 counts.[13] Reproduced by permission of the PCCP Owner Societies.

until a point of saturation was reached.[29] The currents used in this study were higher than the saturation point, which was reported to be around 0.1 nA.[29,30] Since there were no observable changes to the carbon SERS intensity or carbon layer thickness, the decreased accessibility of 4-MBT to the Ag surface is likely related to a scenario in which nanocubes imaged at a higher beam current might have a denser film of carbon deposited on the surface. If deposition of carbon is not the goal, the impact of EBID on the SERS measurements can be reduced by minimizing the current used and shortening the time exposed to the e-beam when the sample is imaged under SEM.

2.4.2 Removal and Replacement of Amorphous Carbon

In addition to manipulation of the conditions under which the SEM images are taken, I would ideally remove the deposited carbon to greatly reduce its SERS background and simultaneously improve the ability of SERS probes to access the Ag surface. It is obvious from Figures 2.6 and 2.7 that simply immersing the sample for a short period of time in a dilute solution of thiol-based analyte was not enough to remove the carbon layer. However, it is highly possible to replace the deposited amorphous carbon with a thiol molecule that can form a SAM on Ag surface.[33] Incorporating a series of washing steps into the functionalization process can potentially lead to complete removal of the carbon, while forming a SAM of the analyte.

To replace carbon with thiol molecules, only the Ag nanocubes with diagonal orientations were located using the SEM operating at the standard settings (15 kV, 1 min, 0.24 nA), and then the entire substrate was immersed in a 1 mM solution of 4-MBT in ethanol. After 1 min, the substrate was removed from the 4-MBT solution, rinsed with ethanol and deionized (DI) water, and SERS spectra were collected from the imaged Ag

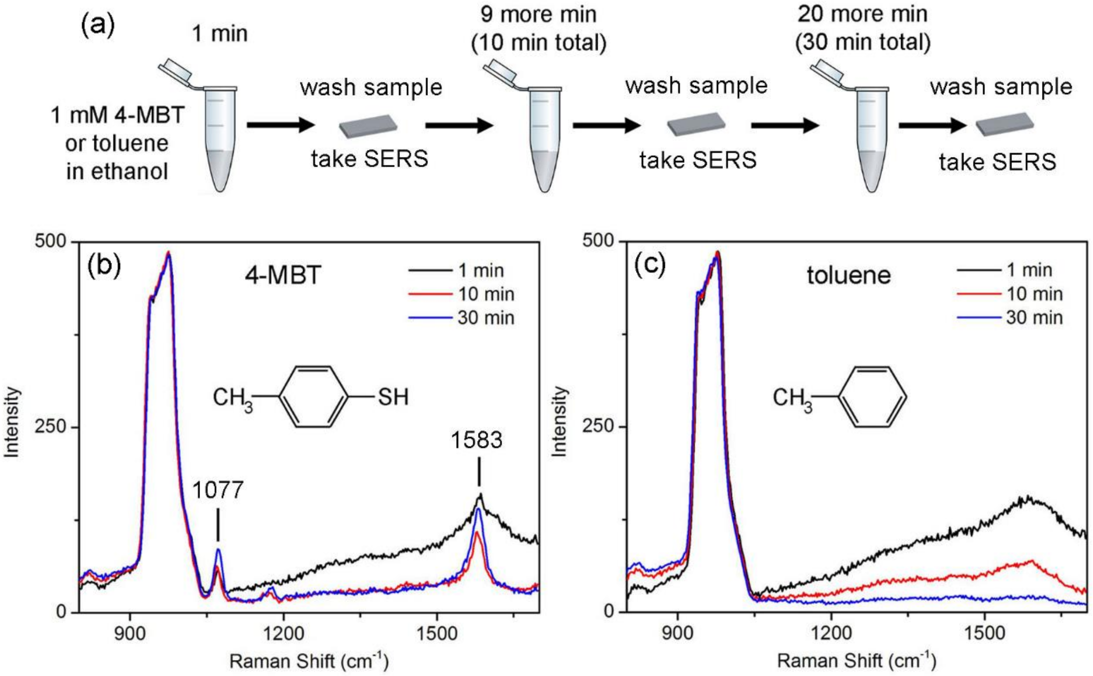

Figure 2.8. The amorphous carbon could be removed by repeatedly immersing the samples in a thiol or toluene solution in ethanol and then washing with ethanol and DI water. Prior to SERS measurements, the Ag nanocubes were imaged using the SEM on a Si substrate (1 min, 15 kV, 0.24 nA). (a) A schematic of the experimental process. The SERS spectra collected over time from the SEM-imaged Ag nanocubes after immersion in (b) a 4-MBT solution and (c) a toluene solution showed a marked decrease in signal from carbon after just 10 min immersion and essential disappearance after 30 min. The scale bars in both (b) and (c) are 100 counts.[13] Reproduced by permission of the PCCP Owner Societies.

nanocubes. The substrate was returned to the 4-MBT solution for another 9 min, or for a total immersion time of 10 min. The process was repeated as schematically illustrated in Figure 2.8(a), and the SERS spectra shown in Figure 2.8(b) indicate that after only 10 min, the signals from the amorphous carbon were substantially reduced, and essentially disappeared after a total of 30 min. This observation demonstrated that the carbon layer was not bound strongly to the Ag surface. Interestingly, I found that the carbon layer could also be washed away by toluene using a procedure similar to what was used for the 4-MBT solution, as shown in Figure 2.8(c).

When 4-MBT was used, the strength of the Ag-S bond was able to overcome the Ag-C interaction. The surface of a Ag nanocube was simultaneously cleaned and functionalized for SERS measurements. The toluene most likely acted as a good solvent for the amorphous carbon. Since the expected SERS signals were not detected from the Ag nanocubes after toluene treatment,[42] the toluene molecules did not adsorb onto the surface, but washed off the carbon, and presumably left behind an exposed Ag surface available for the adsorption of other SERS probes.

In addition to the aforementioned two methods, plasma etching was also found to be capable of removing much of the amorphous carbon layer (see the experimental details in Section 2.6.2 for complete procedure). After imaging two samples of Ag nanocubes on a Si wafer with the standard SEM protocol, one of them was directly functionalized with 4-MBT, while the other was plasma etched for 4 min and then functionalized. The short exposure time was effective in removing the carbon while minimizing the oxidation of Ag

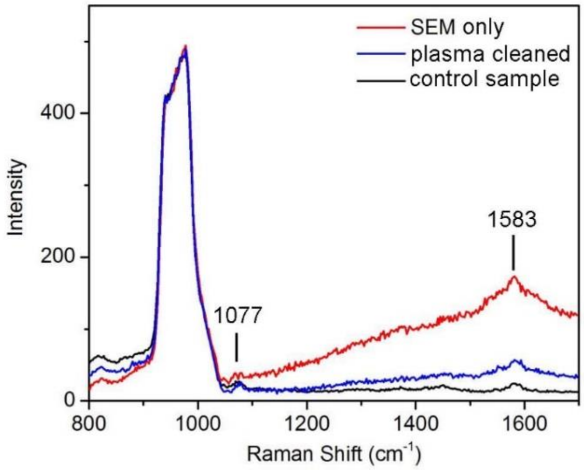

Figure 2.9. Much of the amorphous carbon was removed through plasma etching. After SEM imaging, the Ag nanocubes were derivatized with 4-MBT directly (red) or subjected to plasma etching for 4 min prior to functionalization (blue). As a control, Ag nanocubes with no e-beam exposure were functionalized and included for comparison (black).[13] Reproduced by permission of the PCCP Owner Societies.

surface.[25] Figure 2.9 shows that without plasma etching, amorphous carbon provided a strong background which made the SERS signal from 4-MBT difficult to detect. After plasma etching, this background was greatly reduced, indicating the removal of most of the carbon layer. The spectrum from 4-MBT was nearly identical when collected from the plasma treated sample and from the negative control sample, which was not exposed to SEM or plasma, confirming that the Ag nanocubes were not adversely affected by the plasma treatment. It should be pointed out that the conditions for functionalizing particles and collecting SERS spectra were the same for both Figure 2.5 (curve a) and Figure 2.9. The difference in intensity for the SERS peaks can be attributed to the fact that the nanocubes used to generate the data for Figure 2.9 were from the same original batch as those used in Figure 2.5, only they had been stored in aqueous suspension for several months. It is well documented that this aging process contributes to rounding of the corners of the cubes.[16,43] As a result, the SERS spectra tend to be less intense due to the diminishing intensity of the hot spot.[43]

2.5 Summary

For SERS to be valuable for biosensing, the EFs must be optimized, ensuring high sensitivity for unlabeled detection and high efficiency for labeled detection. Detecting single molecules is the ultimate goal of many fundamental SERS studies, and understanding the link between the structural parameters of a SERS substrate and the resulting SERS EFs is the key. Imaging nanocubes on a substrate prior to collecting SERS measurements is the most effective way for performing correlated SERS studies, and also for checking the quality of SERS substrates in biosensing applications. Using the SEM is the simplest, most efficient imaging modality for this purpose, and I found that the background signals from the EBID that results from using the SEM can be mitigated by washing the substrate, or using plasma cleaning. The EBID can be reduced by optimizing SEM settings such as beam current and exposure time, as well.

2.6 Experimental Details

2.6.1 Preparation of Ag Nanocubes for Use as SERS Substrates

The Ag nanocubes were synthesized using a seed-mediated growth method.[18] In brief, single-crystal, Ag spherical seeds of 30 nm in diameter were prepared by reducing silver trifluoroacetate (CF_3COOAg, Aldrich) to elemental silver in ethylene glycol (EG, J. T. Baker). The seeds were then allowed to grow in the presence of silver nitrate ($AgNO_3$, Aldrich) and poly(vinyl pyrrolidone) (PVP, $M_W \approx 55,000$, Aldrich) as the Ag precursor and capping agent, respectively. The edge length could be controlled by varying the length of the reaction time or the concentration of $AgNO_3$ added.[18] For obtaining 100-nm Ag nanocubes, the reaction was quenched with an ice-water bath when the major LSPR peak reached 585 nm. The Ag nanocubes were washed first with acetone, and then three times with DI water to remove excess EG and PVP. The final product was suspended in ethanol at a typical concentration of 10^{10}-10^{11} particles/mL for further use.

The seeds and 100-nm Ag nanocubes were characterized by a UV-vis spectrometer (Varian, Cary 50), a SEM (FEI, Nova NanoSEM 2300) operated at an accelerating voltage of 15 kV, and a TEM (FEI, G2 Spirit) operated at 120 kV.

2.6.2 SERS Substrate Preparation and SEM Imaging

The samples for SERS measurements were prepared by drop-casting a dilute (at a concentration of 10^7 particles/mL) suspension of Ag nanocubes in ethanol onto a small piece of Si wafer containing registration marks. Unless otherwise specified, functionalization of the 100-nm Ag nanocubes with 4-MBT (Sigma) was carried out by submerging the entire Si substrate in a 4-MBT solution in ethanol (1.0 mM) for 60 min either before or after SEM imaging. Functionalization for SERS measurements at different time points was performed by submerging the sample for 1 min in a 1 mM solution of either 4-MBT or toluene (Aldrich), then washing with copious amounts of ethanol and DI water. After taking the SERS spectra, the substrate was returned to the solution of 4-MBT or toluene. This process was repeated such that the substrate experienced cumulative exposure time to the solution of 10 min and 30 min. The SEM was typically operated at an accelerating voltage of 15 kV with a beam current of 0.24 nA. In a current dependent study, I also used e-beam currents of 0.49 nA and 1 nA. Exposure time was typically 1 min, but in some cases varied as noted. Plasma etching was employed as a possible means to remove the carbon coating. Samples were exposed to the plasma for 4 min with the power being set to “high”.

TEM imaging was also used to observe the carbon deposited on the Ag nanocubes during SEM imaging. In this case, a small volume of the Ag nanocubes suspended in ethanol was dropped onto a standard Cu TEM grid and allowed to dry. Small areas of the Cu grid were then imaged by the SEM using the standard settings for exposure times ranging from 1 to 15 min. The same areas of the Cu grid were then imaged using the TEM to confirm the variation in thickness for the deposited carbon.

2.6.3 Correlated SEM/SERS Measurements

The SERS spectra were recorded using a Renishaw inVia confocal Raman spectrometer coupled with a Leica microscope with a 50x objective (NA = 0.09). The excitation wavelength used was 514 nm generated by an Ar laser (5 mW) equipped with a holographic notch filter with a grating of 1200 lines/mm. The backscattered Raman signals were collected on a thermoelectrically cooled (-60 °C) CCD detector. Individual Ag nanocubes that had been targeted by SEM imaging were located on the substrate under dark-field illumination. Spectra were collected at 0.5 mW for 45 sec from each Ag nanocube. All SERS plots represent an average of the spectra acquired from 15-20 individual nanocubes of approximately the same size and orientation.

Data processing for the SERS spectra was performed using OriginPro v. 8.5.1, Student version (OriginLab, Corp., Northampton, MA). All data was baseline-corrected by subtracting the minimum from the data. The spectra were normalized to the peak of Si at 920-1000 cm^{-1}.

2.7 References

[1] V. Ntziachristos, C. Bremer, and R. Weissleder. *Eur. Radiol.* 2003, **13**, 195.

[2] X. Qian, X.-H. Peng, D. O. Ansari, Q. Yin-Goen, G. Z. Chen, D. M. Shin, L. Yang, A. N. Young, M. D. Wang, and S. Nie. *Nat. Biotech*. 2008, **26**, 83.

[3] D. Cunningham, R. E. Littleford, W. E. Smith, P. J. Lundahl, I. Khan, D. W. McComb, D. Graham, and N. Laforest. *Faraday Discuss.* 2006, **132**, 135.

[4] L. Sun et al. *Nano Lett.* 2007, **7**, 351.

[5] J.-H. Kim, J.-S. Kim, H. Choi, S.-M. Lee, B.-H. Jun, K.-N. Yu, E. Kuk, Y.-K. Kim, D. H. Jeong, M.-H. Cho, and Y.-S. Lee. *Anal. Chem*. 2006, **78**, 6967.

[6] M. Culha. *Appl. Spectrosc.* 2013, **67**, 355.

[7] M. Moger, P. Gribbon, A. Sewing, and C. P. Winlove. *Biochim. Biophys. Acta* 2007, **1770**, 912.

[8] Z. Yi, X.-Y. Li, F.-J. Liu, P.-Y. Jin, X. Chu, and R.-Q. Yu. *Biosens. Bioelectron.* 2013, **43**, 308.

[9] X. X. Han, G. G. Huang, B. Zhao, and Y. Ozaki. *Anal. Chem.* 2009, **81**, 3329.

[10] X.-M. Qian, and S. M. Nie. *Chem. Soc. Rev.* 2008, **37**, 912.

[11] A. M. Michaels, J. Jiang, and L. Brus. *J. Phys. Chem. B* 2000, **104**, 11965.

[12] M. Rycenga, X. Xia, C. H. Moran, F. Zhou, D. Qin, Z.-Y. Li, and Y. Xia. *Angew. Chem. Int. Ed.* 2011, **50**, 5473.

[13] C. H. Moran, X. Xia, and Y. Xia. *Phys. Chem. Chem. Phys.* 2013, **15**, 5400.

[14] T. Shegai, B. Brian, V. D. Miljković, and M. Käll, *ACS Nano*, 2011, **5**, 2036-2041.

[15] S. M. Stranahan, E. J. Titus, and K. A. Willets, *J. Phys. Chem. Lett.*, 2011, **2**, 2711-2715.

[16] Q. Zhang, W. Li, L.-P. Wen, J. Chen, and Y. Xia. *Chem. Eur. J.* 2010, **16**, 10234.

[17] Q. Zhang, C. Cobley, L. Au, M. McKiernan, A. Schwartz, L.-P. Wen, J. Chen, and Y. Xia. *Appl. Mater. Interfaces* 2009, **1**, 2044.

[18] Q. Zhang, W. Li, C. Moran, J. Zeng, J. Chen, L.-P. Wen, and Y. Xia. *J. Amer. Chem. Soc.* 2010, **132**, 11372.

[19] B. Wiley, Y. Sun, B. Mayers, and Y. Xia. *Chem. Eur. J.* 2005, **11**, 454.

[20] F. Zhou, Z.-Y. Li, Y. Liu, and Y. Xia. *J. Phys. Chem. C* 2008, **112**, 20233.

[21] E. Ringe, J. M. McMahon, K. Sohn, C. Cobley, Y. Xia, J. Huang, G. C. Schatz, L. D. Marks, and R. P. Van Duyne. *J. Phys. Chem. C* 2010, **114**, 12511.

[22] Q. Zhang, C. H. Moran, X. Xia, M. Rycenga, N. Li, and Y. Xia. *Langmuir* 2012, **28**, 9047.

[23] J. M. McLellan, Y. Xiong, M. Hu, and Y. Xia. *Chem. Phys. Lett.* 2006, **417**, 230.

[24] S. Y. Lee, L. Hung, G. S. Lang, J. E. Cornett, I. D. Mayergoyz, and O. Rabin. *ACS Nano* 2010, **4**, 5763.

[25] P. H. C. Camargo, M. Rycenga, L. Au, and Y. Xia, *Angew. Chem. Int. Ed.*, 2009, **48**, 2180-2184.

[26] G. A. T. Chansin, J. Hong, J. Dusting, A. J. deMello, T. Albrecht, and J. B. Edel, *Small*, 2011, **7**, 2736-2741.

[27] R. F. Egerton, P. Li, and M. Malac, *Micron*, 2004, **35**, 399-409.

[28] J. Li, M. Toth, V. Tileli, K. A. Dunn, C. J. Lobo, and B. L. Thil, *Appl. Phys. Lett.*, 2008, **93**, 023130.

[29] P. Roediger, H. D. Wanzenboeck, G. Hochleitner, and E. Bertagnolli, *J. Vac. Sci.*

Technol. B, 2009, **27**, 2711-2717.

[30] K. Rykaczewski, M. R. Henry, S.-K. Kim, A. G. Federov, D. Kulkarni, S. Singamaneni, and V. V. Tsukruk, *Nanotechnology*, 2010, **21**, 035202

[31] D. D. Kulkarni, K. Rykaczewski, S. Singamaneni, S. Kim, A. G. Fedorov, and V. V. Tsukruk, *ACS Appl. Mater. Interfaces*, 2011, **3**, 710-720.

[32] W. Ding, A. Dikin, X. Chen, R. D. Piner, R. S. Ruoff, E. Zussman, X. Wang, and X. Li, *J. Appl. Phys.*, 2005, **98**, 014905.

[33] K. L. Norrod and K. L. Rowlen, *Anal. Chem.*, 1998, **70**, 4218-4221.

[34] K. Itoh, I. Kudryashov, J. Yamagata, T. Nishizawa, M. Fujii, and N. Osaka, *J. Phys. Chem. B*, 2005, **109**, 271-276.

[35] H. Ishida, H. Fukuda, G. Katagiri, and A. Ishitani, *Appl. Spectros.*, 1986, **40**, 322-330.

[36] A. Kudelski and B. Pettinger, *Chem. Phys. Lett.*, 2000, **321**, 356-362.

[37] G. Sauer, G. Brehm, and S. Schneider, *J. Raman Spectrosc.*, 2004, **35**, 568-576.

[38] M. Rycenga, M. H. Kim, P. H. C. Camargo, C. Cobley, Z.-Y. Li, and Y. Xia, *J. Phys. Chem. A*, 2009, **113**, 3932-3939.

[39] J.-C. Merlin and J.-P. Cornard, *J. Chem. Educ.*, 2006, **9**, 1393.

[40] P. A. Waske, N. Meyerbröker, W. Eck, and M. Zharnikov, *J. Phys. Chem. C*, 2012, **116**, 13559-13568.

[41] W. Geyer, V. Stadler, W. Eck, M. Zharnikov, A. Gölzhäuser, and M. Grunze, *Appl. Phys. Lett.*, 1999, **75**, 2401-2403.

[42] A. S. P. Chang, A. Maiti, N. Ileri, M. Bora, C. C. Larson, J. A. Britten, and T. C. Bond, *Proc. SPIE*, 2012, **8366**, 83660S.

[43] C. M. Cobley, S. E. Skrabalak, D. J. Campbell, and Y. Xia, *Plasmonics*, 2009, **4**, 171-179.

CHAPTER 3: SERS AS A TOOL FOR MOLECULAR DETECTION

3.1 Introduction

Applications in nanomedicine frequently require that the surfaces of the nanoparticles are functionalized with some specific molecules. The type and purpose of this surface modification varies by application, as demonstrated in Figure 3.1. For example, linker molecules typically modify nanoparticle surfaces prior to attaching targeting moieties like antibodies or peptides.[1] There are also reactive molecules such as “smart” polymers that are sensitive to environmental changes such as pH or temperature and perform a controlled task such as the release of encapsulated drug.[2,3] Finally, coatings may be introduced to improve the biocompatibility and toxicity effects of the nanoparticles and mitigate uptake by macrophages in the reticuloendothelial system (RES).[4-6]

When inorganic nanoparticles are used, there is another reason why the surface must be modified. The synthesis of nanoparticles leaves a residue on the surface in the form of surfactants or capping agents used to control the nanoparticle growth and stability. This residue may interfere with the function of the nanoparticle, cause aggregation and instability *in vivo,* and in some cases, may even be toxic.[6,7]

3.2 Nanoparticle Surfaces and Capping Agents

Capping agents are macromolecules or ions such as PVP, bromide, or citrate used in nanoparticle synthesis to control its shape during growth by stabilizing certain crystal facets.[8-10] Stabilization results from the strong interactions between the capping agent and metal atoms of a particular crystal facet, thus controlling the relative growth rates of different types of facets. The strong interactions means the capping agents remain on the

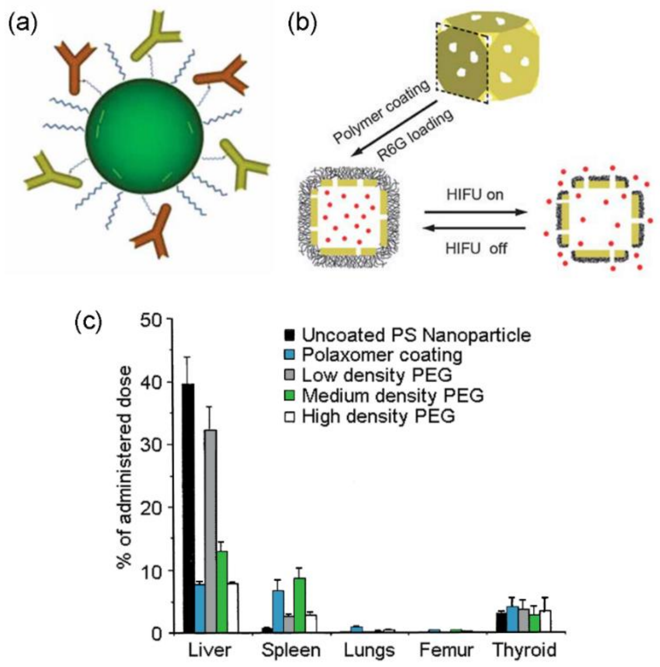

Figure 3.1. Different types of nanoparticle coatings used in nanomedicine. The surface of nanoparticles is most commonly modified with molecules which serve (a) to attach the targeting ligands, (b) for controlled release of drugs, and (c) to stabilize nanoparticles and control biodistribution.[1,2,5]

surface even after the nanoparticle products are washed.[7,11,12] Since some capping agents are toxic to cells, it is important to confirm that the capping agent is completely removed and replaced by the addition of a functional polymer layer before the nanoparticles can be used for *in vitro* or *in vivo* experiments.[4,7] For nontoxic capping agents such as PVP, confirmation of its complete removal is still necessary to enable quantification of the attached functional groups, such as antibodies. As a sensitive, surface-localized technique, SERS is uniquely suited to this task.

3.3 Types of Nanoparticle Coatings Needed in Medical Applications

The three basic functions of surface coatings needed in nanomedicine are linking, acting, and stabilizing, as shown in Figure 3.1. Nanoparticles designed for a particular application may utilize any combination of these three types of surface modification.

Linkers are important for all nanoparticle applications involving targeting. Polymers or other molecules with reactive end groups are often used to anchor antibodies, peptides, SiRNA, and other targeting moieties to the nanoparticle surface.[1,13-15] Active targeting can improve the tumor uptake of nanoparticles significantly, and functionalization by bioactive molecules is also a key step for the development of plasmonic-based biosensors.[16-18]

The active coating typically involves polymers which are sensitive to changes in the local environment. In biomedical applications, these typically involve changes in pH or temperature. At elevated temperatures caused by thermal ablation, a coating of temperature-sensitive polymers will shrink and become more hydrophobic, and thus may be used for controlled activities such as drug release.[2,19,20] For controlled release of drugs when taken up by cells, pH sensitive coatings which break down in the acidic environment of an endosome or lysosome are employed.[19,21] Other molecular coatings may have regions sensitive to protease breakdown to facilitate the activity *in vivo*.[22,23]

The stabilizers are likely needed for nearly all nanomedicine applications. The stabilizer layer improves biocompatibility by preventing nanoparticles from aggregation and improving blood circulation time. It also helps to reduce the uptake of the nanoparticles by the macrophages in the RES. Stabilizers typically come in the form of poly(ethylene glycol) (PEG),[5,6] but can also be more advanced systems for cloaking and targeting by coating the nanoparticles with cell membrane materials.[24]

Confirming the success of surface modification for plasmonic nanoparticles can be as simple as observing a shift in the LSPR as a result of a change in the dielectric constant of the environment surrounding the nanoparticles. However, in order to ensure complete removal of the capping agent and potentially toxic surfactants, a more quantitative approach like SERS is necessary.[25]

3.4 Kinetics of Ligand Exchange on the Surface of Silver Nanocubes

Thanks to the localized surface nature of SERS detection, this technique can be used to monitor changes on the surface of a nanoparticle during functionalization as the capping agent or surfactant is exchanged for the functional polymer layer. If either the capping agent or the functional group has strong SERS signals, the replacement reaction can be monitored by measuring changes in the SERS signal intensity over time. Understanding the kinetics of various surface modification reactions can also streamline future research experimentation and manufacturing processes.

3.4.1 Detection of Poly(vinyl pyrrolidone) by SERS

When synthesizing Ag nanocubes, like those shown in Figure 3.2(a), PVP is used as a capping agent. The cubic shape develops due to a stronger interaction between PVP, shown in the inset in Figure 3.2(b), and the {100} facets of silver, slowing down the growth of these facets relative to others.[10,11,26,27] This interaction is thought to occur between the Ag atoms and the carbonyl group located on the pyrrolidone ring.[28] Therefore, the SERS spectrum of PVP adsorbed on the Ag surface will exhibit strong enhancement for the C=O stretching vibration.[11,25] In the ordinary Raman spectrum of PVP shown in Figure 3.2(b), this peak appears at 1670 cm^{-1}. When bound to the surface of Ag nanoparticles, however, there is a discrepancy in the literature over the peak position of this carbonyl group. Some have shown that this peak was slightly shifted down to the range of 1605-1630 cm^{-1},[29] while others have identified this peak in the range of 1750-1769

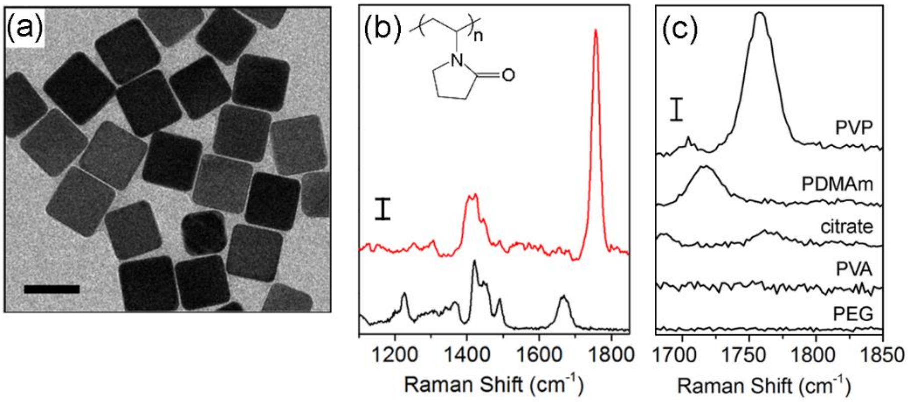

Figure 3.2. (A) TEM image of the 60-nm Ag nanocubes used for the solution-phase replacement reaction. Scale bar: 60 nm. (B) Ordinary Raman spectrum of solid PVP (black) and SERS spectrum of PVP adsorbed on the surface of the 60-nm Ag nanocubes suspended in an aqueous solution (red). The inset shows the chemical structure of PVP. The vertical scale bar represents 125 counts. The strongest SERS peak at 1760 cm^{-1} can be assigned to the C=O stretch. (C) SERS spectra in the carbonyl region of PVP from aqueous suspensions of Ag nanoparticles synthesized with PVP, PDMAm, citrate, PVA, and PEG, respectively, as capping agents. Scale bar: 1000 counts.[25] Reprinted with permission from J. Phys. Chem. C. Copyright 2012, American Chemical Society.

cm^{-1}.[30,31] In the SERS spectrum I obtained from an aqueous suspension of Ag nanocubes, there was a strong peak at 1760 cm^{-1}, see Figure 3.2(b), which most likely belongs to the carbonyl groups in PVP.[30,31]

To confirm that the strong peak at 1760 cm^{-1} is indeed associated with the C=O groups in PVP, Ag nanoparticles were synthesized in water by reducing $AgNO_3$ in the presence of PVP, citrate, poly(N,N-dimethyl acrylamide) (PDMAm), poly(vinyl alcohol) (PVA), and PEG, respectively. Figure 3.2(c) shows the SERS spectra recorded from the as-prepared, aqueous suspensions of these different samples, where the peak at 1760 cm^{-1} was only present for the nanoparticles synthesized in the presence of PVP as a stabilizer. The peak at 1710 cm^{-1} observed for nanoparticles synthesized in the presence of PDMAm is representative of a carboxylic acid group after hydrolysis of the amide.[32] The other SERS

Table 3.1. Assignments of peaks for the SERS and ordinary Raman spectra.

Raman shift[a]	SERS band assignment[b]	Raman band assignment[c]
1225	-	CH_2 twisting vibration
1300	CH_2 wagging, C-N stretching[c]	CH_2 wagging
1425	CH_2 vibration	CH_2 scissor vibration
1450	CH_2 scissor vibration	CH_2 scissor vibration
1490	C'-N stretching[c]	C'-N stretching
1670	-	C=O, C'-N stretch (amide I)
1760	C=O stretch	-

[a] Wavenumber in cm^{-1}. [b] Ref 20. [c] Refs 5, 27, C'=carbonyl carbon.

Reprinted with permission from J. Phys. Chem. C. Copyright 2012, American Chemical Society.

peaks from the nanocubes could also be attributed to PVP, as outlined in Table 3.1.

Compared to the ordinary Raman spectrum taken from a pure, solid PVP, shown in Figure 3.2(b), many of the CH_2 vibrations in the range 1300-1450 cm^{-1} are in agreement, as well as the N-C stretching for the carbonyl carbon.[30] The carbonyl band at 1760 cm^{-1} is the strongest, and also the most important because it corresponds to a moiety that directly interacts with the surface of Ag nanocubes.[28]

In addition to those carbonyl groups directly binding to the Ag surface, other carbonyl groups in the PVP layer may also contribute to the observed SERS peak if they are sufficiently close to the metal surface. The orientations of these carbonyl groups with respect to the Ag surface may affect the intensity of the SERS peak.[29] This is supported by the observation that the intensity of the carbonyl peak decreased when measured from a dry film of Ag nanocubes, as shown in Figure 3.3(a, c, e, g). As the layer of PVP was dried, it is likely that the polymer collapsed due to the removal of hydrogen bonding with water, causing the carbonyl groups to lay parallel to the Ag surface. When the surface was

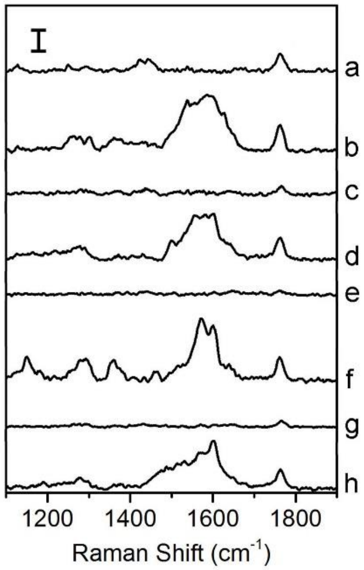

Figure 3.3. The carbonyl SERS peak intensity fluctuated depending on if the Ag nanocubes on a substrate were dried (a, c, e, g) or wet with water (b, d, f, h). The spectra were collected from the same approximate area of a film of 60-nm Ag nanocubes through 4 cycles of drying and wetting. Scale bar: 250 counts. [25] Reprinted with permission from J. Phys. Chem. C. Copyright 2012, American Chemical Society.

re-wetted, the polymer was hydrated again and the carbonyl groups returned to a perpendicular orientation with the surface,[29] resulting in an increase for the SERS signal, shown in Figure 3.3(b, d, f, h). As Figure 3.3 demonstrates, this phenomenon could be observed repeatedly and reproducibly when SERS spectra were taken after 4 cycles of wetting and drying of the same film of Ag nanocubes.

3.4.2 Replacement of the PVP on Ag Nanocubes

Replacement of PVP by other functional groups will actively disrupt the carbonyl interaction with the surface, so I expected the intensity of SERS signals from PVP would be dramatically diminished over the course of this replacement. Cysteamine and methoxy-terminated poly(ethylene glycol) thiol (mPEG-SH) were used to replace the PVP in two separate experiments because they formed hydrophilic monolayers on Ag nanocubes so that SERS measurements could be conducted in aqueous solutions. In addition, neither of these two thiols contained a carbonyl group, so only the carbonyl groups in PVP contributed to the SERS peak at 1760 cm^{-1}. The replacement of PVP was carried out with Ag nanocubes of 60 nm in edge length, which yielded stronger signals at 1760 cm^{-1} compared to smaller nanocubes, providing greater sensitivity for monitoring the intensity change over time. Figure 3.4 shows that the intensity of the carbonyl peak at 1760 cm^{-1} decreased with time during replacement. Since mPEG-SH is much larger than cysteamine, the rate of replacement was slower as expected and shown in Figure 3.5. This dependence on ligand size can be attributed to the difference in rate of diffusion for the two types of

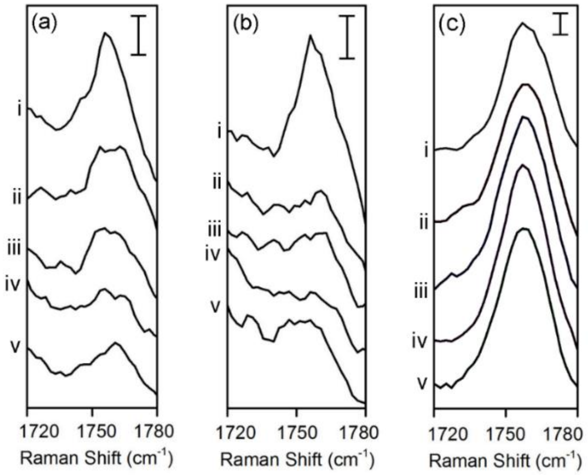

Figure 3.4. SERS spectra of Ag nanocubes in aqueous suspensions showing the replacement of PVP with (a) cysteamine and (b) mPEG-SH over time. The intensity of the C=O stretching peak at 1760 cm^{-1} decreased over time as PVP was removed from the surface in favor of a stronger Ag-thiolate bond. The SERS spectra were acquired: (i) before adding the thiol, and (ii) 5 min, (iii) 10 min, (iv) 30 min and (v) 60 min after incubation with 1 μM solution of cysteamine (ethanolic) or mPEG-SH (aqueous), respectively. To confirm replacement by thiols, (c) a control sample of Ag nanocubes in water was monitored over the same time-frame. There was no change in the amplitude of the C=O stretching peak in this sample, indicating thiol replacement was the cause behind the reduction in (a) and (b). The spectra are shifted vertically for clarity, and the scale bars represent 50 counts.[25] Reprinted with permission from J. Phys. Chem. C. Copyright 2012, American Chemical Society.

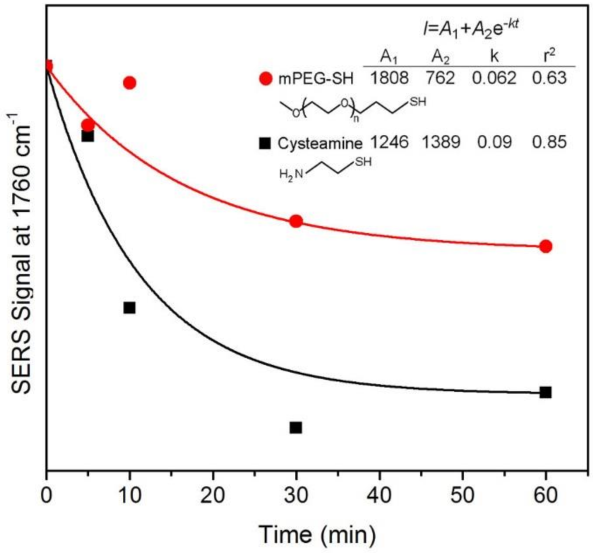

Figure 3.5. The relationship between the SERS peak intensity at 1760 cm^{-1} and the replacement time for cysteamine (black) and mPEG-SH (red) is modeled as the exponential decay of SERS signal intensity from PVP as the thiol molecules form a monolayer on the nanocrystal surface. The fitting curves were obtained based on a linear regression to a Langmuir desorption model (Equation 3.1). When the mPEG-SH data-point at t = 10 min was omitted from the fitting analysis, the fit was excellent, with an r^2 of 0.99. Calculations of peak areas were made on the peak centered at 1760 cm^{-1} alone. The values were normalized after fitting for comparison. The fitting parameters and chemical structures of mPEG-SH and cysteamine are inset. The value of n for the mPEG-SH used was approximately 111.[25] Reprinted with permission from J. Phys. Chem. C. Copyright 2012, American Chemical Society.

thiols. The change in SERS intensity over time resembled the Langmuir adsorption curve,[33] which describes the formation of a monolayer on a surface. Typically the Langmuir curve is used to model an increase in signal amplitude over time as the monolayer formation is monitored.[33,34] However, I tracked desorption of PVP in this study, or a decrease in signal over time,[35] due to the formation of a monolayer by a different molecule. I therefore modeled the dependence of SERS signals on time using the following format of the Langmuir adsorption curve:

$$I=A_1+A_2e^{-kt} \qquad (3.1)$$

where A_1 represents the initial signal intensity of the peak before functionalization and t is time. Assuming that the dissociation of thiols from the surface is negligible, k and A_2 are the fitting parameters for a linear regression of the data points, where k represents the binding constant of the thiol and A_2 represents the saturation surface coverage of the thiol, with respect to thiol concentration. Figure 3.5 shows that the decrease of SERS signals from PVP over time indeed follows this relationship, and the fit to the exponential decay curve was reasonably good. The SERS peak of PVP on a control sample of Ag nanocubes where no ligand was added did not show any change with time, as shown in Figure 3.4(c).

Due to the covalent nature of the Ag-thiolate bond, replacement of PVP by thiol molecules tends to occur rapidly and thoroughly.[34,36,37] I therefore used a very low

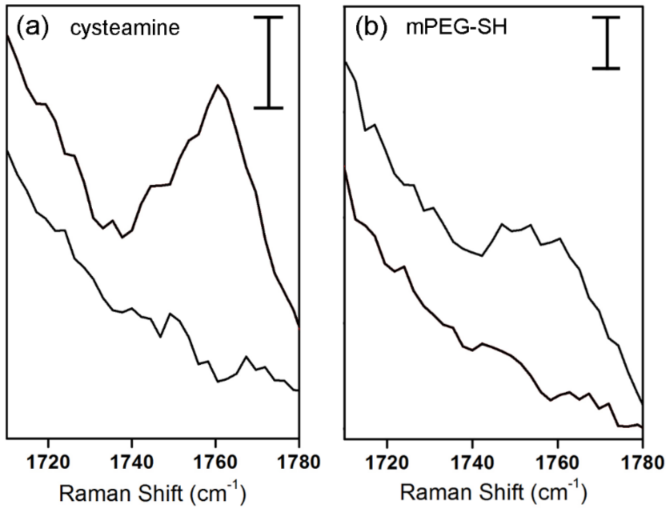

Figure 3.6. SERS spectra showing the complete removal of PVP from the surface of 60-nm Ag cubes. After incubation with 1 μM solutions of (a) cysteamine and (b) mPEG-SH for 60 min (top trace in each panel), PVP was greatly reduced, but not completely removed. The bottom trace in each panel shows the spectrum recorded after thorough washing with water and incubation again for 30 min with fresh 1 μM solutions of cysteamine and mPEG-SH, respectively, completely removing the remaining PVP. The spectra were shifted vertically for clarity, and both scale bars represent 15 counts.[25] Reprinted with permission from J. Phys. Chem. C. Copyright 2012, American Chemical Society.

thiol concentration (1 μM) in order to slow down the reaction so that the change in SERS intensity could be detected. However, at this low concentration of ligand, the equilibrium between PVP bound to the surface and PVP free in solution was shifted toward a surface bound state,[38] and thus a small fraction of PVP remained on the surface. By exposing the surface of Ag nanocubes partially covered by thiol to a fresh solution of thiol, the remaining PVP could be completely removed from the surface (Figure 3.6), indicating that the entire surface was now covered by a monolayer of the thiol ligand. For SERS applications, especially in the detection of molecules on a single particle, the equilibrium can be reached in one replacement step by using the thiol at a higher concentration (Figure 3.7). The replacement of PVP by cysteamine or mPEG-SH was also confirmed using absorption spectroscopy, which shows a blue shift in the LSPR peak of the Ag nanocubes after the replacement (Figure 3.8).

The replacement of PVP by thiol molecules can also be observed on the single nanoparticle level. The SERS spectrum of PVP on single Ag nanocubes was extremely weak. In addition to the fact that single particle studies are conducted in the dry state, a single nanocube does not provide a large enough number of PVP molecules or carbonyl groups, which is not a strongly Raman active group. I therefore monitored the signal increase of 1,4-BDT, a strongly Raman active molecule, which also increased over time according to the conventional Langmuir adsorption model (Figure 3.9). This new result confirms the observations made in solution-phase measurements, and results from other studies that used benzenethiol molecules.[34]

Previous SERS studies of PVP have mostly focused on characterizing its spectrum,[28,39,32] but these papers suggest a strong dependence on the properties of

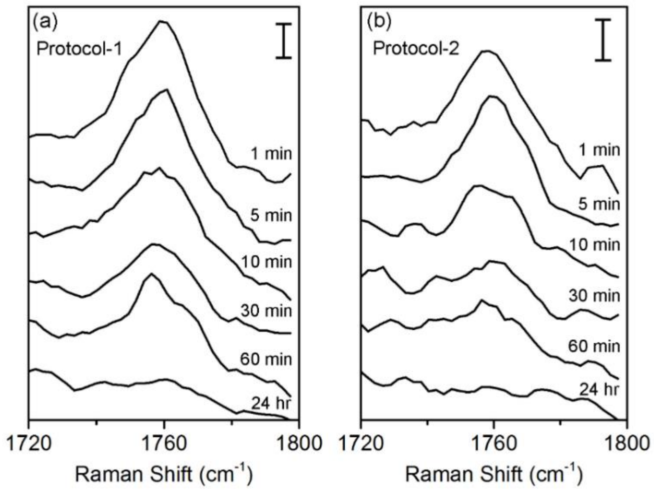

Figure 3.7. Comparison of two protocols for measuring the decrease in SERS peak intensity for PVP during replacement with mPEG-SH. (a) Protocol 1: Aliquots (20 μL) from a stock solution of Ag nanocubes and mPEG-SH were removed at different time points and washed. Each sample was re-suspended with 50 μL water to collect the SERS spectrum. (b) Protocol 2: A single stock solution of Ag nanocubes and mPEG-SH was used for each of the SERS measurements at different time points. The vertical scale bars are 100 counts.[25] Reprinted with permission from J. Phys. Chem. C. Copyright 2012, American Chemical Society.

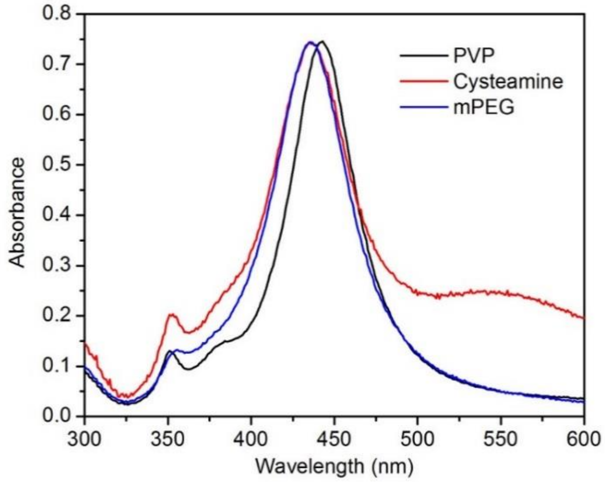

Figure 3.8. UV-vis absorption spectra of the 60-nm Ag nanocubes before (black) and after functionalization with each of the two thiols, cysteamine (red) and mPEG-SH (blue). The major resonance peak for Ag nanocubes functionalized with thiols exhibited a slight blue shift as a result of the change in environment compared to the PVP coating. There seemed to be some aggregation for the Ag nanocubes functionalized with cysteamine, as indicated by the appearance of a shoulder around 550 nm.[25] Reprinted with permission from J. Phys. Chem. C. Copyright 2012, American Chemical Society.

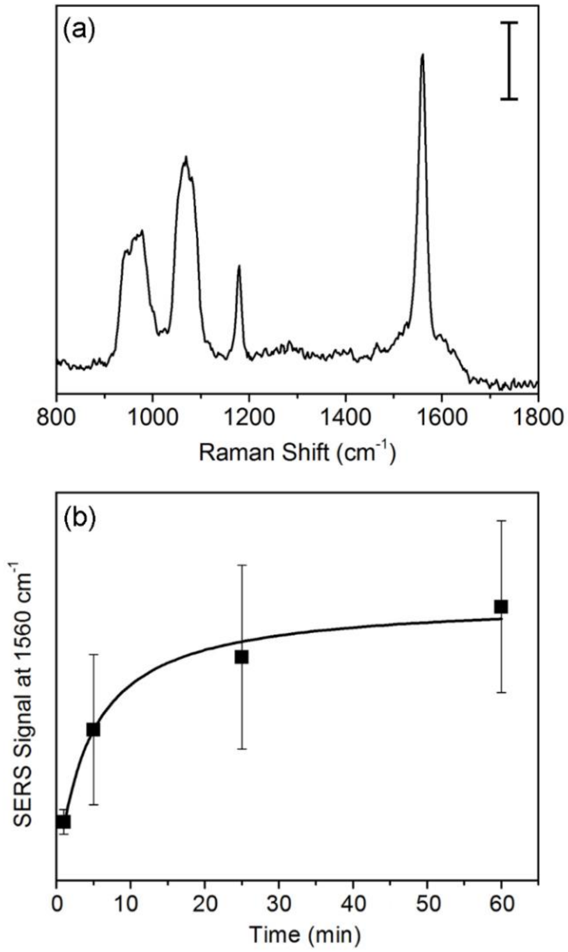

Figure 3.9. (a) Representative SERS spectrum of 1,4-BDT on a single Ag nanocube deposited on a Si substrate after 60 min of functionalization. The strongest peak at 1560 cm^{-1} corresponds to the phenyl ring stretching mode. Other bands representative of 1,4-BDT are the CH bending at 1181 cm^{-1} and interactions between the Ag surface and the benzene ring from 1046-1090 cm^{-1}. The broad band from 920-1000 cm^{-1} came from the Si substrate. The vertical scale bar represents 100 counts. The Ag nanocubes were 110 ± 5 nm in edge length. (b) A plot of the intensity of SERS peak at 1560 cm^{-1} as a function of the reaction time. The increase in SERS signal intensity was fitted to a Langmuir adsorption curve ($r^2 = 0.98$).[25] Reprinted with permission from J. Phys. Chem. C. Copyright 2012, American Chemical Society.

metal substrates, including size, shape, and type of metal as well as PVP concentration. PVP by itself is therefore not a reliable Raman reporter molecule. Most SERS studies using metal colloids as substrates neglected the presence of capping molecules by focusing on the adsorption of Raman reporter molecules and the value of enhancement factors.[11,30,40,41] This study bridges the gap between these types of studies by demonstrating the utility of SERS measurements of capping agents such as PVP for ensuring the complete functionalization of the nanoparticle substrate, and confirming that it can be effectively replaced by more reliable Raman reporters for various SERS applications.

3.5 Summary

SERS has the potential to serve as a valuable research tool in nanomedicine. I demonstrated that SERS can be used to monitor changes in the surface chemistry of nanoparticles. Since surface chemistry plays a critical role in nanomedicine, the information provided by SERS would allow researchers to develop nanomedicine applications quickly and efficiently, and with greater confidence that the surface chemistry is appropriate and matches their hypotheses. SERS was used here to monitor the replacement of residual capping agents by functional layers of polymers on the surfaces of Ag nanocubes. This reaction occurs in agreement with the Langmuir adsorption model for monolayer formation. Accordingly, reaction times and rates can be accurately predicted and modeled for a variety of surface ligands.

3.6 Experimental Details

3.6.1 Synthesis of Silver Nanoparticles Used as Control Samples

The synthesis of Ag nanocubes was the same as what was described in Chapter 2, Section 6.1. The spherical Ag nanoparticles were synthesized to compare the SERS spectra of capping agents different from what was used for the Ag nanocubes. In a typical synthesis, 10 mL of an aqueous solution (2 mM) of sodium borohydride ($NaBH_4$, Sigma Aldrich) was stirred vigorously on ice while 3.33 mL of aqueous $AgNO_3$ solution (5 mM) was added. To stabilize the growth of the Ag nanoparticles, 1.67 mL of a 1% solution of a capping agent was added immediately after the addition of $AgNO_3$. The polymers used were PVA (Sigma Aldrich), PDMAm (Scientific Polymer Products), PEG (Sigma Aldrich), and PVP. In addition, citrate-stabilized Ag nanoparticles were synthesized by adding 1 mL of a 1% aqueous solution of sodium citrate (Sigma Aldrich) to 50 mL of boiling $AgNO_3$ (1 mM). All samples were washed three times with DI water. SEM images showed polycrystalline Ag nanoparticles with broad size distributions other than the samples of Ag nanocubes were produced.

3.6.2 Functionalization of Silver Nanocubes

Silver nanocubes were functionalized with several different ligands over the course of this study. To monitor the replacement of PVP, Ag nanocubes of 60 nm in edge length were functionalized with cysteamine (Aldrich) or mPEG-SH (MW ≈ 5,000, Laysan Bio, Inc.). Equal volumes of as-prepared Ag nanocubes dispersed in DI water were mixed with an aqueous mPEG-SH solution so there was a final thiol concentration of 1 μM and a final Ag nanocube concentration of approximately 5×10^9 particles/mL in a total volume of 140 μL. After 5, 10, 30 and 60 min, 20 μL aliquots were removed from the vial, injected into

1.5 ml centrifuge tubes, and immediately diluted with DI water. The cubes were washed twice in water with centrifugation to remove any unbound mPEG-SH, and were then re-suspended in 50 μL of DI water. A SERS spectrum was taken from each aqueous suspension in order to monitor the decrease in PVP signal over time. To confirm that the centrifugation steps did not affect the overall concentration of Ag nanocubes and resulting SERS signal intensity, I compared this method to a second protocol for surface functionalization. In protocol 2, the Raman data was collected at different time points from a single suspension of Ag nanocubes mixed with mPEG-SH (see Figures 3.7 and 3.10). There were no measurable differences in the SERS signal intensity changes over time between the two protocols (Figure 3.7) and UV-vis absorbance confirmed that the

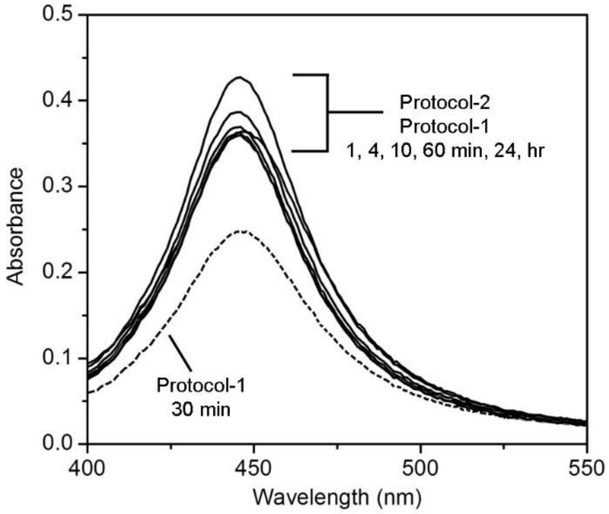

Figure 3.10. UV-vis absorption spectra of the Ag nanocubes involved in the comparison of two different PVP replacement protocols shown in Figure 3.7. Only one sample from protocol 1 (taken at 30 min) experienced a significant loss of Ag nanocubes due to washing, as indicated by the dashed curve. Protocol 2 only needed one UV-vis measurement taken at the end of the experiment. The similarity in absorbance between protocols 1 and 2 demonstrates that the washing steps in protocol 1 did not significantly affect the concentration of Ag nanocubes, and therefore should not affect the SERS intensities of PVP.[25] Reprinted with permission from J. Phys. Chem. C. Copyright 2012, American Chemical Society.

concentration between samples was not affected by centrifugation (Figure 3.10).

For functionalization with cysteamine, 70 μL as-prepared Ag nanocubes were centrifuged and re-suspended in an equal volume of ethanol before mixing with 70 μL of an ethanolic solution of cysteamine, resulting in a final thiol concentration of 1 μM and a final volume of 140 μL. After 5, 10, 30 and 60 min, 20 μL aliquots were removed from the vial, injected into 1.5 ml centrifuge tubes, and immediately diluted with ethanol. The cubes were washed once in ethanol and once in water with centrifugation to remove any unbound cysteamine, and were then re-suspended in 50 μL of DI water.

Functionalization with a 1 mM solution of 1,4-benzenedithiol (1,4-BDT, 98%, Alfa Aesar) in ethanol was performed for single-particle SERS studies. Silver nanocubes of 110 nm in edge length were dispersed onto a Si substrate and the entire chip was immersed in the ethanolic 1,4-BDT solution. After 1, 5, 25, and 60 min cumulative exposure time, the chip was removed from the solution and washed with copious amounts of ethanol and DI water in preparation for SERS measurements. After SERS spectra collection, the substrate was imaged using SEM to confirm that only individual Ag nanocubes had been selected. I chose 110-nm Ag nanocubes because they are more easily located on the substrate using dark-field illumination, and they also provided stronger SERS enhancement than the 60-nm cubes.

3.6.3 Surface-Enhanced Raman Spectroscopy (SERS)

The SERS spectra were recorded using the same Raman spectrometer set-up described in Chapter 2, section 6.3. The excitation wavelength used was 514 nm. Data was collected from the solution phase with a laser power of 5 mW and a collection time of 60 sec for all samples. Sample cells were made by attaching a microcentrifuge tube cap, which holds 50 μL of liquid sample, to a glass slide. A thin glass cover slip (0.17 mm) was placed on top of the sample's meniscus to prevent evaporation and to act as a reference point from which the focal plane was lowered 200 μm into the sample. For single particle studies, individual Ag nanocubes were located on the substrate using dark-field illumination. Spectra were collected at 10% laser power for 25 sec acquisition time from each Ag nanocube. The spectra from the Ag nanocube film dried on a Si substrate were also collected at 10% laser power, but for 45 sec acquisition time.

Probing the orientation of the carbonyl group was performed by first placing 1 μL drop of 60-nm Ag nanocubes on a Si substrate. The drop was dried for 15 min in a 75 ºC oven to form a Ag nanocube film. After taking a SERS spectrum from the film, a 1 μL drop of water was placed on top. Another SERS spectrum was collected, and the film was dried again in the oven. This cycle was repeated 4 times. The Si substrate had been marked prior to forming the Ag nanocube film so that the same relative area could be probed for each iteration.

Data processing was performed using OriginPro v. 8.1, Student edition (OriginLab, Corp., Northampton, MA). All data was baseline corrected by subtracting the minimum from the data. Data taken from Si substrates were normalized to the peak of Si at 920-1000 cm^{-1}. If smoothing was necessary, an adjacent-averaged smoothing algorithm was applied with a window size of 2 or 4 data points. Fitting of the change in peak area over time was performed with nonlinear regression to a Langmuir adsorption model using Matlab v. 7.10 (Mathworks Inc., Natick, MA).

3.7 References

[1] S. Kumar, J. Aaron, and K. Sokolov. *Nat. Protoc.* 2008, **3**, 314.

[2] W. Li, X. Cai, C. Kim, G. Sun, Y. Zhang, R. Deng, M. Yang, J. Chen, S. Achilefu, L. V. Wang, and Y. Xia. *Nanoscale* 2011, **3**, 1724.

[3] M.-Q. Zhu, L.-Q. Wang, G. J. Exarhos, and A. D. Q. Li. *J. Amer. Chem. Soc.* 2004, **126**, 2656.

[4] N. Lewinski, V. Colvin, and R. Drezek. *Small* 2008, **4**, 26.

[5] S. E. Dunn, A. Brindley, S. S. Davis, M. C. Davies, and L. Illum. *Pharma. Res.* 1994, **11**, 1016.

[6] S. D. Perrault, C. Walkey, T. Jennings, H. C. Fischer, and W. C. W. Chan. *Nano Lett.* 2009, **9**, 1909.

[7] C. Grabinski, N. Schaeublin, A. Wijaya, H. D'Couto, S. H. Baxamusa, K. Hamad-Schifferli, and S. M. Hussain. *ACS Nano* 2011, **5**, 2870.

[8] Y. Sun and Y. Xia. *Science* 2002, **298**, 2176.

[9] J. Zeng, Y. Zheng, M. Rycenga, J. Tao, Z.-Y. Li, Q. Zhang, Y. Zhu, and Y. Xia. *J. Amer. Chem. Soc.* 2010, **132**, 8552.

[10] Y. Xia, Y. Xiong, B. Lim, and S. E. Skrabalak. *Angew. Chem. Int. Ed.* 2009, **48**, 60.

[11] Q. Zhang, W. Li, C. Moran, J. Zeng, J. Chen, L.-P. Wen, and Y. Xia. *J. Am. Chem. Soc.* 2010, **132**, 11372.

[12] Q. Zhang, C. H. Moran, X. Xia, M. Rycenga, N. Li, and Y. Xia. *Langmuir* 2012, **28**, 9047.

[13] C. Loo, A. Lowery, N. Halas, J. West, and R. Drezek. *Nano Lett.* 2005, **5**, 709.

[14] L. Au, Q. Zhang, C. M. Cobley, M. Gidding, A. G. Schwartz, J. Chen, and Y. Xia. *ACS Nano* 2010, **4**, 35.

[15] L. Wang, *et al*. *Nano Lett*. 2011, **11**, 772.

[16] R. Bardhan, S. Lal, A. Joshi, and N. J. Halas. *Acc. Chem. Res.* 2011, **44**, 936.

[17] D. S. Grubisha, R. J. Lipert, H.-Y. Park, J. Driskell, and M. D. Porter. *Anal. Chem.* 2003, **75**, 5936.

[18] J. A. Anker, W. P. Hall, O. Lyandres, N. C. Shah, J. Zhao, and R. P. van Duyne. *Nat. Mater.* 2008, **7**, 442.

[19] C. de las Heras Alarcón, S. Pennadam, and C. Alexander. *Chem. Soc. Rev.* 2005, **34**, 276.

[20] M. S. Yavuz, Y. Cheng, J. Chen, C. M. Cobley, Q. Zhang, M. Rycenga, J. Xie, C.

Kim, K. H. Song, A. G. Schwartz, L. V. Wang, and Y. Xia. *Nat. Mater.* 2009, **8**, 935.

[21] Z. Poon, D. Chang, X. Zhao, and P. T. Hammond. *ACS Nano* 2011, **5**, 4284.

[22] C. Wong, T. Stylianopoulos, J. Cui, J. Martin, V. P. Chauhan, W. Jiang, Z. Popovic, R. K. Jain, M. G. Bawendi, and D. Fukumura. *Proc. Natl. Acad. Sci.* 2011, **108**, 2426.

[23] E. S. Olson, T. Jiang, T. A. Aguilera, Q. T. Nguyen, L. G. Ellies, M. Scadeng, and R. Y. Tsien. *Proc. Natl. Acad. Sci.* 2010, **107**, 4311.

[24] C.-M. J. Hu, L. Zhang, S. Aryal, C. Cheung, R. H. Fang, and L. Zhang. *Proc. Natl. Acad. Sci.* 2011, **108**, 10980.

[25] C. H. Moran, M. Rycenga, Q. Zhang, and Y. Xia. *J. Phys. Chem. C* 2011, **115**, 21852.

[26] S. E. Skrabalak, L. Au, X. Li, and Y. Xia. *Nat. Protoc.* 2007, **2**, 2182.

[27] Y. Sun, B. Mayers, T. Herricks, and Y. Xia. *Nano Lett.* 2003, **3**, 955.

[28] Y. Borodko, S. Humphrey, T. D. Tilley, H. Frei, and G. A. Somorjai. *J. Phys. Chem. C.* 2007, **111**, 6288.

[29] Y. Gao, L. Song, P. Jiang, L. F. Liu, X. Q. Yan, Z. P. Zhou, D. F. Liu, J. X. Wang, H. J. Yuan, Z. X. Zhang, X. W. Zhao, X. Y. Dou, W. Y. Zhou, G. Wang, S. S. Xie, H. Y. Chen, and J. Q. Li. *J. Cryst. Growth.* 2005, **276**, 606.

[30] M. A. Mahmoud, C. E. Tabor, and El-Sayed, M. A. *J. Phys. Chem. C.* 2009, **113**, 5493.

[31] Y. Gao, P. Jiang, D. F. Liu, H. J. Yuan, X. Q. Yan, Z. P. Zhou, J. X. Wang, L. Song, L. F. Liu, W. Y. Zhou, G. Wang, C. Y. Wang, S. S. Xie, J. M. Zhang, and D. Y. Shen. *J. Phys. Chem. B.* 2004, **108**, 12877.

[32] S. J. Lee, G. Park, D. Seo, D. Ka, S. Y. Kim, I. S. Chung, and H. Song. *Chem. Eur. J.* 2011, **17**, 8466.

[33] J. M. McLellan, Y. Xiong, M. Hu, and Y. Xia. *Chem. Phys. Lett.* 2006, **417**, 230.

[34] S. Mahajan, R. M. Cole, J. D. Speed, S. H. Pelfrey, A. E. Russell, P. N. Bartlett, S. M. Barnett, and J. J. Baumberg. *J. Phys. Chem. C.* 2010, **114**, 7242.

[35] P. Hildebrandt and M. Stockburger. *J. Phys. Chem.* 1984, **88**, 5935.

[36] J. C. Love, L. A. Estroff, J. K. Kriebel, R. G. Nuzzo, and G. M. Whitesides. *Chem. Rev.* 2005, **105**, 1103.

[37] C. E. Taylor, S. D. Garvey, and J. E. Pemberton. *Anal. Chem.* 1996, **68**, 2401.

[38] D. P. McDermott. *J. Phys. Chem*. 1986, **90**, 2569.

[39] Y. Borodko, S. E. Habas, M. Koebel, P. Yang, H. Frei, and G. A. Somorjai. *J. Phys. Chem. B*. 2006, **110**, 23052.

[40] M. Rycenga, M. H. Kim. P. H. C. Camargo, C. Cobley, Z.-Y. Li, and Y. Xia. *J. Phys. Chem. A.* 2009, **113**, 3932.

[41] M. Rycenga, P. H. C. Camargo, W. Li, C. H. Moran, and Y. Xia. *J. Phys. Chem. Lett.* 2010, **1**, 696.

CHAPTER 4. SERS IMAGING AND MULTIPLEXING

4.1 Introduction

SERS recently emerged as an attractive imaging modality owing to its multiplexing and fingerprinting capabilities, high sensitivity, and real-time data feedback.[1-4] Nanoparticles functionalized with Raman reporters have been used to construct images for a variety of medical applications. SERS can image small areas like a single cell or a histology sample, or even larger areas like a tumor.[1,5-11] Essentially, SERS imaging takes advantage of the rich chemical information contained in a Raman spectrum to generate images of nanoparticle distributions. Notably, the Raman spectrum of a molecule is like a human fingerprint – each type of molecule has a unique pattern. Therefore, by simply changing the molecules attached to the nanoparticle's surface, many distinctive SERS probes can be easily fabricated.[3,4] Moreover, since SERS bands are much narrower compared with fluorescent peaks, multiplexing of multiple probes, data analysis, and image reconstruction is easier and more accurate.[1,3,4,9-11]

The narrow bands and unique nature of signals generated from different molecules allow for two or more different probes to be imaged simultaneously. This multiplexing capability is very useful in biomedical applications. Only a single excitation source is needed (unlike fluorescent molecules) to generate SERS from an array of different probe molecules, making it more efficient than current multiplexed imaging modalities. Due to the multimodal properties of metal nanoparticles, SERS imaging can also be combined with other therapeutic and diagnostic applications.[7,8] For these reasons, SERS is an attractive imaging technique that may become a useful tool, albeit for niche applications.

4.2 SERS Imaging Parameters

Despite the merits discussed above, the basic imaging parameters of SERS are rarely quantified. For example, the penetration depth of SERS is more or less limited when imaging biological samples due to the scattering and absorption by tissues, and thus deserves thorough investigation. In this chapter, the SERS images are closely compared with the corresponding physical objects – Ag nanocubes with a specific size, as well as well-defined separation and aggregation state. This work also represents the first study to characterize several important parameters of a SERS imaging system, including the blur and spatial resolution.[12]

4.2.1 Blur and Spatial Resolution

To determine the spatial resolution of the Raman system, the blur value (B_v) associated with a SERS image has to be characterized first. Blur takes into account the fact that an image is a visual representation of a specific physical object.[13] Ideally, a small point within the object would be represented by a congruent point within the image. In reality, the image of each point in the object is blurred in the image, and can be modelled by the point spread function (PSF). The degree of blurring is quantified by B_v, the dimension of the image of a very small point object. Figure 4.1 shows the SEM image of a single nanocube with an edge length of 100 nm, as well as the Rayleigh scattering image and the SERS image of the same nanocube. The nanocube is small enough to be used as a point object from which B_v can be determined from the images. Values of 1.2 μm and 0.5 μm were determined for the B_v of Rayleigh scattering and SERS images, respectively. In contrast, the typical blur values are 150 μm for mammography and 500 μm for photoacoustic tomography.[13,14] Figure 4.1(d) shows a plot of the lateral PSF as a

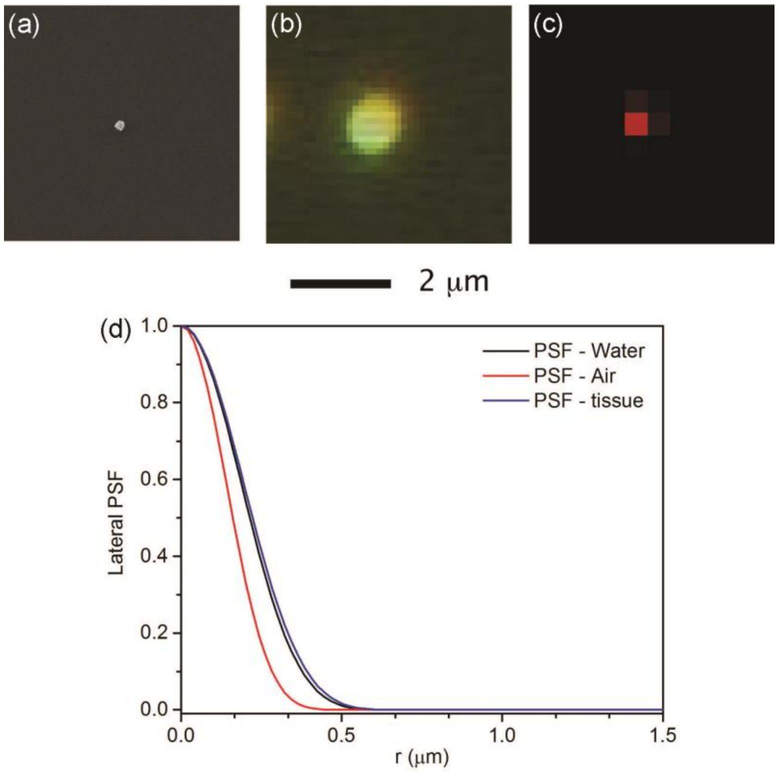

Figure 4.1. The blur value (B_v) of the SERS imaging system was determined by measuring the diameter of the image of an individual Ag nanocube used as a point object. (a) SEM image of a Ag nanocube with an edge length of 100 nm that had been functionalized with 1,4-BDT. (b) A dark-field image from the Rayleigh scattering of the same nanocube in (a). (c) SERS image of the same nanocube in (a). B_v of 1.2 and 0.5 μm were measured for Rayleigh scattering and SERS imaging, respectively. (d) The measured blur values were compared to the calculated lateral PSF of the confocal Raman imaging system as a function of the radial distance from the object point. The FWHM in air was 0.32 μm. The PSF of the system in water and tissue were also calculated, and the B_v was found to increase slightly in these media to 0.42 μm and 0.44 μm respectively. $\lambda_{ex} = 785$ nm, $t = 2$ s, $P = 3.1$ mW.[12] Printed with permission from IOP Publishing.

function of the radial distance from the point object for the Raman imaging system. For imaging in air, as was the case in Figure 4.1(a-c), the measured B_v correlates to the calculated full-width half-maximum (FWHM) of the PSF, which was 0.32 μm. This value is slightly better than the approximated B_v for SERS images taken in tissue and water, which were 0.44 and 0.42 μm, respectively.

Spatial resolution is closely related to blur, and it describes the ability of an imaging system to distinguish objects that are close to each other. The ability of the Raman system to resolve individual nanoparticles that were closely spaced was determined to obtain the spatial resolution of the system. The spatial resolution of a particular imaging system can be inferred by the degree of blur, and is typically defined as the FWHM of the PSF.[13,15] From the above measurements of blur for a single nanocube, the resolution was expected to be about 0.5 μm. To verify this, a linear array of nanocubes with different distances from one to another was formed on a Si substrate. Drop-casting a dilute suspension of nanocubes so that the outer edge of the meniscus slowly dried could yield such a linear array of nanocubes. Figure 4.2(a) shows the SEM image of an array of five nanocubes and Figure 4.2(b) shows the Rayleigh scattering image from the same array. The red line in Figure 4.2(b) shows the path of the Raman microprobe acquisition, and the peak intensity of the 1562 cm^{-1} band from 1,4-BDT was plotted along this line in Figure 4.2(c). This graph shows that nanocubes with more than 2 μm separation from each other can easily be resolved in the SERS image with the naked eye. However, the resolution could be more precisely calculated by determining the area between the peaks, which has a correlation with the separation between the nanoparticles. As the area between the peaks (P_a) approached zero, the separation between the nanoparticles approached 1.1 μm, which

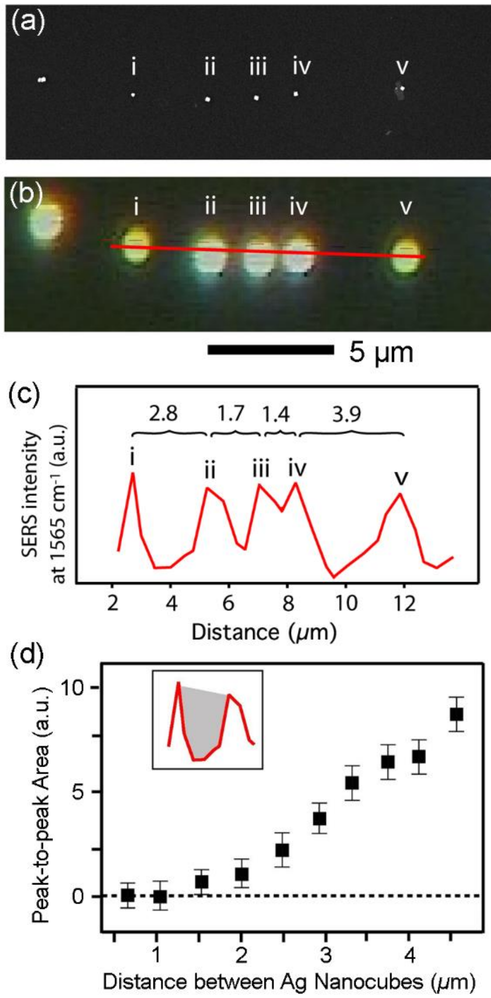

Figure 4.2. (a) SEM image of Ag nanocubes (edge length: 100 nm, functionalized with 1,4-BDT) on a Si substrate and (b) the corresponding dark-field image. The red line represents the path of the Raman acquisition that included the five nanocubes labeled in (a). Data was acquired over this red line with a step size of 0.2 μm. The scale bar is 5 μm. (c) A plot of the SERS intensity at 1562 cm^{-1} along the red line shown in (b), which clearly resolves the nanocubes. The distance between (i) and (ii) was 2.8 μm; (ii) and (iii) was 1.7 μm; (iii) and (iv) was 1.4 μm; and (iv) and (v) was 3.9 μm. (d) The peak-to-peak area (P_a) is a tool to quantitatively determine the resolution. The area between the peaks in (c), shown in the insert as the gray shaded region, was plotted as a function of the distance between neighboring nanocubes. As the distance between neighboring nanocubes approached 1.1 μm, P_a approaches 0, indicating that 1.1 μm is the spatial resolution.[12] Printed with permission from IOP Publishing.

represented the actual spatial resolution of the Raman system. This value was slightly greater than the resolution predicted by the PSF and blur value. This result suggests that Ag nanocubes with a separation less than 1.1 μm would appear as one object in the SERS image.

4.2.2 Penetration Depth

Because SERS is an optical imaging method, it will be greatly influenced by tissue scattering and blood absorption.[16,17] The penetration depth is an important parameter which describes how far light can travel into a material. For optical imaging this also includes the maximum thickness of tissue through which the detected signal can return to the surface and still be used for image construction. The transport mean free path (TMFP) is a term used to describe how far a photon of a particular wavelength can travel before experiencing severe scattering, and will therefore determine the penetration depth of the imaging modality.[18] Since the SERS imaging in this study was performed using a confocal microscopy set-up, the spatial resolution of the system should not be adversely affected as long as the image is formed within the TMFP. The TMFP has been found to be 1.1 mm for muscle tissue and 0.6 mm for brain tissue for NIR photons.[18] Should the tissue thickness exceed the TMFP, scattering will cause incident light to become too diffuse and severely reduce the spatial resolution.[18,19] Determination of the penetration depth is shown in Figure 4.3(a), where a slice of chicken tissue with gradually increasing thickness was placed on top of a film of Ag nanocubes. The SERS signal of 1,4-BDT decreased as the thickness of the tissue increased. The penetration depth appears to be around 600 μm for this system. This simple study highlights that penetration depth is a major limiting factor in the use of SERS probes for deep *in vivo* tissue imaging.

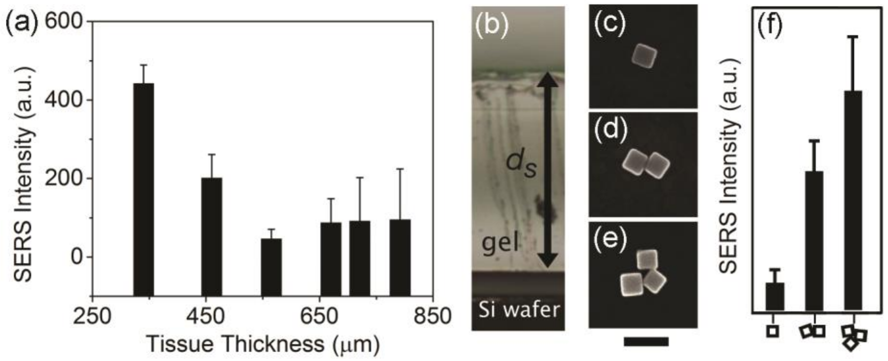

Figure 4.3. (a) The SERS intensity of the 1562 cm^{-1} peak from 1,4-BDT functionalized nanocubes as a function of the thickness of chicken breast tissue measured at 100 μm intervals along a one-dimensional path. As the thickness of the tissue increases from 380 to 800 μm the SERS signal decreases and becomes non-detectable. (b) Image of a PVA-gel on top a Si substrate that supported nanocubes. The distance from the top of the gel and the Si substrate is labeled d_s. The SERS was recorded from single nanoparticles, dimers, and trimers. d_s = 1.5 mm. (c-e) Typical SEM images of the nanocubes and their dimer and trimer configurations. Scale bar is 100 nm. (f) The relative SERS intensities from nanocubes with the morphologies indicated on the bottom axis.[12] Printed with permission from IOP Publishing.

4.2.3 The Impact of Particle Aggregation

Special considerations need to be made when using SERS as an *in vivo* imaging technique. While this study has shown that the penetration depth was quite shallow, around 600 μm, there are a range of penetration depths as determined from other groups, from 5.5 mm up to 1-2 cm.[7,11] SERS imaging studies typically do not investigate the morphology or the aggregation state of the nanoparticles in their images,[2,3,7,20] even though it is well-known that aggregation affects the SERS signals dramatically.[21] In Figure 4.3(b-f), nanocubes were deposited on a Si substrate and a PVA-gel was placed on top of them during the SERS measurements. A PVA phantom was used because the nanocubes could be visualized (by their Rayleigh scattering) through the nearly transparent gel. Figure 4.3(b) shows a side view of a typical phantom where d_s is the distance from the top of the gel to the Si substrate. The SERS signals from nanocubes with different morphologies (a single nanocube, a dimer, and a trimer as seen in Figure 4.3(c-e) were recorded. Figure 4.3(f) compares the intensities of the 1562 cm-1 band from 1,4-BDT supported on Ag nanocubes in three different aggregation states for a d_s value of 1.5 mm. It is clear that the SERS signals were detectable for all the different states of aggregation, with the signals strongly increased for the dimers and trimers. The SERS signal through the phantom was shown to increase by ×5 from a single particle to a dimer and ×10 from a single particle to a trimer. This simple demonstration clearly shows the role that aggregation plays in SERS imaging and suggests many prior studies involving Au and Ag nanoparticles might have relied on the aggregation even though this effect was never explicitly explored or stated.[1-8,22] The ability to obtain SERS images in vivo from tissues away from the skin surface should be largely determined by the aggregation states of nanoparticles, and not necessarily the SERS activity of individual nanoparticles.[7]

4.3 Multiplexed SERS Imaging

One of the major strengths of SERS imaging is its multiplexing capability, or detecting multiple probes simultaneously. SERS is not the only imaging modality capable of performing multiplexed imaging. Fluorescence microscopy, spectral CT, and MR spectroscopy can all take advantage of how different materials respond to the excitation specific to that modality. However, multiplexing with these systems quickly becomes complex. Fluorescence and MR spectroscopy require the use of different illumination sources and different RF coils, respectively, to achieve contrast between the different media.[23-25] As a result, image acquisition times may increase, and create problems with motion artifacts. Several attempts have been made to streamline multiplexed fluorescence imaging, including the use of fluorescence resonance energy transfer (FRET) and quantum dots.[26-28] Spectral CT requires multiple X-ray sources and multiple detection systems for accurate data collection.[29,30] SERS multiplexing can be performed with a single excitation wavelength and a single detector, and the signal analysis comes later. Like spectral CT, this may mean more time and computational power spent on the data analysis step post-acquisition.

Post-processing of mixed SERS signals is complex, and a good algorithm is all that is needed to harness the power of SERS multiplexing. At first glance, a simple peak-picking approach seems logical and appealing, because SERS signals are narrow and distinctive for each given SERS probe. This may only work in very simple situations, because many components of SERS spectra have overlapping peaks, and when the multiplexing number, *N*, increases, the multiple peaks become even more difficult to distinguish and separate. If complex background signals are introduced, peak-picking will not only be extraordinarily time consuming, it may also be not sensitive enough for quantitative signal analysis.

Current computational methods for separating mixed SERS signals are few and are unfortunately based on assumptions irrelevant to biology, contain unnecessary complexity, and result in large error.[3,10,31] Principle component analysis (PCA) is a powerful tool to identify the main components in a mixed SERS spectrum; however, the results are difficult to interpret.[32,33] The direct classical least-squares (DCLS) method is based on the assumption that the multiplicative fitting constants are proportional to the concentrations of the pure components.[1,10] However, in reality, these constants represent multiple factors, including concentration and the intrinsic Raman scattering cross-section of each molecule. Lutz *et al.* used a third-degree free-fitting polynomial regression (PR) model to fit their spectra and extract individual component spectra, but adding polynomials has little physical justification, even though it greatly reduces fitting error.[3]

I collaborated with the O'Sullivan group at Washington University in St. Louis to design a new algorithm for unmixing SERS signals with excellent fitting characteristics and low error. This alternating minimization (AM) method was able to accurately fit and separate signals from a mixture of SERS probes, and to map a tissue phantom with regions containing different probe mixtures.

4.3.1 Fabrication of SERS Probe and Phantom

Synthesis of Ag nanoparticle SERS probes (SNSPs) for multiplexed analysis occurred in three phases: synthesis of Ag nanocubes, functionalization, and surface passivation with silica. Specifically, Ag nanocubes with a 50 nm edge length were synthesized using a seed-mediated protocol, and then functionalized with Raman reporter molecules, which contained thiol (-SH) groups, so that a covalently attached monolayer was formed on the Ag nanocube surface. The functionalization was performed in two separate batches, with a different species of Raman reporter used in each batch: 2-napthalenethiol (2-NT) or 4-MBT, shown in Figure 4.4(a-b). The nanocubes were then coated with a silica shell to passivate the Ag surface and generate SNSPs. Figure 4.4(c) shows the Ag nanocubes with their silica coating. Subsequent functionalization of the SNSPs could then potentially be performed using binding ligands, such as antibodies, to target the SNSPs to selected cell antigens, such as those expressed on the surface of tumor cells for use in biological imaging applications.[5,11]

Mixtures of the SNSPs in different ratios were used to characterize the AM algorithm. The final test of the algorithm was its use in creating a map of a 2-dimensional phantom.

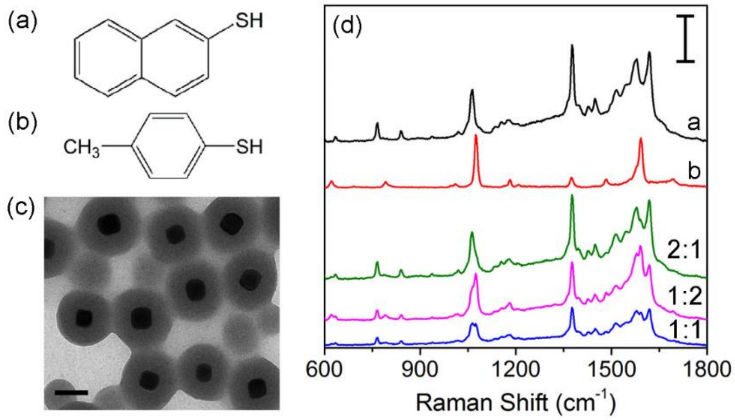

Figure 4.4. The first step in SNSP fabrication was to functionalize the Ag nanocubes with either (a) 2-NT or (b) 4-MBT and then to coat with silica. (c) TEM was used to characterize the SNSPs. Scale bar: 100 nm. (d) SERS spectra of aqueous solutions of pure SNSPs and their mixtures. Spectra have been shifted vertically for clarity. The scale bar represents a Raman intensity of 10,000 counts.[4] Printed with permission of John Wiley & Sons. Copyright 2013.

A gelatin phantom was prepared with two distinct regions. One had pure 4-MBT tagged SNSPs, and the other had a 1:1 mixture of the two different types of SNSPs. The algorithm was used to map the locations of the different types of SNSPs in a SERS image collected of the surface of the phantom.[4]

4.3.2 Signal Analysis Algorithm

Research has shown that SERS spectra from molecular probes are ideal for multiplexing because of their specificity and narrow peaks.[2,5] However, the full potential for imaging applications of SERS spectroscopy remains under-explored because of the limitations of conventional analysis methods. Using SNSPs, both PR and DCLS models were used to successfully perform multiplex analysis on the measured SERS spectra. However, the PR model may be insufficient in suboptimal conditions, such as decreased signal-to-noise ratio, high spectral peak overlap, or high *N*. And since the limit of detection

(LOD) for SERS spectroscopy is limited by the spectral fitting error, it is beneficial to include such error in the cost function. Thus, the reconstruction method developed here is an application of the Poisson model, which accommodates the photon counting nature of SERS measurements and the existence of noise in the measured data.[34] For each mixed Raman signal, constituent spectra and mixture coefficients were estimated jointly based on reference spectra that were measured in the lab. The AM algorithm is able to evaluate the entire spectral signature and quantitatively extract individual probe signals from a mixed signal, regardless of spectral peak overlap or the size of N.

In practice, the AM algorithm was applied to a SERS spectrum that was collected from a mixture composed of SNSPs functionalized with different Raman reporter molecules to extract the individual component spectra. First, the measured SERS spectrum were modeled as a linear mixture of constituent spectra

$$M_i = \sum_k H_k S_{ik}, \tag{4.1}$$

where i indexes the Raman shift, H_k is the mixture coefficient for the k^{th} constituent spectrum, and S_{ik} is the i^{th} element of the k^{th} constituent spectrum. The constituent spectra may be known, or may be inferred from reference measurements. In the latter case, the reference spectral elements are denoted by R_{ik}. Note that measurement noise is included in both the measured mixture and reference signals, which is realistic because even reference spectra have noise. The problem was to estimate both the unknown constituent spectra and the mixture coefficients given the measured data that was a mixture of signals from different Raman reporters.

I-divergence describes the discrepancy between the measured data and the data estimated by a model. Therefore, the AM algorithm was developed to minimize the I-

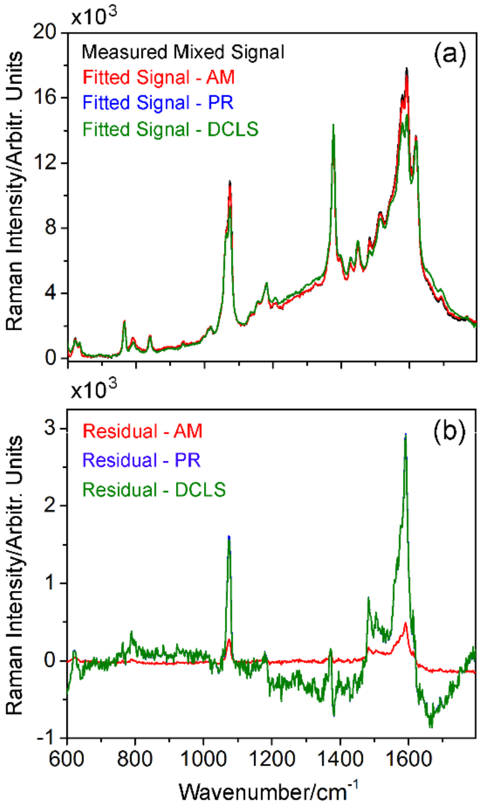

Figure 4.5. SERS spectral fitting via the AM, PR, and DCLS algorithms. (a) The measured mixed signal of a solution with a 1:2 ratio of SNSPs functionalized with either 2-NT or 4-MBT, respectively, is shown in black along with the calculated fits using the AM (red), PR (blue), and DCLS (green) algorithms. (b) The residuals were calculated from the fits in panel (a) with respect to the measured signal. The fitting error was 1.7% for the AM algorithm, compared to 9.2% error for each the PR and DCLS algorithms.[4] Printed with permission of John Wiley & Sons. Copyright 2013.

divergence. This is appropriate for analyzing Raman signals because the photon counting nature of SERS measurements can be represented by a Poisson model. Maximizing the Poisson log-likelihood function is equivalent to minimizing I-divergence.[35,36] In this model, the I-divergences for two separate problems are included: fitting the overall mixed signal and extracting individual spectra from that mixed signal. The complete details of the algorithm can be found in the Section 4.5.6.

By applying this AM algorithm to the mixed spectra, the component spectra were

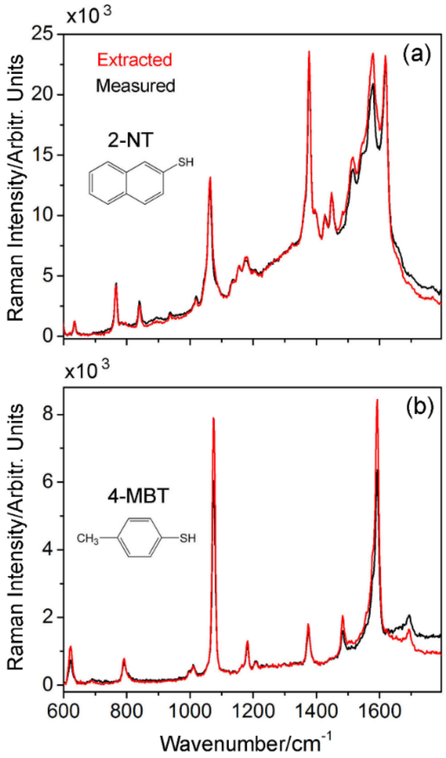

Figure 4.6. Plots of the reference spectra and the extracted spectra using the AM algorithm. The individual spectra were extracted from the measured spectrum of a 1:2 mixture of SNSPs functionalized with (a) 2-NT and (b) 4-MBT.[4] Printed with permission of John Wiley & Sons. Copyright 2013.

separated with high precision. The results from a mixture of SNSPs tagged with 2-NT and 4-MBT in a ratio of 1:2 are shown in Figures 4.5 and 4.6. Figure 4.5 compares the SERS spectral fitting acquired via the PR, DCLS, and AM algorithms, and Figure 4.6 compares the spectrum of each extracted individual component and its corresponding reference. From Figure 4.5(a), the extracted signal using the AM method is shown to be almost indistinguishable from the measured mixed signal. Figure 4.5(b) gives a quality assessment of the three methods (PR, DCLS, and AM) by plotting the residuals of the fitted mixed signal and the measured mixed signal. By defining the overall fitting error as norm(M-SH)/norm(M), the AM method gave a fitting error of 1.7%, while the PR and DCLS methods gave a fitting error of 9.2%. The residuals are not around 0 and there appears to be a systematic error near the peak, but the errors are much smaller than the other available models.

The parameters λ_1 and λ_2 give the user control over the trade-off between the quality of fit to the mixed signal and the quality of the extracted signals when compared to the references. Larger λ values emphasize the second term of the objective function (found in Section 4.5.6, Equation 4.5), and will therefore produce individual extracted signals that will be close to the component's reference signals. Conversely, smaller λ values cause the first term to dominate the objective function, so the fit to the mixed signal will be very good, reducing the overall fitting error at the expense of the individual extraction error. These trends are illustrated in Figure 4.7. One of the advantages of the AM method is that this trade-off provides flexibility according to the needs of the specific imaging problem. For example, the results presented in Figures 4.5 and 4.6 were obtained using $\lambda_1 = 0.2$ and $\lambda_2 = 0.5$. Using these two values for λ, the convergence time for this experiment was 0.6 s for the full 78 iterations, when performed on a 2.3 GHz Intel Core i7 processor, and the tolerance of error was 10^{-6}. These values were chosen to balance the λ trade-off by achieving a relatively small overall fitting error while maintaining a small average individual extraction error. These values can be changed according to the different capabilities of scattering for different molecules, the concentration of SNSPs, and the measurement precision of the experimental equipment. Figure 4.7 shows the dependence of fitting error and individual extraction error as λ_1 and λ_2 were changed. Here, the ratio λ_1:λ_2 remained at 2:5 so that the individual extraction errors for both extracted spectra are almost the same; otherwise, one extracted spectrum would deviate greatly from its

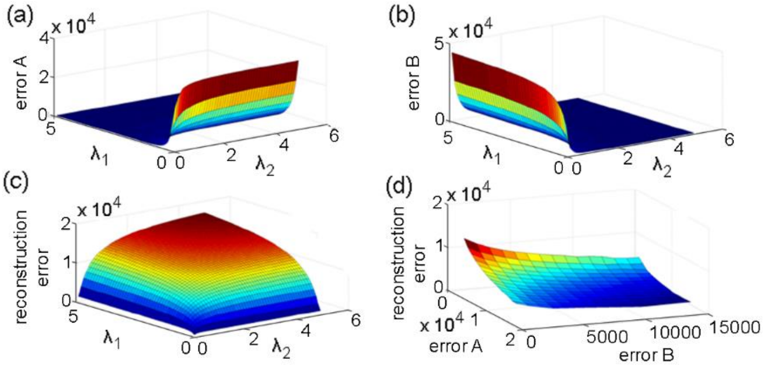

Figure 4.7. 3D surface plots showing (a and b) the individual extraction errors and (c) the reconstruction error as functions of λ_1 and λ_2, as well as (d) the reconstruction error as a function of the individual extraction errors.[4] Printed with permission of John Wiley & Sons. Copyright 2013.

reference while the other would be indistinguishable from its reference. This setting is reasonable because the measurements for both reference spectra were performed under the same experimental conditions. From Figure 4.7, it is clear that as the amplitude of each λ increases, the overall fitting error increases while the average individual extraction error decreases. The trend is not linear and tends to saturate as λ increases. As stated before, larger λ values give prior expectation that the extracted spectra will be very close to their references, whereas smaller λ values focus more on minimizing the error of the measured mixed data and the data estimated by the model.

4.3.3 Mapping Areas of Mixed SERS Probes

The AM algorithm was also able to map an image of a phantom with two distinct regions, as shown in Figure 4.8. A gelatin phantom was prepared that had a region of pure 2-NT conjugated SNSPs and a region of a 1:1 (2-NT:4-MBT) mixture of SNSPs. There was no clear difference between the regions simply by visualizing with a white-light optical microscope. Applying the AM algorithm to the spectra collected from a series of points on

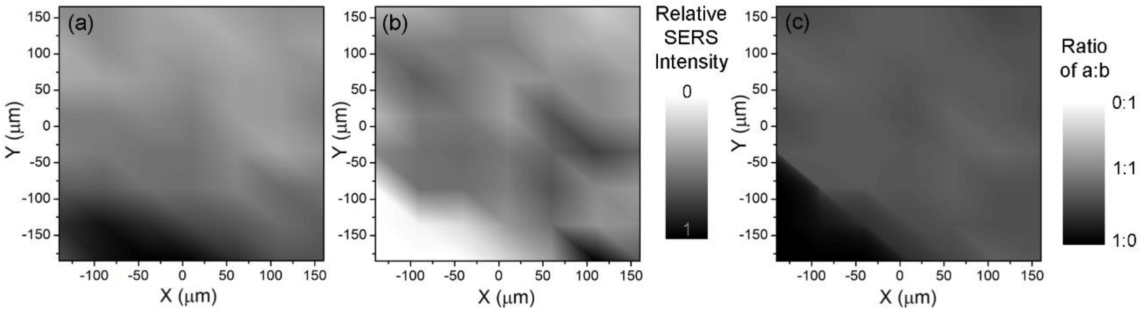

Figure 4.8. SERS mapping image of a tissue phantom containing two regions with different ratios of SNSPs. The two regions have 2-NT:4-MBT ratios of 1:0 and 1:1. Panels (a) and (b) show the signal from individual molecules 2-NT (a) and 4-MBT (b) separately, and panel (c) shows the merged image.[4] Printed with permission of John Wiley & Sons. Copyright 2013.

the surface, however, was able to draw the boundary between the two regions.

4.4 Summary

Imaging with SERS holds great promise for the medical imaging community. This work represents the first characterization of the imaging capabilities and limitations of a SERS imaging system by using well-defined nanoparticles as the substrate. It also demonstrated the power of multiplexed SERS imaging, and addressed some of the computational problems associated with multiplexing.

The Raman system could resolve individual Ag nanocubes that were separated by a distance of ~1.1 µm on a Si substrate. Importantly, in phantom experiments, SERS signals were shown to increase with the formation of simple aggregates such as dimers and trimers. Larger aggregates could be responsible for some of the unusual penetration depths reported in the literature in addition to the resonance effects of the dyes used as probe molecules.[7,11] Nanoparticle aggregation is an important variable for SERS imaging in vivo, and that a better control over the aggregation state of nanoparticles may lead to greater penetration depths. However, as an optical imaging modality, there will be a limit to the depth of penetration and quality of images collected *in vivo*.

The AM method for collecting and analyzing multiplexed SERS images developed in collaboration with the O'Sullivan group at Washington University in St. Louis provides several key improvements over other existing methods. It treats the references as measurements, accounting for the randomness and nonlinear noise in the measured data, which is more realistic for SERS measurements. Therefore, it can reduce error resulting from noise with relatively low computational cost and is quite robust to noisy data. Furthermore, the AM method inherently guarantees global minimum achievement and monotonic convergence. Potential limitations of the AM algorithm include that it is iterative and more computationally involved than other single processing methods like PR and DCLS. However, this expense can be justified by more accurate results, an acceptable convergence rate, and the robustness that the AM method provides. Experiments to test the accuracy of this method showed it to be robust and precise in mapping regions containing different SERS probes, and determining the ratio between the probes.

4.5 Experimental Details

4.5.1 Synthesis and Functionalization of Ag Nanocubes

Silver nanocubes of different sizes were synthesized using the seed-mediated approach described in Chapter 2, Section 6.1. The single Ag nanocubes used to determine the fundamental imaging parameters were 100 nm along the edge, and the Ag nanocubes used to fabricate the SNSPs were 50 nm.

For the 100-nm Ag nanocubes, functionalization was performed by mixing 10 μL of the as-prepared suspension to 100 μL of 1 mM 1,4-benzenedithiol (1,4-BDT, Aldrich) in ethanol. After incubation at room temperature for 1 h, the 1,4-BDT should have formed a self-assembled monolayer on the surface of the Ag nanocubes and could then be used as a SERS probe with well characterized SERS peaks, in particular the peak at 1562 cm^{-1}.[18]

For the preparation of SNSPs, solutions of Raman reporters were prepared in ethanol, using 2-NT (0.01 M, Sigma Aldrich) and 4-MBT (0.01 M, Sigma Aldrich). The water was removed from 500 µL aliquots of Ag nanocubes via centrifugation (9.2 g, 8 min) and was replaced with 1 mL of 2-NT or 4-MBT solutions. After 1 h of functionalization time, the particles were washed twice with ethanol, and were resuspended with 200 µL ethanol. The Ag nanocubes were coated in silica by adding the Ag nanocube suspension to a mixture of 1.5 mL ethanol and 0.25 mL water.[37] To this mixture were added 65 µL ammonium hydroxide (Fisher Scientific) and 10 µL tetraethyl orthosilicate (TEOS, Sigma Aldrich). The mixture was stirred at 200 rpm for 3 h and washed twice with ethanol and then twice with water. Characterization of both pristine Ag nanocubes and silica coated SNSPs were carried out using a TEM (FEI G2 Spirit Twin) operated at acceleration voltage of 120 kV.

4.5.2 SERS Measurements and Mapping

The SERS spectra were recorded using the Raman spectrometer described in Chapter 2, Section 6.3. The excitation wavelength used for the fundamental imaging studies was 785 nm generated by a semiconductor c.w. diode laser The power of the laser was 3.1 mW, and the acquisition times varied, as noted, from 2-45 s. The excitation wavelength used for the multiplexing studies was 514 nm. Data from the solution phase was collected with a laser power of 5 mW for 60 sec exposure time.

Mapping was accomplished with a high-speed encoded stage (HSES) system capable of step sizes of 100 nm in the *x*, *y*, and *z* dimensions at speeds of 80 mm/s and a range of

112 mm in *x* and 76 mm in *y*. The two-dimensional SERS images were generated using Renishaw's WiRE Mapping Review software (Renishaw plc, Gloucestershire, UK). The intensity of a selected peak for each data collection point was mapped as two-dimensional images based on the (*x*, *y*) coordinates, which provided a map of the spatial distributions of Ag nanocubes. The images were further modified with the WiRE software, or converted into a matrix with Origin software for the determination of peak-to-peak areas and image analysis with Matlab.

Sample cells consisted of 50 µL liquid sample placed into microcentrifuge tube cap attached to a glass slide. A thin glass cover slip (0.17 mm) was placed on top of the sample's meniscus to prevent evaporation and to act as a reference point from which the focal plane was lowered 200 µm into the sample.

The gelatin phantom containing SNSPs was prepared to have two distinct regions of different SNSPs. First, a solution of as-prepared SNSPs functionalized with 2-NT were mixed with a small volume of 15% (w/v) gelatin, and allowed to solidify at 4 °C. Half of the solid phantom was cut away, and refilled with a different solution of 15% gelatin mixed with a 1:1 ratio of 2-NT and 4-MBT conjugated SNSPs. A SERS image was collected over a 350 µm square area at the interface of the two regions on the surface of the gelatin phantom.

Fundamental data processing was performed using OriginPro v. 8.1, Student edition (OriginLab Corp., Northampton, MA). The data was baseline corrected to flatten the spectra. The fitting algorithms and mathematical models were performed using Matlab v. 7.6 R2008a (Mathworks Inc., Natick, MA).

4.5.3 Determination of Blur and Resolution

SERS images were recorded from individual Ag nanocubes using the Renishaw Raman spectrometer. The samples were prepared by drop casting an ethanol suspension of the functionalized Ag nanocubes onto a Si substrate that had been patterned with registration marks *via* lithography or by simply scoring the substrate with a diamond pen. The substrate was briefly rinsed with ethanol to remove any dust that may interfere with locating the Ag nanocubes under a dark-field optical microscope. The Ag nanocubes were allowed to dry under ambient conditions and the locations of many nanocubes (typically 20 to 50) were identified by their Rayleigh scattering image using the dark-field microscope and their positions were noted for correlation with SEM. After the Ag nanocubes had been probed with SERS, the sample was immediately imaged by SEM to determine the sizes, shapes, and orientations of the nanocubes.

The SEM images, dark-field images, and two-dimensional SERS images were compared to determine the blur value of the SERS imaging system by measuring the diameter of the Ag nanocubes represented in each imaging modality. Resolution was calculated based on the ability to distinguish between two neighboring Ag nanocubes using a peak-to-peak area calculation. The signal intensity of the peak at 1562 cm^{-1} was plotted with respect to distance in the x-direction. As the area between the signal peaks of two neighboring Ag nanocubes approached zero, the resolution limit of the imaging system would be reached. The effect of imaging parameters on resolution was examined by collecting two-dimensional scans of functionalized Ag nanocubes on a Si substrate at different step sizes: 300 nm, 700 nm, 1.5 μm, 3 μm, and 5 μm. The SERS signals at different points were mapped, and the area between the peaks was calculated.

4.5.4 Calculation of Point Spread Function

The lateral PSF of the confocal Raman microscope was plotted in Matlab v. 7.10 (Mathworks, Inc,. Natick, MA) using the following equation:[15]

$$\mathrm{PSF}(v) = \left| \frac{2J_1(v)}{v} \right|^4 , \qquad (4.2)$$

where J_1 is a first-order Bessel function of the first kind and v is the radial normalized optical coordinate:

$$v = \frac{2\pi \sin\gamma}{\lambda} r \, . \qquad (4.3)$$

The radius, r, is the distance from the object point in the x, y plane, λ is the wavelength of the laser, and γ is the angle that defines the numerical aperture (NA) of the objective along with the refractive index, n, of the medium. This was calculated based on the following equation, with the NA of this Raman system being 0.9:

$$0.9 = n \sin\gamma \, . \qquad (4.4)$$

4.5.5 Determination of Penetration Depth

The PVA gels were formed by allowing aqueous solutions of PVA to stand at room temperature. The mechanical properties were enhanced by freezing and then thawing the gel to encourage more cross-linking between the chains. This method is based on the concept of physical cross-linking, and avoids the need for additives or complex procedures involved in chemical cross-linking. By optimizing the number of freezing and thawing cycles, PVA gels with optical properties similar to those of soft tissue can be obtained.[38] Gels were cast and then frozen for 12 h followed by a thawing period of 12 h in one cycle, and 4 cycles were used to obtain the PVA phantoms used here. The SERS spectra were collected through the gel phantom from individual Ag nanocubes and aggregates of various sizes, as determined by the Rayleigh scattering image and SEM.

Chicken tissue was used to examine the impact of scattering in a realistic tissue environment. Chicken breast tissue, obtained from a local grocery store, was frozen and then sliced with a Xacto knife to obtain wedge-shaped pieces, such that the thickness increased gradually across its width. The tissue was placed on top of a monolayer of the functionalized Ag nanocubes. After focusing the laser on the surface of the Si coated with Ag nanocubes, SERS spectra were collected at 100 μm intervals through the tissue with increasing thickness. Signal intensity from the 1,4-BDT ring stretching mode at 1562 cm^{-1} was plotted at each point alongside the thickness of the tissue at that point. Processing of the raw SERS data was carried out using OriginPro v. 9, student version (OriginLab, Corp., Northampton, MA) and analysis was performed using Matlab.

4.5.6 Alternating Minimization Algorithm for Multiplexed SERS Analysis

The AM algorithm aims to minimize the I-divergence for two separate problems, fitting the overall mixed signal and extracting individual spectra from that mixed signal. The following objective function, *L*, was therefore used to accomplish this:

$$L(\mathbf{S},\mathbf{H}) = \sum_i \left[M_i \log \frac{M_i}{\sum_k H_k S_{ik}} - M_i + \sum_k H_k S_{ik} \right] \qquad (4.5)$$

$$+ \sum_k \lambda_k \sum_i \left[R_{ik} \log \frac{R_{ik}}{S_{ik}} - R_{ik} + S_{ik} \right]$$

where λ_k represents the weighting factor for each component. This objective function can also be interpreted as the trade-off in the quality of the fit between the measured data and the reference spectra. The first term represents the discrepancy between the measured mixed data and the data estimated by the model to represent the mixture, and the second term represents the discrepancy between the reference spectra and the extracted spectra. Following O'Sullivan,[39] a variational representation of this objective function was introduced, with the goal of deriving an AM algorithm for the quantities of interest. The resulting representation is:

$$\mathbf{L}(\mathbf{S},\mathbf{H}) = \min_{\mathbf{Q}\in\mathcal{Q}} \mathbf{J}(\mathbf{S},\mathbf{H},\mathbf{Q}) \tag{4.6}$$

where *J* is the new objective function

$$\mathbf{J}(\mathbf{S},\mathbf{H},\mathbf{Q}) = \sum_i \sum_k \left[M_i Q_{k|i} \log \frac{M_i Q_{k|i}}{S_{ik} H_k} - M_i Q_{k|i} + S_{ik} H_k \right] + \sum_i \sum_k \lambda_k \left[R_{ik} \log \frac{R_{ik}}{S_{ik}} - R_{ik} + S_{ik} \right], \tag{4.7}$$

and where *Q* is a variational term that is non-negative and satisfies linear constraints

$$Q_{k|i} \in \mathcal{Q} = \left\{ Q_{k|i} : Q_{k|i} \geq 0, \sum_k Q_{k|i} = 1, \forall i \right\}. \tag{4.8}$$

Due to the photon counting nature of SERS measurements, the problem was reduced to a linear inverse problem subject to non-negativity constraints (i.e., $A_i \geq 0$, $B_i \geq 0$). The AM algorithm asymptotically achieves the global minimum and converges monotonically.[35] All these properties make the AM algorithm ideal for implementation with SERS spectral fitting, which was performed as follows:

1. Initial guesses for *A* and *B* were made based on R_a and R_b, respectively. The initial value of $Q_{k|i}$ was set such that $Q_{1|i} = Q_{2|i} = 0.5$, ∀i.

2. Minimization over *H* was accomplished by fixing the values of $Q_{k|i}$, *A*, and *B*, and then taking the derivative of the objective function with respect to H_k and then equating that result to zero:

$$H_k^{(n+1)} = \frac{\sum_i M_i Q_{k|i}^{(n)}}{\sum_i S_{ik}} \tag{4.9}$$

3. S was minimized by fixing the values of $Q_{k|i}$ and H_k were fixed, and then taking the derivative of the objective function with respect to S_{ik} and then equating that result to zero:

$$S_{ik}^{(n+1)} = \frac{M_i Q_{k|i}^{(n)} + \lambda_k R_{ik}}{\lambda_k + H_k^{(n+1)}} \tag{4.10}$$

4. Then, the values of S_{ik} and H_k were fixed, while Q was minimized by taking the derivative of the objective function with respect to $Q_{k|i}$ and then equating that result to zero:

$$Q_{k|i}^{(n+1)} = \frac{S_{ik}^{(n+1)} H_k^{(n+1)}}{M_i} \tag{4.11}$$

5. Finally, the overall fitting error for the AM algorithm was determined to be:

$$\varepsilon^{(n+1)} = M - S^{(n+1)} * H^{(n+1)} \tag{4.12}$$

If the error did not decrease significantly ($\Delta\varepsilon < 10^{-6}$), the algorithm terminated and the fitted model was plotted; otherwise, *n* was incremented and steps 2-5 were repeated.

4.6 References

[1] C. L. Zavaleta, B. R. Smith, I. Walton, W. Doering, G. Davis, B. Shojaei, M. J. Natan, and S. S. Gambhir. *Proc. Natl. Acad. Sci*. 2009, **106**, 13511.

[2] K. W. Kho, C. Y. Fu, U. S. Dinish, and M. Olivo. *J. Biophotonics* 2011, **4**, 667.

[3] B. R. Lutz, C. E. Dentinger, L. N. Nguyen, L. Sun, J. Zhang, A. N. Allen, S. Chan, and B. S. Knudsen. *ACS Nano* 2008, **2**, 2306.

[4] Y. Chen, C. H. Moran, Z. Tan, A. L. Wooten, and J. A. O’Sullivan. *J. Raman Spectrosc*. 2013, **44**, 703.

[5] J.-H. Kim, J.-S. Kim, H. Choi, S.-M. Lee, B.-H. Jun, K.-N. Yu, E. Kuk, Y.-K. Kim, D. H. Jeong, M.-H. Cho, and Y.-S. Lee. *Anal. Chem*. 2006, **78**, 6967.

[6] M. Y. Sha, H. Xu, M. J. Natan, and R. Cromer. *J. Am. Chem. Soc*. 2008, **130**, 17214.

[7] X. Qian, X.-H. Peng, D. O. Ansari, Q. Yin-Goen, G. Z. Chen, D. M. Shin, L. Yang, A. N. Young, M. D. Wang, and S. Nie. *Nat. Biotech*. 2008, **26**, 83.

[8] S. Lee, S. Kim, J. Choo, S. Y. Shin, Y. H. Lee, H. Y. Choi, S. Ha, K. Kang, and C. H. Oh. *Anal. Chem*. 2007, **79**, 916.

[9] B.-H. Jun, J.-H. Kim, H. Park, J.-S. Kim, K.-N. Yu, S.-M. Lee, H. Choi, S.-Y. Kwak, Y.-K. Kim, D. Jeong, M.-H. Cho, and Y.-S. Lee. *J. Comb. Chem.* 2007, **9**, 237.

[10] L. Sun *et al. Nano Lett*. 2007, **7**, 351.

[11] S. Keren, C. Zavaleta, Z. Cheng, A. de la Zerda, O. Gheysens, and S. S. Gambhir. *Proc. Natl. Acad. Sci.* 2008, **105**, 5844.

[12] C. H. Moran, M. Rycenga, X. Xia, C. M. Cobley, and Y. Xia. *Nanotechnology* 2013, in press.

[13] P. Sprawls. Blur, Resolution, and Visibility of Detail. *Physical Principles of Medical Imaging*. (Madison, WI: Medical Physics Pub Corp) 1995.

[14] M. Xu and L. V. Wang. *Rev. Sci. Instrum.* 2006, **77**, 041101.

[15] L. V. Wang and H. Wu. *Biomedical Optics: Principles and Imaging*. (Hoboken, NJ: John Wiley & Sons) 2007, pp 166-167.

[16] V. Ntziachristos, C. Bremer, and R. Weissleder. *Eur. Radiol.* 2003, **13**, 195.

[17] H. F. Zhang, K. Maslov, G. Stoica, and L. V. Wang. *Nat. Biotech.* 2006, **24**, 848.

[18] V. Ntziachristos. *Nat. Methods* 2010, **7**, 603.

[19] Y. Liu, C. Zhang, and L. V. Wang. *J. Biomed. Opt.* 2012, **17**, 126014.

[20] S. W. Joo, S. W. Han, and K. Kim. *J Colloid Interface Sci.* 2001, **240**, 391.

[21] P. H. C. Camargo, W. Li, L. Au, M. Rycenga, and Y. Xia. *J. Phys. Chem*. 2009, **484**, 304.

[22] H. Chon, S. Lee, S. W. Son, C. H. Oh, and J. Choo. *Anal. Chem*. 2009, **81**, 3029.

[23] M. van der Graaf. *Eur. Biophys. J.* 2010, **39**, 527.

[24] M. Thakur, D. Melnik, H. Barnett, K. Daly, C. H. Moran, W.-S. Chang, S. Link, C. T. Bucher, C. Kittrell, and R. Curl. *J. Biomed. Opt.* 2010, **15**, 026126.

[25] K. D. Barbee, A. P. Hsiao, E. E. Roller, and X. Huang. *Lab Chip* 2010, **10**, 3084.

[26] A. Wagh, F. Jyoti, S. Mallick, S. Qian, E. Leclerc, and B. Law. *Small* 2013, **9**, 2129.

[27] I. Krylova, R. R. Kumar, E. M. Kofoed, and F. Schaufele. *PLOS One* 2013, **8**, e63286.

[28] M. Han, X. Gao, J. Z. Su, and S. Nie. *Nat. Biotech.* 2001, **19**, 631.

[29] J. P. Schlompka *et al. Phys. Med. Biol*. 2008, **53**, 4031.

[30] M. Karcaaltinçaba and A. Aktaş. *Diagn. Interv. Radiol.* 2011, **17**, 181.

[31] Y. Cui, B. Ren, J.-L. Yao, R.-A. Gu, and Z.-Q. Tian. *J. Raman Spectrosc.* 2007, **38**, 896.

[32] A. F. McCabe, C. Eliasson, R. A. Prasath, A. Hernandez-Santana, L. Stevenson, I. Apple, P. A. G. Cormack, D. Graham, W. E. Smith, P. Corish, S. J. Lipscomb, E. R. Holland, and P. D. Prince. *Faraday Discuss.* 2006, **132**, 303.

[33] D. A. Watson, L. O. Brown, D. R. Gaskill, M. Naivar, S. W. Graves, S. K. Doorn, and J. P. Nolan. *Cytometry A* 2008, **73A**, 119.

[34] C. L. Haynes, A. D. MacFarland, and R. P. Van Duyne. *Anal. Chem.* 2005, **338A**.

[35] J. A. O'Sullivan, in *Codes, Curves, and Signals: Common Threads in Communications*, (Ed: A. Vardy), Kluwer Academic, Norwell, MA, **1998**, pp. 173-192.

[36] D. M. Titterington, *IEEE Trans. Med. Imaging* 1987, **6**, 52.

[37] S. P. Mulvaney, M. D. Musick, C. D. Keating, and M. J. Natan. *Langmuir* 2003, **19**, 4784.

[38] A. Kharine, S. Manohar, R. Seeton, R. G. M. Kolkman, R. A. Bolt, W. Steenbergen, and F. F. M. de Mul. *Phys. Med. Bio.* 2003, **48**, 357.

[39] J. A. O'Sullivan, J. Benac, *IEEE Trans. Med. Imaging* 2007, **26**, 283.

CHAPTER 5: POLYMER HOLLOW BEADS FOR ENCAPSULATION OF IMAGING CONTRAST AGENTS

5.1 Introduction

With the increasing reliance on medical imaging, development of contrast agents has become a vital field of research. Designing particle-based contrast agents, as discussed in Chapter 1, is a popular approach due to the flexibility and multimodal capability of particles. However, not all contrast-enhancing compounds are amenable to fabrication in particle form, or are too toxic to be used *in vivo*. The design of a carrier platform, such as hollow particles, for encapsulation of these materials is one solution to this problem.

Hollow particles can encapsulate a contrast agent to minimize its potential toxicity, improve its stability in biological media, and reduce the concentration necessary for effective enhancement.[1-3] Encapsulating a contrast agent in a hollow particle will isolate it from the biological environment, and thus be an effective way to improve its stability regardless of the means of administration. Additionally, the external surface of the hollow particle shells may also serve as a platform for bioconjugation, opening the door to targeted delivery and molecular imaging.[4]

The size of the hollow particles can also be controlled as a key design parameter, since size will impact their circulation half-life and the targeting ability. Capillaries, the smallest blood vessels, typically measure 5-10 μm in diameter. Particles used for contrast enhancement should at least be smaller than 5 μm in diameter to prevent capillary occlusion.[5] However, the RES will reduce the circulation half-life of particles larger than 100 nm in diameter and increase their accumulation in the liver.[6,7] Therefore, the size of the particles should be tailored based on the particular imaging modality and target, as should the mode of delivery. For example, commercially available microbubbles for ultrasound imaging are administered by intravenous injection and their diameters are in the range of 1-5 μm, which suits the imaging needs for ultrasound applications.[8,9]

There are many approaches to fabricating hollow particles since encapsulation has found widespread use in many applications such as controlled release of drugs, cosmetics, inks, chemical reagents, or biologically active species.[10-14] Materials frequently utilized for hollow particle synthesis include polymers,[15-18] lipids,[19] and proteins.[20] The two most commonly used methods for encapsulation with hollow particles are based on microemulsion[21-23] and sacrificial templating.[24-27] Despite their popularity, there are some disadvantages and limitations associated with these two methods. For example, the hollow particles fabricated by microemulsion usually have a broad size distribution, although optimizing the experimental parameters of emulsion processes may achieve reasonable monodispersity for the particles. In addition, the specific pairings of core and shell materials are limited, and non-uniform loading of the particles is generally observed. However, microemulsion has a major advantage of accomplishing the particle synthesis and encapsulation processes simultaneously. The particles fabricated using a sacrificial template tend to be more uniform in size, but loading the hollow core must occur after etching away the template. Therefore, the only pathway for loading relies on passive diffusion through the shell, which is not an efficient and universal solution for all types of contrast agents, especially not for macromolecules or nanoparticles.

5.2 Polystyrene Hollow Beads for the Encapsulation of Contrast Agents

I chose to develop an encapsulation system based on hollow polymer particles. Polystyrene (PS) is a nontoxic, though not biodegradable, polymer. It is used to fabricate microparticles and nanoparticles with highly uniform size distributions, which is very important for encapsulation. A uniform size will ensure that approximately the same amount of material is encapsulated in each hollow particle. A protocol was previously developed in the Xia group for fabricating hollow PS beads with a single hole on the surface.[28,29] This unique structure allows the cavity to be easily filled by using reduced pressure to fill the hollow beads with any desired payload. The hole is large enough to fit solutions of proteins or dyes, or even suspensions of nanoparticles. Once loaded, the holes were sealed by annealing the hollow beads at a temperature elevated slightly above the glass transition temperature (T_g) of PS.[1]

I initially used the unique design of the hollow PS beads with the hole on the surface to encapsulate a material not traditionally used as a contrast agent – sodium chloride (NaCl). Thermoacoustic tomography (TAT) uses microwave source for excitation of thermoelastic expansion of tissue for imaging with ultrasound. In order to use TAT to detect diseases such as breast cancer in the very early stages, a good contrast agent must be developed.[30] As discussed in Chapter 1, very few materials have been explored as viable contrast agents for TAT.[30,31] Since saline heats better than pure water when exposed to microwaves, NaCl encapsulated at concentrations higher than the normal physiologic level should provide contrast enhancement with TAT.[32] Encapsulation is necessary because it would be impossible to develop NaCl particles for contrast since contact with water would result in their rapid dissolution upon injection.

In addition to use for imaging with TAT, the beads were also used for encapsulation of iodinated contrast compounds (ICC) for CT and perfluorooctane (PFO) for MR imaging. While ICC is a common CT contrast agent, it causes allergic reactions in some patients, and has exhibited toxicity.[33] Encapsulation in a particle could also provide improved circulation times for ICC.[34] PFO is a volatile liquid, not amenable for direct injection. In these three cases, hollow beads can serve as an ideal vector for harnessing the potentially powerful contrast enhancement from these compounds by protecting them within the sealed hollow bead.

5.2.1 Fabrication of PS Hollow Beads

The PS hollow beads were initially prepared with a small hole on the surface by swelling commercial PS latex beads with toluene, followed by freeze-drying.[28,29,35] As the toluene swells the PS beads, the radius increases about 30%, although this value can be adjusted by changing the type of solvent or the volume added.[29] When the swollen particles freeze quickly when dropped into a vial containing liquid nitrogen, a chilling -210 °C. Since polymers are poor thermal conductors, a temperature gradient forms within an individual particle, with the outside freezing before the center. As the PS-toluene mixture freezes, the density increases and the polymer shrinks.[29] This gradient likely causes a small cavity to form in the center of each bead as it freezes.

The frozen sample is then placed in a vacuum freeze-dryer for 24 hours, which kept the temperature of the sample at –89 °C. Toluene has a melting point of –93 °C, so it evaporates in the vacuum freeze-dryer. The cavity inside the PS particles will grow with the flux of evaporating toluene. Eventually, one side of the interior cavity will come into contact with the outer surface, creating a hole.

5.2.2 Encapsulation of Contrast Agents for TAT, CT, and MRI

Figure 5.1 shows how to encapsulate three different types of contrast agents suitable for various imaging modalities: *i*) saline solutions (or NaCl microcrystals) for TAT; *ii*)

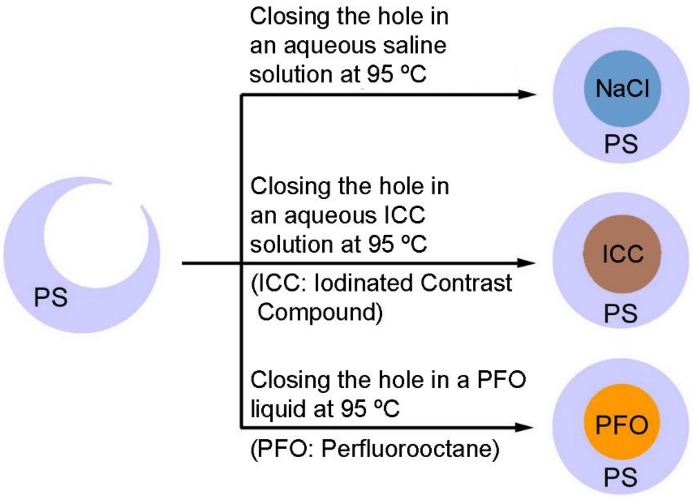

Figure 5.1. Schematic illustration of the procedure for closing the hole on the surface of a PS hollow bead while an imaging contrast agent is being encapsulated.[1] Printed with permission of John Wiley & Sons. Copyright 2012.

ioversol, an iodinated contrast compound (ICC), for micro-CT; and *iii*) PFO for MR imaging. These three types of contrast agents possess completely different physical properties, but all of them can be supplied as solutions or pure liquids for the purpose of encapsulation. The mixture was typically subjected to a vacuum for a short period of time to induce a quick flow of the contrast agent into the cavity through the small hole on the surface.

The hole on the surface was then sealed using a thermal annealing process, encapsulating the contrast agent within the PS hollow bead. Heating the mixture to a temperature (95 ºC) slightly above the T_g of PS, causing the migration of polymer chains within each particle. As a result, the PS shell became more or less uniform in terms of thickness as the hole was closed on the surface of each PS hollow bead and a spherical cavity was generated in the interior. When the solvent evaporated during sample preparation for microscopy, the solute (NaCl or ICC) remaining in the core of a hollow bead tended to precipitate out as a solid. Such samples could then be imaged by TEM to collect direct evidence for contrast agent encapsulation. Contrast agents such as PFO that remained in a liquid state at room temperature had to be characterized using a spectroscopic method rather than TEM.

Figure 5.2(a,b) shows SEM and TEM images of the as-prepared PS hollow beads with a hole on the surface. It is clear that the solid PS beads (1.89 ± 0.03 μm in diameter and standard deviation) had been transformed into hollow beads with an average outer diameter of 2.61 ± 0.04 μm and a hole of 0.38 ± 0.04 μm on the surface. Their spherical shape and uniformity in size were both retained during the swelling and freeze-drying processes. The hole could be gradually closed by annealing the sample at a temperature (e.g., 95 ºC) slightly above the T_g of PS. Figure 5.2(c,d) shows SEM and TEM images of the same batch of PS hollow beads after the sample had been annealed in water at 95 ºC for 5 min. In this case, the average diameter of the hole on the surface of the PS hollow beads was reduced from 0.38 to 0.10 μm. As shown in Figure 5.2(e,f), the hole on the surface of the PS hollow beads were completely closed when the annealing time was increased to 30 min. In this case, the PS beads still had a hollow, spherical cavity in the interior while the outer diameter had been slightly reduced to 2.42 μm. Since the size of the hole on the surface can be controlled based on the choice of solvent used to swell the beads and the rate of subsequent evaporation, it is possible to make hollow beads with a hole that is much larger than those used here. As shown previously, it was still possible to seal a hole of 0.5-1 μm in diameter using thermal annealing or treatment with a good solvent for the polymer.[28]

No polymer degradation was observed because the annealing temperature was well below the decomposition temperature of polystyrene (350-500 ºC).[36] Additionally, there

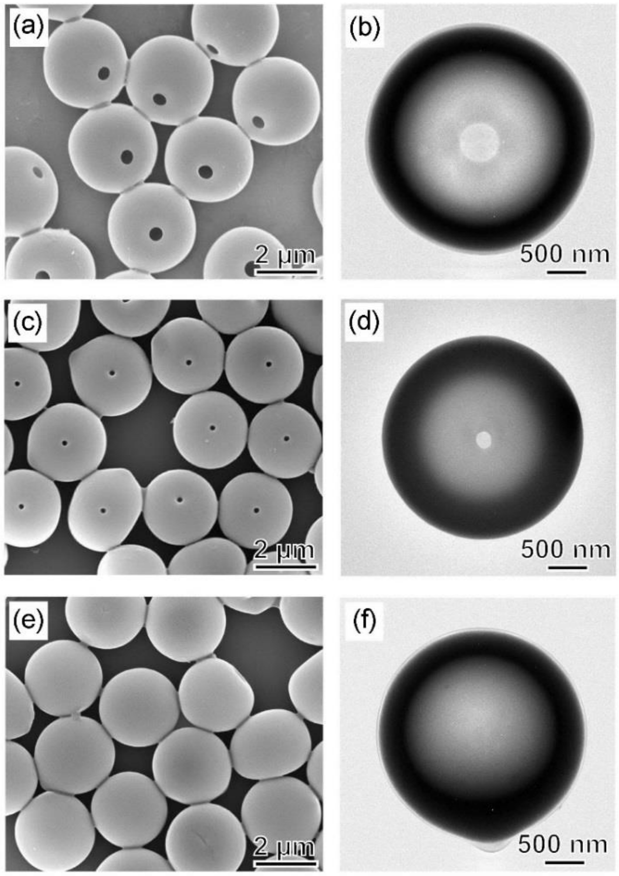

Figure 5.2. (a) SEM and (b) TEM images of the as-prepared PS hollow beads with a hole on their surface; (c) SEM and (d) TEM images of the same batch of PS hollow beads after the hole had been partially closed by annealing the system in water at 95 ^{o}C for 5 min; (e) SEM and (f) TEM images of the same batch of PS hollow beads after the hole had been completely closed by annealing the system in water at 95 ^{o}C for 30 min.[1] Printed with permission of John Wiley & Sons. Copyright 2012.

was no aggregation observed during the annealing process, which can be attributed to two main factors. First, a relatively low concentration of PS beads was used, thereby reducing the likelihood of collision and aggregation. Second, the PS beads contained slight negative charges from the sulfate ester used by the manufacturer during synthesis. This provided an electrostatic repulsion force capable of stabilizing the PS beads, even at elevated temperatures.

Saline-encapsulated PS hollow beads were initially prepared to serve as a microwave-absorbing contrast agent for TAT. The PS hollow beads with openings on their surfaces were dispersed in saline solutions of 5.9%, 11.1%, and 23.1% (w/w) in concentration, respectively, followed by thermal annealing at 95 ºC under magnetic stirring. After 45 min, the particles were collected by centrifugation and washed with deionized water to remove excess saline solution outside the hollow beads. The TEM could only be used to characterize samples after the water inside the hollow beads had completely evaporated. As shown in Figure 5.3, each hollow bead contained a cube-shaped NaCl microcrystal in its core. The samples were thoroughly washed with water prior to TEM characterization, ruling out the possibility that the NaCl microcrystals were formed on the outer surfaces of the PS hollow beads. Interestingly, the size of the microcrystals increased as the concentration of the saline solution increased from 5.9% to 23.1%, implying that the single NaCl cube nucleated and grew from the limited supply of saline solution encapsulated in each PS hollow bead. Due to the relatively slow evaporation of water through the PS shell, and the hydrophobic nature of PS, only one nucleus was formed inside each hollow bead.

The feasibility of producing ICC-encapsulated PS hollow beads for use with microCT was also demonstrated. Again, the PS hollow beads with a hole on the surface were used

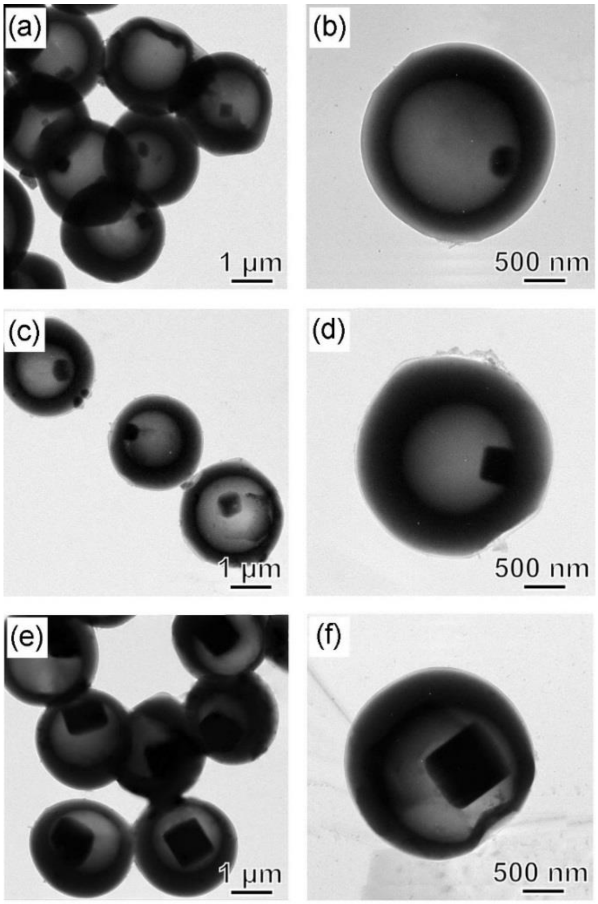

Figure 5.3. TEM images of the PS hollow beads that had been encapsulated with saline solutions of different concentrations: (a, b) 5.9 wt%; (c, d) 11.1 wt%; and (e, f) 23.1 wt%. The hole was closed by annealing the samples in the corresponding saline solutions at 95 ºC for 45 min. The samples were collected by centrifugation and thoroughly washed with water. The samples supported on copper grids were further dried at 75 ºC for 5 min to remove water prior to TEM characterization.[1] Printed with permission of John Wiley & Sons. Copyright 2012.

to encapsulate aqueous ioversol solutions with concentrations of 25%, 51%, and 74% (w/v), respectively. The products were collected by centrifugation and either suspended in water for microCT imaging or dried for characterization by TEM. Since the ICC contains a large number of iodine atoms, it had a darker contrast relative to PS under TEM. As shown in Figure 5.4, the ICC precipitated out as a solid mass inside the core of each PS hollow bead after the water had evaporated. The volume of the solid mass also increased with the concentration of ICC solution used for encapsulation. When the concentration of ICC was 74%, the mass of ICC occupied nearly the entire cavity inside the PS hollow bead, seen in Figure 5.4(e,f).

The most appealing advantage of this method for directly loading a functional material through the hole on the surface of a PS hollow bead is that it is very straightforward and not closely tied with the properties of the material to be encapsulated. Simply mixing the PS hollow beads with a solution/suspension containing the desired material allows the solution/suspension to quickly enter into the cavity of the PS hollow beads. The original state of the desired material does not really matter as long as it can be prepared as a solution or colloidal suspension. In the aforementioned studies, encapsulation was performed with two hydrophilic solids, NaCl and ICC, which can both be readily prepared as aqueous solutions.

Not only aqueous solutions but also organic liquids as hydrophobic as PFO can also be easily encapsulated in the PS hollow beads. In this case, the PS hollow beads with a hole on the surface were dried and dispersed in PFO to obtain a homogeneous suspension. The mixture was then sealed in a sample vial and placed in a 95 ºC oil bath for 30 min to close the hole on the surface of the PS hollow beads. Since PFO is a volatile compound,

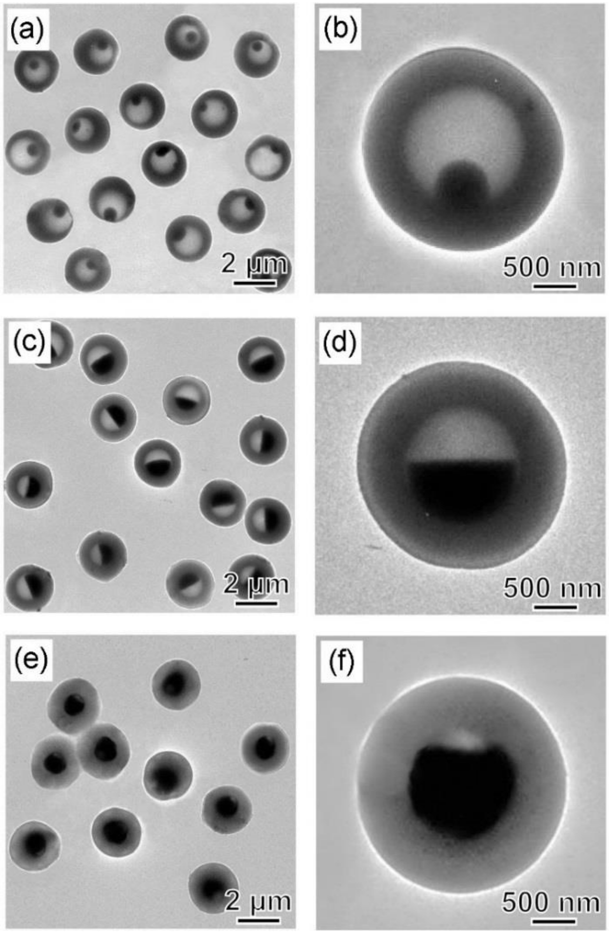

Figure 5.4. TEM images of PS hollow beads containing ioversol in the interiors. The hole was closed by heating the PS hollow beads at 95 ºC for 45 min in aqueous solutions containing (a, b) 25%; (c, d) 51%, and (e, f) 74% of ioversol, respectively. The samples were collected by centrifugation and thoroughly washed with ethanol and dried at 75 ºC for 5 min to remove the water inside the beads prior to TEM characterization.[1] Printed with permission of John Wiley & Sons. Copyright 2012.

the encapsulated PFO could not be observed by electron microscopy. However, the half-life of fluorine isotope ^{19}F is relatively long and has a nuclear spin of 1/2, making it easily detectable by MR spectroscopy and imaging. Specifically, ^{19}F MR spectroscopy and imaging can be performed using the same instrument used for proton MR imaging. Therefore, MR spectroscopy and imaging were used for qualitatively and quantitatively determining the encapsulation of PFO inside the cores of the PS hollow beads.

5.2.3 Imaging with the Encapsulated Contrast Agents

The saline-encapsulated PS hollow beads were evaluated as a contrast agent for TAT imaging. After annealing in the 23.1% saline solution, sealed particles were washed with water to remove excess saline solution. Samples were loaded into low-density polyethylene (LDPE) tubes at a concentration of 9.0×10^8 particles/mL. Two control samples were imaged for comparison. The first control was deionized water alone. The second control was PS hollow beads, whose hollow interiors were filled with deionized water to confirm that the water-encapsulated PS beads did not absorb microwaves to a greater degree than water alone. Figure 5.5(a-c) shows the cross-sectional TAT images of all three samples. Two values were used to assess the contrast-enhancing capability of the saline-encapsulated PS hollow beads: the peak and average signals. First, the peak value of the signal was determined from the reconstructed images, where the intensities are displayed in arbitrary units. The peak intensity for saline-encapsulated PS hollow beads was 2.6×10^{-5}, which is about 1.5 times greater than deionized water alone (with a peak value of 1.7×10^{-5}). Using both the maximum and average values gives a more accurate estimate of the difference between the controls and the saline-encapsulated PS hollow beads. The average values indicate that there was virtually no difference between deionized water alone and

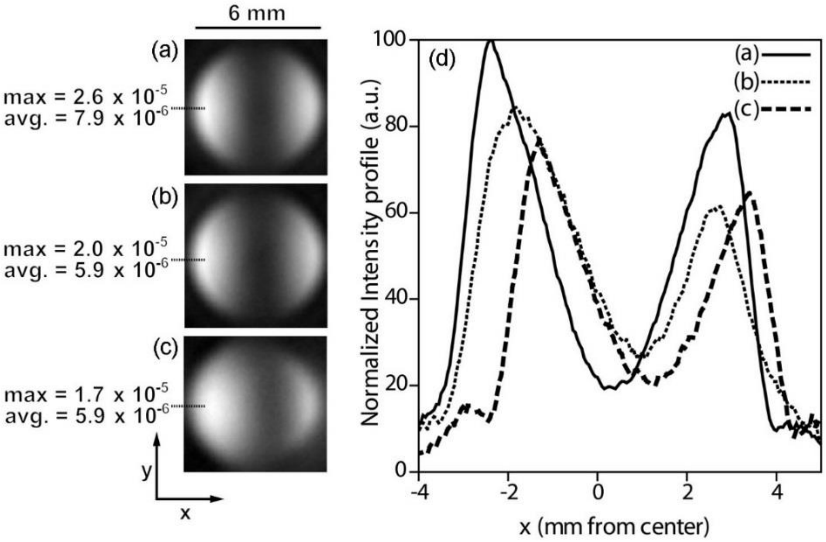

Figure 5.5. Thermoacoustic images of (a) saline-encapsulated PS hollow beads (prepared from the 23.1% saline solution), (b) DI-water-encapsulated hollow beads, and (c) DI water alone contained in a 6-mm (inner diameter) LDPE tube, where "max" indicates the peak signal value in an arbitrary unit of the reconstructed image and "avg." indicates the average signal value calculated over the entire square area shown. (d) Normalized signal intensity cross-section of images in (a-c), taken at the direction of the *x* axis. Signal intensities were normalized to the peak value in (a) for saline-encapsulated hollow beads.[1] Printed with permission of John Wiley & Sons. Copyright 2012.

the water-encapsulated hollow beads (5.9×10^{-6} for both samples). The average signal amplitude from the saline-encapsulated PS hollow beads was 7.9×10^{-6}, which was about 1.3 times as great as the controls.

The contrast enhancement ability of the ICC-encapsulated PS hollow beads was evaluated using microCT imaging. In this case, a poly(dimethyl siloxane) (PDMS) mold with a row of holes in the center was used to hold a series of aqueous suspensions of PS hollow beads encapsulating ICC solutions at different concentrations. Figure 5.6(b-d) shows the microCT images of a series of ICC-encapsulated PS hollow beads (all samples contained the same total number of PS hollow beads), in comparison to the blank PS hollow beads seen in Figure 5.6(a). The brightness of each image increased along with the

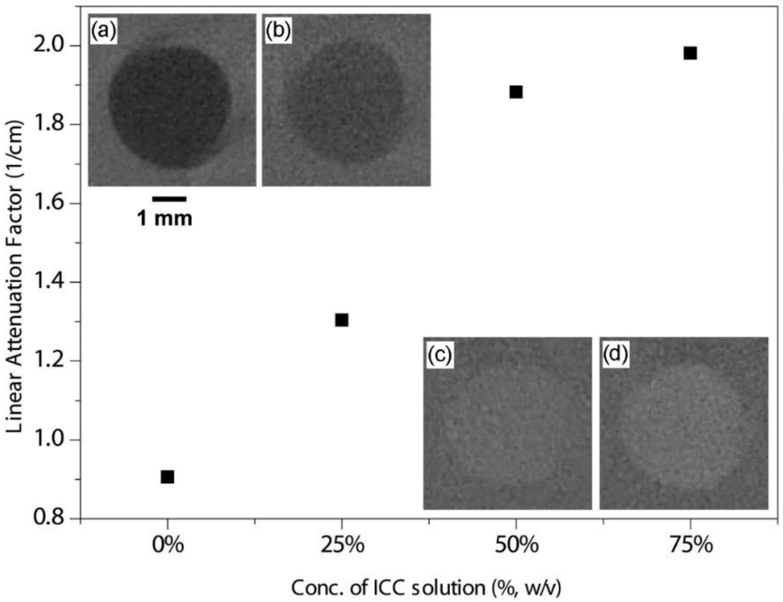

Figure 5.6. microCT imaging of PS hollow beads containing aqueous ICC solutions with different concentrations (used for encapsulation): (a) 0%, (b) 25%, (c) 51%, and (d) 74%, respectively. The square symbols shown in the figure indicate the average values of linear attenuation factors for each accompanying microCT image. The 1 mm scale bar is the same for all the microCT images.[1] Printed with permission of John Wiley & Sons. Copyright 2012.

concentration of ICC used for encapsulation. The brightness of a microCT image represents the ability of the medium to absorb the incident X-ray radiation, which is quantified by the linear attenuation factor. A large attenuation factor means that the X-rays are quickly attenuated as they pass through the medium, and a small attenuation factor means that the medium is relatively transparent to X-rays. Linear attenuation factor is usually measured using units of reciprocal length. Figure 5.6 also shows the average values of the linear attenuation factors as a function of ICC concentration used for encapsulation. As expected, the blank PS hollow beads did not significantly attenuate X-rays. The linear attenuation factor of ICC-encapsulated beads increased along with the concentration of ICC. In brief, the ability of ICC-encapsulated beads to attenuate X-ray radiation makes them useful as a

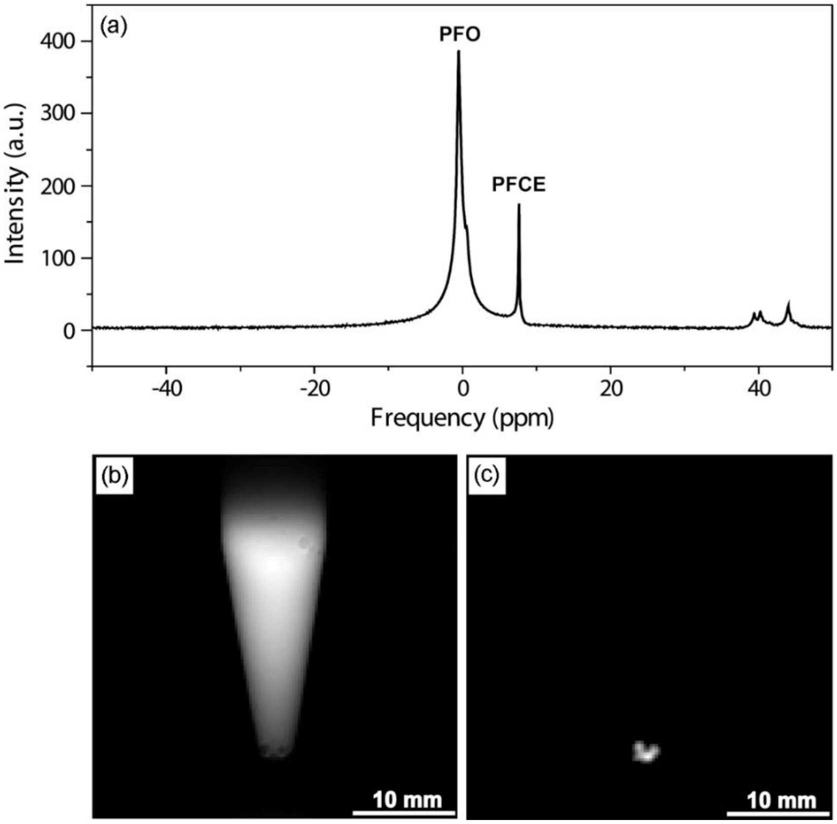

Figure 5.7. MR spectrum and images of PS hollow beads whose interiors had been encapsulated with PFO: (a) a ^{19}F MR spectrum acquired from a sample containing PFO-encapsulated PS hollow beads and PFCE, a reference compound; (b) ^{1}H mapping image from a suspension containing PFO-encapsulated PS hollow beads hosted in a centrifuge tube (left); and (c) ^{19}F mapping image of the same sample by using the peak of PFO.[1] Printed with permission of John Wiley & Sons. Copyright 2012.

contrast agent for CT imaging.

The PFO-encapsulated PS hollow beads were collected by centrifugation after the annealing process and re-dispersed in a centrifuge tube containing 1 mL water. 10 μL of perfluoro-crown ether (PFCE) was added into the suspension as an internal standard for the quantitative analysis. Figure 5.7(a) shows the ^{19}F MR spectrum acquired from this centrifuge tube containing a suspension of PFO-encapsulated PS hollow beads. As expected, two major ^{19}F peaks were detected, which were attributed to the fluorine atoms in PFO and PFCE, respectively. Since the instrument typically used for ^{1}H MR spectroscopy and imaging utilized a radiofrequency coil that was tunable to both ^{1}H and ^{19}F frequencies, so one could conveniently switch back and forth to acquire spectra and images in ^{1}H or ^{19}F mode from the same sample. Therefore, the sample used to collect the spectrum in Figure 5.7(a) was then used to acquire an image in ^{1}H mode (500 MHz) as shown in Figure 5.7(b). This ^{1}H mapping image was used to pinpoint the position of the tube and found that the suspension appeared bright, except a very small portion at the tip of the tube. After switching to ^{19}F mode (470 MHz), a complementary image was observed: Figure 5.7(c) shows that only the small portion at the tip of the tube was bright, but the remainder was dark. Since the density of PFO (1.766 g/mL) is greater than that of water, the PFO-encapsulated PS hollow beads tended to settle to the bottom of an aqueous suspension. This phenomenon explains the localization of ^{19}F signal shown in Figure 5.7(c). A quantitative measure of the amount of PFO contained in the sample shown in Figure 5.7(a) was obtained by integrating the peak area (see Experimental Details, Section 5.4.9 for detailed calculations). Three different batches of PFO-encapsulated PS hollow beads were prepared and submitted to quantitative analysis by MR. The first sample is shown in Figure 5.7a, which contained 33.8 μL PFO. The other two samples were also measured, and found to contain 33.8 and 34.2 μL PFO. The average total encapsulation of PFO measured in a typical batch of PS hollow beads was therefore 33.9 ± 0.2 μL, and each batch contained a total number of 7.0×10^{9} PS hollow beads. From the TEM image of an individual PS hollow bead, the theoretically total volume of interior cavities inside the batch of PS hollow beads was calculated to be about 33 μL. This value is consistent with the quantitative data obtained by MR measurement. In brief, by directly loading PFO through the hole on the surface of the PS hollow beads, PFO achieved high encapsulation efficiency.

5.3 Summary

In summary, a facile method for quick encapsulation of different types of contrast agents in PS hollow beads was demonstrated here. As a major deviation from the emulsion method most commonly used in literature for the preparation of hollow particles encapsulated with contrast agents or drugs, uniform PS beads with hollow interiors and the hole on the surface were used. Such hollow beads could be routinely produced in relatively large quantities by swelling commercial PS latex beads with toluene, followed by freeze-drying. The small hole on the surface allowed contrast agent to be directly and quickly loaded into the hollow beads as long as it could be supplied as a solution or a liquid. Annealing at a temperature (e.g., 95 ^{o}C) slightly higher than the glass transition temperature of PS allowed the hole to close and thus complete encapsulation and prevent leakage. Polymer degradation during heating was avoided by using temperatures significantly lower than the decomposition temperature of PS. Aggregation was prevented by using a relatively low concentration of PS beads for encapsulation (0.05 wt%, 0.2 wt%, and 0.4 wt% for encapsulation of saline, ICC, and PFO, respectively) and by using PS beads with negative charges on the surface.

It should be pointed out that the PS beads with micrometer-sized diameters were selected for the present work because of their availability in large quantities from commercial vendors. Other types of polymers such as poly(methyl methacrylate) (PMMA) or even those biocompatible and biodegradable such as polycaprolactone (PCL) and poly(L-lactide) have also been successfully prepared as hollow beads with openings on the surfaces and have been used for encapsulation.[28] In addition, polymeric microspheres and nanospheres with a range of sizes may potentially be used to match the needs of particular imaging applications.

In addition to the encapsulation of contrast agents as demonstrated in the present work, this approach can also be extended to other types of chemical or biological species including drugs and theranostic agents.[37,38] Major advantages of this new system for encapsulation include high encapsulation efficiency, good compatibility with different types of chemicals/materials, and uniformity of particle size distribution.

5.4 Experimental Details

5.4.1 Chemicals and Materials

PS latex beads of 1.89 μm in diameter were obtained from Polysciences (Warrington, PA) as an aqueous suspension (2.5% w/v or 5.68×10^9 particles per mL). Sodium chloride (99.5%), PFO (98%), and toluene (HPLC, 99.9%) were all purchased from Sigma-Aldrich (St. Louis, MO). Ioversol, an ICC, was obtained from Covidien (Mansfield, MA) as 51% and 74% (w/v) aqueous solutions with trade names of Optiray 240 and 350, respectively. The 25% ioversol solution was prepared by diluting the 51% solution with DI water.

5.4.2 Preparation of PS Hollow Beads with a Hole on the Surface

In a typical procedure, 1 mL of the as-obtained suspension of PS latex beads was centrifuged at 10,000 rpm for 3 min. After the supernatant had been removed, the beads were re-dispersed in DI water (0.5 mL) to obtain a new suspension with a concentration of 5% (w/v). 0.5 mL of this suspension was added into a mixture of DI water (4 mL) and toluene (0.6 mL), followed by magnetic stirring for 1 h to allow all the toluene to diffuse into the PS beads. The suspension was then added into a liquid nitrogen bath dropwise within 2 min. Finally, the frozen mixture was placed in a freeze-drier to let toluene evaporate for 24 h, generating PS hollow beads with a hole on the surface. The final product was collected as a dry, white powder.

5.4.3 Encapsulation of Saline and NaCl Microcrystals

0.125 g, 0.25 g, and 0.6 g NaCl solid was separately dissolved in 2 mL DI water to obtain saline solutions with concentrations of 5.9%, 11.1%, and 23.1%, respectively. Dried PS hollow beads (1.4 mg) were re-dispersed in ethanol (0.9 mL) and used as a stock solution. This stock solution (0.3 mL) was mixed with a saline solution (0.3 mL) and DI water (0.3 mL). The mixture was connected to a vacuum for 2 min, heated at 95 ºC with a silicone oil bath under magnetic stirring at 60 rpm for 45 min. Afterwards, the resultant saline-encapsulated PS hollow beads (sealed, with no hole on the surface anymore) were collected by centrifugation at 9,000 rpm for 15 min and washed 3 times with DI water (0.1 mL). The hollow beads were simply suspended in deionized water for TAT measurements. For TEM characterization, the product was re-dispersed in ethanol (0.1 mL) and 5 μL of the final suspension was dropped onto a carbon-coated copper grid. The grid was put in an oven heated at 75 ºC for 5 min to remove all water inside the PS hollow beads prior to TEM characterization. During the evaporation of water, the NaCl encapsulated in each hollow bead tended to precipitate out as a microcrystal.

5.4.5 Encapsulation of the Iodinated Contrast Compound

3.9 mg of the dried PS hollow beads were re-dispersed in ethanol (1.2 mL) and used as a stock solution. This stock solution (0.3 mL) was mixed with an ioversol solution (0.3 mL, 25%, 51%, or 74% w/v). The suspension was connected to a vacuum for 2 min, stirred at 60 rpm at room temperature for 1 h, and then heated with a silicone oil bath at 95 ºC under magnetic stirring at 60 rpm for 45 min. The resultant ICC-encapsulated PS hollow beads (sealed on the surface) were collected by centrifugation at 13,300 rpm for 3 min and washed 3 times with ethanol (0.1 mL). Finally, the product was re-dispersed in water (80 μL) for CT imaging. To prepare for TEM characterization, a sample was resuspended in ethanol (50 μL), and 5 μL of the final suspension was dropped onto a carbon-coated copper grid and dried at 75 ºC for 5 min to remove the water inside the beads.

5.4.6 Encapsulation of Perfluorooctane

PS hollow beads (3.8 mg) were re-dispersed in PFO (0.3 mL) in a centrifuge tube, and the suspension was connected to a vacuum for 2 min. Afterwards, PFO (0.2 mL) was added into the centrifuge tube to make up for the loss of PFO vaporized during vacuum. The suspension was then stirred at 60 rpm and heated at 95 ºC with a silicone oil bath for 30 min. The final product was separated by centrifugation at 10,000 rpm for 3 min. The collected precipitate was kept under ambient conditions to let the PFO outside the PS beads evaporate naturally. Finally, the product was re-dispersed in Di water (1 mL) for MR measurements.

5.4.7 Thermoacoustic Tomography

Suspensions of the saline-encapsulated PS beads (9×10^8 particles per mL, prepared from the 23.1% saline solution) were placed in LDPE tubes with a 6 mm inner diameter. The tubes were submerged in a mineral oil bath. Mineral oil was used as a background because it is a poor microwave absorber while being a good medium for transmitting ultrasound. A 3 GHz high-power microwave source with a 0.6-µs pulse width and a 10-Hz pulse repetition rate was applied to the bath via a standard horn antenna. The pulse power was measured to be 62 kW (37.2 mJ pulse energy). The acoustic signals generated were collected by an ultrasound transducer with a center frequency of 2.25 MHz and an active area diameter of 0.5 inch. The data were collected in a full circle around the sample, generating a cross-sectional image of the tube. Image reconstruction was performed using a delay-and-sum (backprojection) algorithm.

5.4.8 Micro-Computed Tomography

microCT (Scanco Medical microCT40) was used to image and characterize the ICC-encapsulated PS beads, with plain PS hollow beads serving as a control. A PDMS mold with wells of 4 mm in diameter was used to hold suspensions of the PS hollow beads (80 μL/well). The sample was scanned at a resolution of 16 μm (45 kVp, 176 μA, and 250 ms) perpendicular to the longitudinal axis of the wells. By using the manufacturer's software (Eval v5.0), linear attenuation factors were acquired within the selected circular area (3 mm in diameter) from 5 layers of each well at the same *z* positions. Average values were presented as the final data.

5.4.9 Magnetic Resonance

MR spectroscopy and imaging studies were conducted with a Varian UNITY-INOVA spectrometer (11.74 Tesla, Varian Associates, Palo Alto, CA). The PFO-encapsulated PS beads were centrifuged down to the bottom of a 1.5 mL centrifuge tube. A 2 mm tube containing 10 μL perfluoro-15-crown-5-ether (PFCE) was used as an internal standard during MR spectroscopy to enable quantification of the encapsulated PFO. MR spectra and images were acquired using a custom-built 1-cm-diameter single-turn solenoid RF coil dual-tunable to proton and fluorine frequencies (500 MHz and 470 MHz, respectively). Water (^{1}H) and PFO (^{19}F) MR images were acquired with the following parameters: spin-echo sequence; TR (1s), TE (15 ms), FOV (3×3 cm^2), matrix size (128×128), in plane

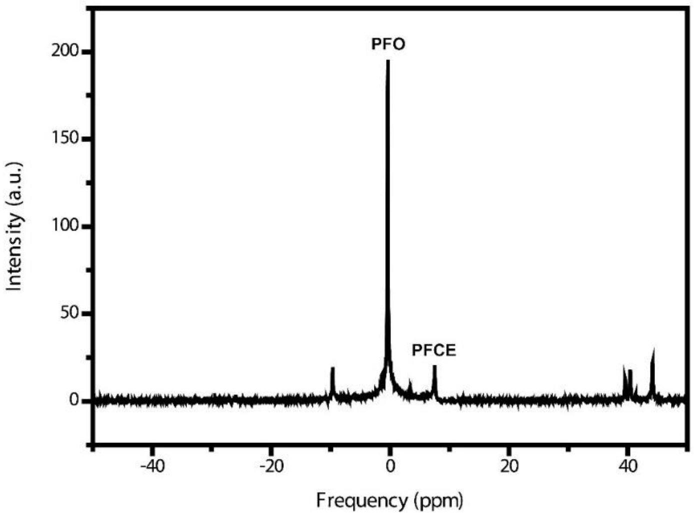

Figure 5.8. A control experiment for the quantitative analysis of PFO encapsulation was prepared by mixing 5.0 µL PFO and 2.0 µL PFCE. The peak area ratio of PFO to PFCE in this spectrum was used to determine the encapsulation efficiency of PFO.[1] Printed with permission of John Wiley & Sons. Copyright 2012.

resolution (234 × 234 µm^2), thickness (10 mm), and imaging time (2 and 8.5 min, respectively).

The encapsulation efficiency was determined by first performing a control experiment in which known amounts of PFO and PFCE were measured with the MR spectrometer. 5.0 µL PFO and 2.0 µL PFCE were mixed together in a tube, and the MR spectrum is shown in Figure 5.8. The area under each peak, A_{PFO} and A_{PFCE}, were measured, and the ratio was calculated:

$$\frac{A_{PFO}}{A_{PFCE}}=5.72. \qquad (5.1)$$

The known ratio of volumes added, V_{PFO} and V_{PFCE}, were related to the peak area ratio by a constant *k* in the following formula:

$$\frac{V_{PFO}}{V_{PFCE}}=\frac{5.0}{2.0}=\frac{A_{PFO}}{A_{PFCE}}\times k. \qquad (5.2)$$

After substituting the peak area ratio, *k* was found to be 0.44. This value was used to determine the total encapsulation volume of PFO in test samples using the 10 µL volume of PFCE added as a standard in each sample:

$$\frac{x}{10} = \frac{A_{PFO}}{A_{PFCE}} \times k \tag{5.3}$$

where x is the total volume of PFO encapsulated. Three samples were measured, and x was found to be 33.8 µL, 34.2 µL, and 33.8 µL, so the average encapsulation volume x in a batch of PS hollow beads was 33.9 ± 0.2 µL.

The theoretical maximum loading capacity was calculated based on the inner volume of a single bead taken from TEM images of the PS hollow beads, such as the one shown in Figure 5.9, which shows the interior diameter of the beads to be 2.083 µm. The inner volume was calculated to be 4.7×10^{-18} m^3 per particle, so a batch of particles used for a single encapsulation experiment containing 7.0×10^7 particles had a total inner volume of about 33 µL. This corresponds well to the measured encapsulation volume of PFO, indicating extremely high encapsulation efficiency.

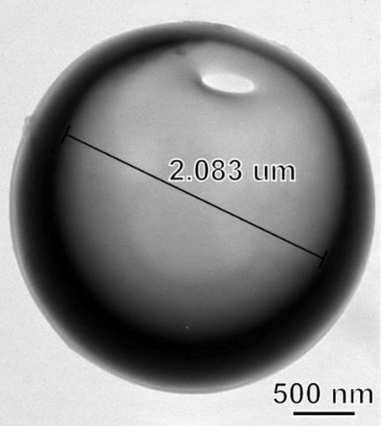

Figure 5.9. A TEM image of a typical PS hollow bead. The inner diameter was measured as shown to determine the theoretical total inner volume of a batch of PS hollow beads.[1] Printed with permission of John Wiley & Sons. Copyright 2012.

5.5 References

[1] M.-Y. Bai, C. H. Moran, L. Zhang, C. Liu, Y. Zhang, L. V. Wang, and Y. Xia. *Adv. Funct. Mater.* 2012, **22**, 764.

[2] K. An and T. Hyeon. *Nano Today* 2009, **4**, 359.

[3] M. O. Oyewumi and R. J. Mumper. *Drug Dev. Ind. Pharm.* 2002, **28**, 317.

[4] K. Zhang, D. Zheng, L. Hao, J. I. Cutler, E. Auyeung, and C. A. Mirkin. *Angew. Chem. Int. Ed.* 2012, **51**, 1169.

[5] M. Anthea, J. Hopkins, C. W. McLaughlin, S. Johnson, M. Q. Warner, D. LaHart, J. D. Wright, *Human Biology and Health*, Prentice Hall, Englewood Cliffs, New Jersey, **1993**.

[6] S. D. Perrault, C. Walkey, T. Jennings, H. C. Fischer, and W. C. W. Chan. *Nano Lett.* 2009, **9**, 1909.

[7] K.-I. Ogawara, M. Yoshida, K. Higaki, T. Kimura, K. Shiraishi, M. Nishikawa, Y. Takakura, and M. Hashida. *J. Controlled Release*. 1999, **59**, 15.

[8] G. Schmitz. *Basic Res. Cardiol.* 2008, **103**, 174.

[9] B. B. Goldberg, J.-B. Liu, and F. Forsberg. *Ultrasound in Med. & Biol.* 1994, **20**, 319.

[10] D. L. Wilcox, M. Berg, T. Bernat, D. Kellerman, and J. K. Cochran. *Mater. Res. Soc. Symp. Proc.* 1994, **372**, 1.

[11] R. Langer. *Nature* 1998, **392**, 5.

[12] D. E. Bergbreiter. *Angew. Chem. Int. Ed.* 1999, **38**, 2870.

[13] S. R. White, N. R. Sottos, P. H. Geubelle, J. S. Moore, M. R. Kessler,S. R. Sriram, E. N. Brown, and S. Viswanathan. *Nature* 2001, **409**, 794.

[14] F. Caruso. *Adv. Mater.* 2001, **13**, 11.

[15] G. Crotts, and T. G. Park. *J. Controlled Release* 1995, **35**, 91.

[16] T. Pitaksuteepong, N. M. Davies, I. G. Tucker, and R. Rades. *Eur. J. Pharm. Biopharm.* 2002, **53**, 335.

[17] V. Coccoli, A. Luciani, S. Orsi, V. Guarino, F. Causa, and P. A. Netti. *J. Mater. Sci: Mater. Med.* 2008, **19**, 1703.

[18] T. Betancourt, K. Shah, and L. Brannon-Peppas. *J. Mater. Sci: Mater. Med.* 2009, **20**, 387.

[19] M. C. Woodle. *Adv. Drug Delivery Rev.* 1998, **32**, 139.

[20] A. MaHam, Z. Tang, H. Wu, J. Wang, and Y. Lin. *Small* 2009, **5**, 1706.

[21] T. Freytag, A. Dashevsky, L. Tillman, G. E. Hardee, and R. Bodmeier. *J. Controlled Release* 2000, **69**, 197.

[22] M. F. Zambaux, F. Bonneaux, R. Gref, E. Dellacherie, and C. Vigneron. *J. Controlled Release* 1999, **60**, 179.

[23] S. Freitas, H. P. Merkle, and B. Gander. *J. Controlled Release* 2005, **102**, 313.

[24] W. Cui, J. Bei, S. Wang, G. Zhi, Y. Zhao, X. Zhou, H. Zhang, and Y. Xu. *J. Biomed. Mater. Res. B: Appl. Biomater.* 2005, **73B**, 171.

[25] S. Li, L. Nguyen, H. Xiong, M. Wang, T. C.-C. Hu, J.-X. She, S. M. Serkiz, G. G. Wicks, and W. S. Dynan. *Nanomedicine: NBM.* 2010, **6**, 127.

[26] X. Yang, L. Chen, B. Huang, F. Bai, and X. Yang. *Polymer* 2009, **50**, 3556.

[27] G. Liu, H. Ji, X. Yang, and Y. Wang. *Langmuir* 2008, **24**, 1019.

[28] U. Jeong, S. H. Im, P. H. C. Camargo, J. H. Kim, and Y. Xia. *Langmuir* 2007, **23**, 10968.

[29] S. H. Im, U. Jeong, and Y. Xia. *Nature Mater.* 2005, **4**, 671.

[30] A. Mashal, J. H. Booske, and S. C. Hagness. *Phys. Med. Biol.* 2009, **54**, 641.

[31] M. Pramanik, M. Swierczewska, D. Green, B. Sitharaman, and L. V. Wang. *J. Biomed. Opt.* 2009, **14**, 034018.

[32] M. Tanaka and M. Sato. *J. Chem. Phys.* 2007, **126**, 034509.

[33] J. J. Pasternak and E. E. Williamson. *Mayo Clin. Proc.* 2012, **87**, 390.

[34] S. Ahn, A. Y. Jung, J. P. Lee, and S. J. Lee. *Contrast Media Mol. Imaging* 2011, **6**, 437.

[35] M. Y. Bai and Y. Xia. *Macromol. Rapid Commun.* 2010, **31**, 1863.

[36] T. Arii. *J. Mass Spectrom. Soc. Jpn.* 2003, **51**, 235.

[37] L. E. V. Vlerken and M. M. Amiji. *Expert Opin. Drug Deliv.* 2006, **3**, 205.

[38] E. Pisani, et al. *Adv. Funct. Mater.* 2008, **18**, 2963.

CHAPTER 6: CONCLUSIONS AND FUTURE DIRECTIONS

This dissertation focused on the intersection of nanotechnology and medical imaging. I used SERS as an analytical tool to uncover changes in surface chemistry of Ag nanocubes, and designed a more streamlined approach to correlate SERS to the physical properties of Ag nanocubes. A thorough examination of the imaging capabilities of SERS was performed, identifying several key imaging parameters such as resolution and penetration depth. Multiplexing is a main benefit offered by SERS imaging, so I led a collaboration to develop and test a robust alternating minimization algorithm for the analysis of multiplexed SERS images with high accuracy.

I also investigated polymer hollow particles with a single hole on the surface for the encapsulation of different types of contrast agents. Image enhancement for TAT, MRI, and X-ray CT was tested after the successful encapsulation of their respective contrast agents. The compound used for TAT, a saline solution, is not typically used as a contrast agent, which made it the ideal candidate for demonstrating the effectiveness of encapsulation for novel imaging applications.

6.1 Future Directions for SERS and Imaging

6.1.1 Applications Tailored to SERS Imaging

Due to the limited penetration depth of SERS, its ideal imaging applications will likely not involve deep tissue. However, there are several cases in which I expect SERS to stand out as an invaluable tool.

Endoscopy is the standard technique used to image the GI tract, such as the oral cavity or the esophagus.[1-3] Molecular imaging based upon endoscopy is a real possibility, and currently under investigation with antibody-tagged fluorophores or nanoparticles.[1,4]

This could be an ideal application for SERS. There is no tissue scattering since an endoscope creates images of the surface of the mucosal membranes. SERS probes can be easily labeled with specific targeting ligands, and multiplexing could be employed to identify multiple lesions within a single patient. A PubMed search for "SERS endoscopy" returns only 5 results. The Gambhir group has made the greatest strides, and there is clearly much potential in this area.[4,5]

Image-guided surgery is another area where SERS could be very useful. Currently, there are many applications and devices being developed for guiding surgery with fluorescent markers.[6,7] Targeted fluorophores are used to identify tumor margins to ensure the complete resection during surgery to improve outcomes. There is also great potential for targeted SERS imaging in this field, although there is very little in the literature examining this possibility.[7-9]

6.1.2 Multiplexing and Barcode Tagging

As discussed in Chapter 4, multiplexing is one of the major advantages of using SERS as an imaging modality. Beyond just imaging applications, multiplexing could be applied to other medical applications such as assays, pathology slides, and diagnostics.[10-13] Advanced algorithms for separating mixed signals, such as the one described in this dissertation, will enable multiplexing to provide real value in clinical applications.

Multiplexing may also be used to create barcodes for high-throughput assays by combining different Raman probes in specific ratios. The concept of multiplexed barcodes has been explored to a greater extent using fluorescent markers.[14,15] As in imaging, however, SERS has many advantages over fluorescence when it comes to multiplexing, and there have been some examples in the literature of SERS barcodes.[16-18] These studies demonstrate the feasibility and potential of developing SERS barcodes for high-throughput assays for protein or DNA detection.

6.2 Future Directions for Polymer Hollow Beads

6.2.1 Encapsulating Materials for Multimodal Applications

The hollow beads with a hole on the surface can potentially be used to encapsulate a variety of materials for multimodal imaging. Since encapsulation is non-specific and loading relies only upon diffusion or applying a pressure, a solution containing a mixture of contrast agents would be encapsulated uniformly from bead to bead. For example, a mixture of gold nanoparticles tagged with SERS probes and PFO could theoretically be encapsulated for use in SERS, X-ray CT, and MR imaging, with each bead containing same relative concentrations of SERS probes and PFO.

Dyes or SERS probes can be encapsulated in specific ratios for “barcode” tagging, from which large scale, multiplexed assays may be built. In addition, since penetration depth is the greatest roadblock to SERS imaging, taking steps to maximize signal intensity will go a long way. Choosing SERS probes in resonance with the incident light source, such as NIR dyes, is one way. In addition, controlling the aggregation state of nanoparticles will greatly improve signal intensities. Encapsulation of nanoparticle SERS probes could facilitate aggregation and increase SERS EFs.

6.2.2 Extension to Biodegradable Materials

This dissertation describes encapsulation of contrast agents in polystyrene, a nontoxic although not biodegradable polymer. For some biomedical applications, it may be desirable for the hollow beads to be fabricated using biodegradable polymers, such as poly(lactic-co-glycolic) acid (PLGA) or polycaprolactone (PCL). Biodegradable hollow beads are an ideal vector for the encapsulation of a combination of imaging contrast agents and therapeutics for theranostic applications and monitored drug delivery. Traditional approaches for fabricating multimodal particles are complex and not always uniform in size or distribution of functional material. However, the facile loading process through the hole on the surface and the uniform shape should vastly improve the drug loading and release kinetics over other particle-based systems. Loading imaging contrast agents along with the drugs is a simple but effective approach for designing multimodal particles for diagnosis, treatment, and monitoring.

6.3 References

[1] E. L. Bird-Lieberman, A. A. Neves, P. Lao-Sirieix, M. O'Donovan, M. Novelli, L. B. Lovat, W. S. Eng, L. K. Mahal, K. M. Brindle, and R. C. Fitzgerald. *Nat. Med.* 2012, **18**, 315.

[2] A. Stallmach, C. Schmidt, A. Watson, and R. Kiesslich. *J. Biophotonics* 2011, **4**, 482.

[3] S. K. Amateau and M. I. Canto. *Curr. Opin. Gastroenterol.* 2010, **26**, 445.

[4] C. L. Zavaleta, K. B. Hartman, Z. Miao, M. L. James, P. Kempen, A. S. Thakor, C. H. Nielsen, R. Sinclair, Z. Cheng, and S. S. Gambhir. *Small* 2011, **7**, 2232.

[5] C. L. Zavaleta, E. Garai, J. T. C. Liu, S. Sensarn, M. J. Mandella, D. Van de Sompel, S. Friedland, J. Van Dam, C. H. Congat, and S. S. Gambhir. *Proc. Natl. Acad. Sci.* 2013, **110**, E2288.

[6] A. L. Vahrmeijer, M. Hutteman, J. R. van der Vorst, C. J. H. van de Velde, and J. V. Frangioni. *Nat. Rev. Clin. Oncol.* 2013, doi:10.1038/nrclinonc.2013.123.

[7] S. Keereweer, P. B. A. A. Van Driel, T. J. A. Snoeks, J. D. F. Kerrebijn, R. J. Baatenburg de Jong, A. L. Vahrmeijer, H. J. C. M. Sterenborg, and C. W. G. M. Löwik. *Clin. Cancer Res.* 2013, **19**, 3745.

[8] M. F. Kircher, et al. *Nat. Med.* 2012, **18**, 829.

[9] A. M. Mohs, M. C. Mancini, S. Singhal, J. M. Provenzale, B. Leyland-Jones, M. D. Wang, and S. Nie. *Anal. Chem.* 2010, **82**, 9058.

[10] L. Sun et al. *Nano Lett.* 2007, **7**, 351.

[11] D. S. Grubisha, R. J. Lipert, H.-Y. Park, J. Driskell, and M. D. Porter. *Anal. Chem.* 2003, **75**, 5936.

[12] B.-H. Jun, et al. *J. Comb. Chem.* 2007, **9**, 237.

[13] T. Vo-Dinh, L. R. Allain, and D. L. Stokes. *J. Raman Spectrosc.* 2002, **33**, 511.

[14] I. Krylova, R. R. Kumar, E. M. Kofoed, and F. Schaufele. *PloS One.* 2013, **8**, e63286.

[15] M. Han, X. Gao, J. Z. Su, and S. Nie. *Nat. Biotech.* 2001, **19**, 631.

[16] L. Qin, M. J. Banholzer, J. E. Millstone, and C. A. Mirkin. *Nano Lett.* 2007, **7**, 3849.

[17] J.-M. Li, C. Wei, W.-F. Ma, Q. An, J. Guo, J. Hu, and C.-C. Wang. *J. Mater. Chem.* 2012, **22**, 12100.

[18] S. Ye, J. Xiao, Y. Guo, and S. Zhang. *Chem. Eur. J.* 2013, **19**, 8111.